US Army Corps of Engineers®
Engineer Research and Development Center

PAVEMENT SUBGRADE PERFORMANCE STUDY

Final Report

Edel R. Cortez

January 2007

Pavement Subgrade Performance Study
Final Report

Edel R. Cortez
Cold Regions Research and Engineering Laboratory
72 Lyme Road
Hanover, New Hampshire 03755

ABSTRACT

All pavement materials contain moisture in various forms and amounts. The effects of moisture on the mechanical behavior of these materials vary from insignificant for some bound materials to very significant for some fine grained soils. Moisture effects become critical particularly during the spring thaw, but also where prolonged exposure to water sources occurs. The pavement design engineer must consider the effect of moisture on the mechanical properties of the constituent materials, and how different pavement layers interact under wet conditions.

This experimental and analytical study focuses on the effect that moisture in the subgrade has on the mechanical response and performance of flexible pavement structures. The research work is based on experiments on a series of full-scale pavement test sections that were built inside a testing facility where the temperature and soil moisture were artificially kept constant at predetermined values. The test sections were subjected to accelerated traffic by means of a heavy vehicle simulator. The test results were analyzed and relationships between subgrade soil type, moisture content, load intensity and number of traffic repetitions to failure were established. The effects of subgrade soil moisture content on subsurface strain and stress distributions were explored and relationships between resilient deformation and the progression of permanent deformation were examined. The existing failure criteria based on limiting the resilient strain at the top of the subgrade were revised in view of the new experimental data. The data indicates that the criteria must be specific for each soil type, and the subgrade soil moisture condition must be established in order to predict permanent deformation. The virtual sensor experimental method is presented and used to build profile and contour cross sections of strain and stress. Comparing the stress and

strain figures in the vertical direction to those in the longitudinal and transversal directions it is apparent that the loading regime significantly differs from that used in laboratory triaxial tests. In laboratory triaxial tests the confining pressure is radial and symmetric around the side walls of the cylindrical specimen. In real pavements the loads are rolling over the pavement surface and stress rotations occur.

Based on the experimental data, subgrade rut depth prediction models were developed for each soil type as functions of subgrade moisture content, load intensity, and number of traffic repetitions.

TABLE OF CONTENTS

SUMMARY, CONCLUSIONS AND RECOMMENDATIONS 121

LIST OF FIGURES

LIST OF TABLES

PREFACE

CHAPTER I

INTRODUCTION

1.1 Historical Perspective

The history of pavement design parallels that of the development of cars, trucks, and airplanes. The roads and streets that existed prior to the invention of the internal combustion engine were relatively primitive and consistent with the low requirements imposed by pedestrian and horse-pulled vehicle traffic. The advent of heavier trucks demanded stronger and more durable roads. Engineers were charged with the task to devise pavement design and construction methods. As the investment in highways and airfields grew, specialized agencies were created to gather and develop the necessary expertise to design, build, and maintain the growing pavement networks. By necessity, the first pavement design methods were purely empirical. Efforts were made to develop material testing methods. When material properties were difficult to obtain, index parameters were devised. A soil classification systems specific for pavements was developed by the U. S. Department of Public Roads (Hogentogler and Terzaghi, 1929). Subgrade soils were classified from A-1 (coarse grained, stronger) to A-8 (fine grained, least desirable). With only minor improvements, this soil classification system is still in common use. It is known as the American Association of State Highway and Transportation Officials (AASHTO) soil classification system.

A more elaborate pavement design method emerged by adopting the California Bearing Ratio (CBR) index and the Marshall method of asphalt mixture design. The U.S. Army Corps of Engineers played a lead role in the development of these methods, and in their integration into a pavement design system that was adopted by most transportation agencies (Huang, 2004).

The economic boom of the post-World War II period resulted in accelerated need for a modern national highway system. The AASHO Road Test was conducted in Ottawa, Illinois, from October 1958 to January 1960. The cost of the experiments was $27,114.220 (at 3.5% inflation, the present value is $141 million; Highway Research Board, 1962b). From the findings of these experiments, an interim pavement design guide was produced in 1972 that evolved into the 1986 AASHTO Pavement Design Guide. This was 100% empirically based on the AASHO Road Test observations. The 1993 AASHTO Guide for Design of Pavement Structures remained empirical, with the exception of an optional linear elastic design methodology that has limited use. At the time of this writing (2006), this is still the official pavement design guide used in the United States and in many countries. A draft version for a proposed new mechanistic-empirical (M-E) pavement design guide has been completed, and it is currently in the process of official approvals. The new M-E guide requires the use of specially developed computer software that integrates finite element code and that is computationally intensive. The framework for this method is complete and designed in a modular format that facilitates the replacement of existing models when improved versions become available. The current subgrade model is generic for all unbound materials. The experiments included in the research support the development of new subgrade models

that consider soil type and moisture content. A separate series of data reports document

the construction, instrumentation, and testing of the test sections and the experimental

results are recorded in a database that will be publicly available for use by other

researchers.

A series of full-scale flexible pavement test sections was build inside a specialized

facility where traffic, temperature, and moisture were controlled. Traffic was applied by

means of a heavy vehicle simulator (HVS). The HVS is a sophisticated machine designed

to simulate highway truck traffic in an accelerated manner, whereby the traffic volume

normal of several years of highway service is compressed into several weeks. The test

sections were instrumented with stress, strain, deformation, moisture, and temperature

sensors. The sensor responses during traffic events were recorded by means of a

computerized, custom-made data acquisition system.

1.2 The Problem

The current highway pavement design methods are based on the findings of the

AASHO Road Test of the 1950's. These experiments were conducted during a period of

1 year and 3 months at one location (Ottawa, Illinois), and the effects of traffic and

seasonal variations were confounded. Extrapolating from these experiments onto modern

design lives of 20 to 50 years may not be justified. Aside from a linear elastic procedure,

the current AASHTO Guide for Design of Pavement structures (AASHTO, 1993)

contains only empirical procedures. The predominant subgrade soil at the location of the

AASHO Road Test was classified as AASHTO type A-6. Pavement performance with

other subgrade soil types, such as sand or clay, may vary significantly, especially if the subgrade moisture content also varies.

1.3 A Solution

A new initiative led by the American Association of State Highway and Transportation Officials (AASHTO), the National Academies, and the Federal Highway Administration (FHWA) through the National Cooperative Highway Research Program (NCHRP) is developing a more mechanistic pavement analysis and design methodology. The initial methodology integrates the best available material models with a plan to substitute them for better models as they become available. The current subgrade model is generic for all subgrade soil types.

A national pooled-fund study (SPR 2-208 *Pavement Subgrade Performance Study*), with participation of 19 states, the FHWA, and the U.S. Army Corps of Engineers, was designed to develop failure criteria and performance prediction models according to subgrade soil type and moisture condition.

Twelve sets of full-scale flexible pavement test sections were built inside the Frost Effects Research Facility (FERF) of the Cold Regions Research and Engineering Laboratory (CRREL). CRREL is a component of the U. S. Army Engineer Research and Development Center (ERDC), the R&D branch of the U.S. Army Corps of Engineers. The temperature was artificially kept constant at room temperature. The subgrade soil moisture was kept constant by means of a closed basin system. The experiments in this

study will constitute the basis for new subgrade models that consider soil type and

moisture variations.

1.4 Complexity of The Problem

During the early 1990's, the transportation community, led by AASHTO,

recognized the new opportunities brought by personal computers and advances in sensor

technologies and created a task force to plan the development of a mechanistic design

method for pavement structures. After a few years of planning, this task force determined

that a purely mechanistic method was not yet possible because of the great mechanical

complexity of a typical pavement structure. As shown in Figure 1, the properties of the

various constituent materials vary with time in their own unique way. For example, frost-

susceptible soils in seasonal frost areas may become very weak during the spring thaw,

while the asphalt concrete becomes more brittle with time and exposure to solar radiation,

and then decays through cracking. Asphalt concrete is also susceptible to softening at

high temperatures. Portland cement typically gains strength fast at early age and slowly at

older age. Bound or cohesive materials can be modeled as a continuum, while unbound,

coarse-grained soils may need to be treated as a system of particles that are able to rotate

and slip. The various pavement layers must work as components of a pavement structure.

On the other hand, traffic volume most commonly increases with time. The effect that

one truck pass has near the beginning of the pavement life is different from that of the

same truck at late pavement age.

Cumulative damage per load application
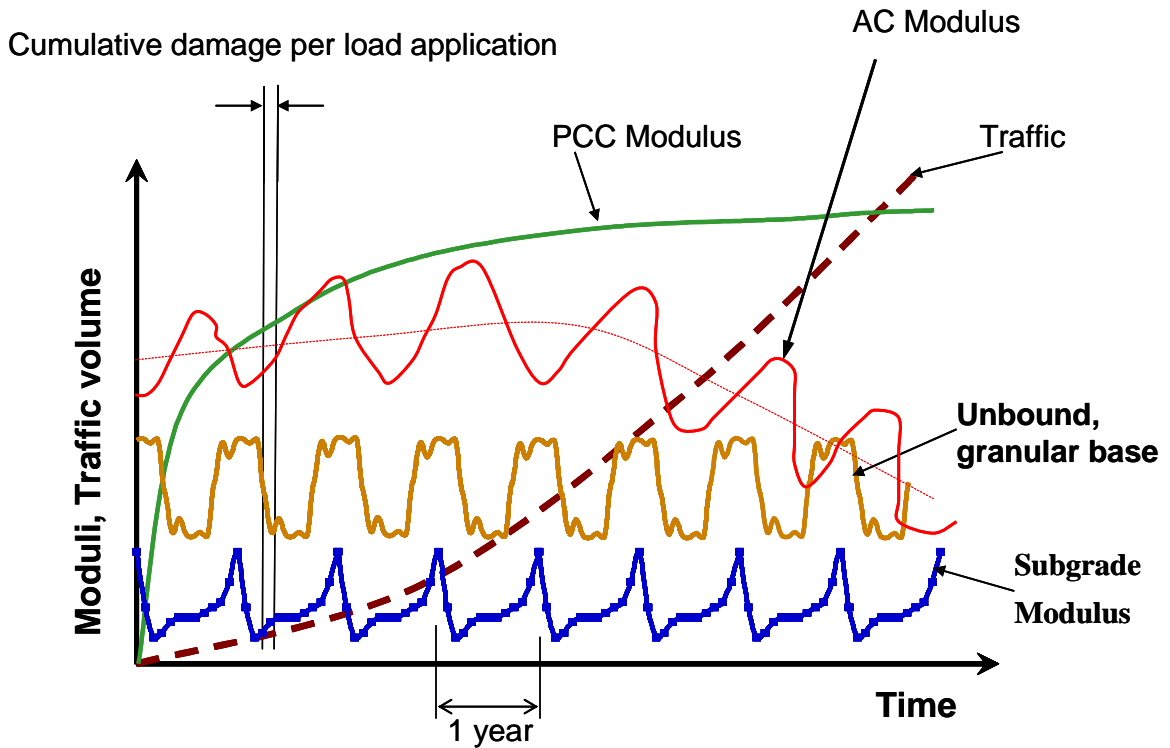
Figure 1. Variation of layer moduli and traffic volume.

1.5 Transition from Empirical to Mechanistic Analysis and Design

The first AASHTO pavement design guide of 1986 (AASHTO, 1986) was completely empirical. The 1993 AASHTO *Guide for Design of Pavement Structures* introduced linear elastic analysis. At the time of this writing (2007), this is still the official guide. The new, proposed AASHTO *Mechanistic-Empirical Pavement Design Guide* implements mechanistic analysis using mechanistic material inputs to estimate stresses and strains that, together with transfer functions (the empirical component), estimate and tally cumulative damage in the forms of common distress modes, such as rutting and cracking. The pavement designer must compare the amount of calculated distress with failure thresholds to judge the adequacy of a design.

1.6 Objectives of This Research

The experimental and analytic research included in this report was planned to define the response of pavement structures, built with various subgrade soil types at various moisture conditions, to repetitive traffic loads. The fundamental hypothesis was that different subgrade soil types have different moisture susceptibility and performance. From experiments on instrumented, full-scale pavement test sections, this research has produced load-response-performance relationships useful in evaluating existing failure criteria and in developing improved pavement models.

CHAPTER 2

EXPERIMENTAL PLAN

2.1 Subgrade Soil Types

Soils are formed by the disintegration of rock from the earth crust coupled with integration of organic particles and physical and chemical effects of weathering. Because geologic history, rock composition and topography vary across the continental United States, soils types also vary. Highway and airfield pavements must be built in locations with all soil types. Figure 2 shows a map divided in zones according to the prevalent soil type.

Residual soils
Filled valleys and outwash
Coastal plain soils
Alluvium
Glacial soils
Lacustrine soils
Loess
Clay and organic soils
No-soil areas
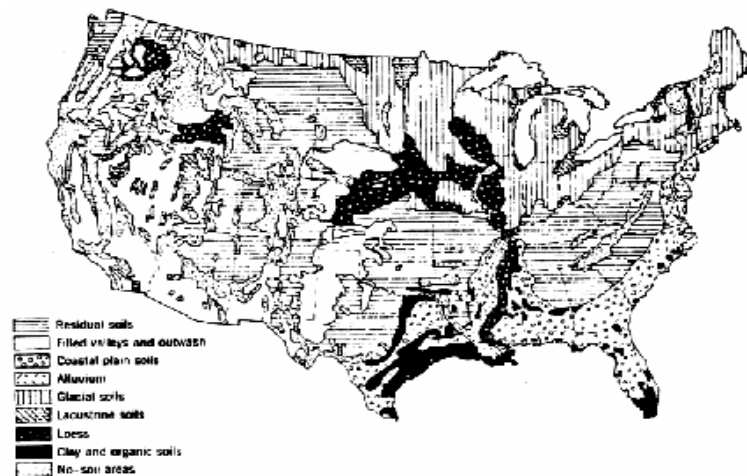
Figure 2.   Variety of soil typesin theUnited States. (After Belcher et al., 1946).

2.2 Experimental Matrix

Through consultation with the participant state Departments of Transportation (DoTs), four soil types were selected for this research project. Each of the soils was planned to be tested at three moisture conditions: one at optimum moisture content defined by a modified Proctor test (AASHTO, 2005), one at a moisture condition near the end of practical constructability, and one at an intermediate value between the other two extremes. The practical constructability limit had to be determined in advance on the basis of the available laboratory data, but some uncertainty was acknowledged.

Table 1 shows the test matrix. One test section for each combination of subgrade soil type and moisture content was built. The test sections were numbered from Test Section 701 (TS 701) through Test Section 712 (TS 712). Each test section had from 4 to 6 test windows.

Table 1 Experiment matrix based on soil types and moisture conditions.

Subgrade Moisture Content	AASHTO Soil Type			
	A-2-4	A-4	A-6	A-7-5
M1	Optimum 10 % TS 701	Optimum 17 % TS 702	Optimum 16 % TS 709	Optimum 20.5 % TS 712
M2	12 % TS 707	19 % TS 704	19 % TS 708	21 % TS 710
M3	15 % TS 703	23 % TS 705	22% TS 706	25 % TS 711

The original intent was to test four subgrade soil types. A deviation in the plan occurred when, after numerous soil classification tests, the soil in one of the test sections (Test Section 710) proved to be borderline type between A-6 and A-7-6. The Atterberg limit tests also indicated that the soil originally intended to be type A-7-6 had to be re-classified as A-7-5 because more tests supported this classification than those supporting its classification as A-7-6.

2.3 Laboratory Soil Tests

Laboratory soil tests were conducted on representative samples of the base course and subgrade soils. The following AASHTO standard soil tests were used: [probably all should be in refs]

- Particle Size Analysis of Soils (T 88-90).

- Determining the Liquid Limit of Soils (T 89-90).

- Determining the Plastic Limit and Plasticity Index of Soils (T 90-87).

- Specific Gravity of Soils (T 100-90).

- Laboratory Determination of Moisture Content of Soils (T 265-86).

- The Moisture-Density Relations of Soils (Standard Proctor) (T 99-99).

- The Moisture-Density Relations of Soils (Modified Proctor) (T 180-99).

- The California Bearing Ratio at Standard Proctor Density (T 193-81).

CHAPTER 3

FULL-SCALE PAVEMENT TEST SECTIONS

3.1 Materials

The materials and layer structure used for the test sections were kept constant for all test sections except for the subgrade soil type and moisture content.

The asphalt concrete material of the binder course conformed to the Vermont Type II standard, with 19-mm (.75 in.) maximum aggregate particle size and 4.5% of asphalt binder PG-58-34. The asphalt concrete material of the wearing course conformed to the Vermont Type III standard, with 13-mm (0.5 in.) maximum aggregate particle size and 5.3% of asphalt binder PG-58-34. The nominal thickness of the binder course was 51 mm. The nominal thickness of the wearing course was 25 mm (1 in.).

The base course material was made of unbound crushed stone. It was classified as an AASHTO type A-1 soil. According to the Unified Soil Classification System, the base course soil was type GP-GM (mix of poorly graded gravel and silty gravel). The base course material met the New Hampshire specification 304.4 (crushed stone, fine) except for the portion passing the sieve 0.074-mm (#200) that was 11% by weight versus the specified limit of 5%. The fines were classified as non-plastic. According to the modified Proctor test, the base course maximum density was 2232 kg/m^3 (139.3 lb/ft^3) at optimum moisture content of 6%. The crushed stone was obtained from an amphibolite bedrock

quarry in Lebanon, NH (Lane and Fish, 2003). The fine soil particles are made of rock

dust resulting from the crushing operation.

Figure 2. Base course crushed stone.

(The scale reference circle is a U.S. quarter coin, 24 mm in diameter.)
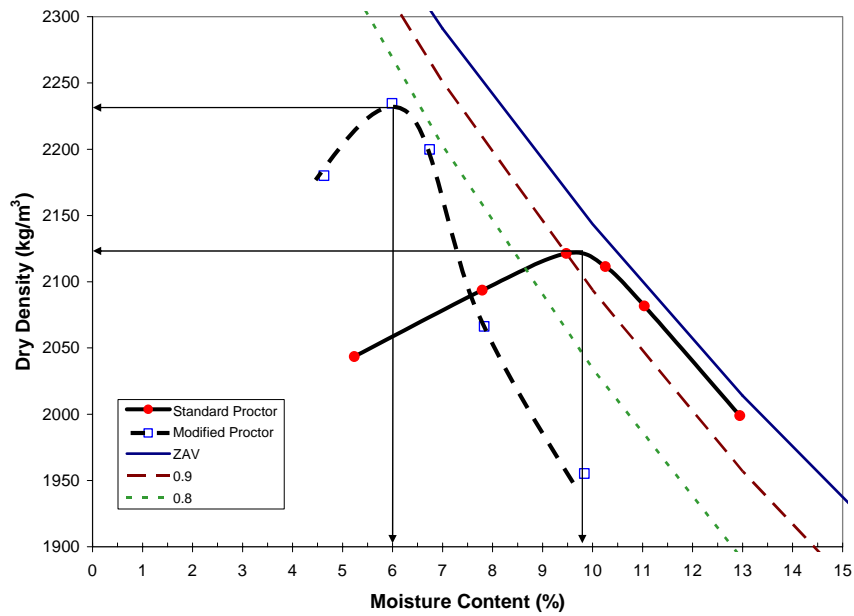
Figure 3. Base course standard and modified Proctor test results.
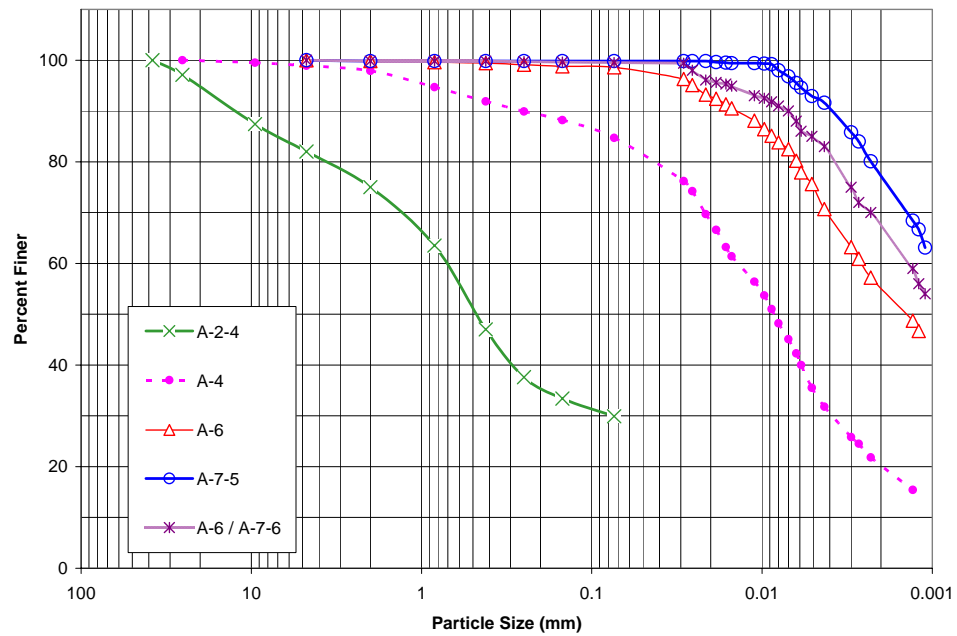
Figure 4. Subgrade soils particle size distributions.

Table 2. Subgrade soil properties.

Soil Classification		Passing sieve 200 (%)	Liquid Limit	Plastic Limit	Optimum Moisture (%)	Maximum Density (kg/m^3)	Specific Gravity
AASHTO	USCS						
A-2-4	SM	29.9	30	3	10	1934	2.72
A-4	ML	84.7	28	8	16	1780	2.72
A-6	CL	98.6	33	15	16	1791	2.70
A-6/A-7-6	CL/CH	99.5	40	21	17	1800	2.72
A-7-5	MH	99.8	55	21	20	1700	2.71

The subgrade soils were obtained from various regional sources. Figure 4 shows the particle size distributions of the subgrade soils included in this study. The data were obtained from sieve and hydrometer tests.

Table 2 summarizes the relevant material properties for the subgrade soils in this study. The amount of soil particles passing standard sieve number 200 is an index used in conjunction with the liquid and plastic limits (Atterberg limits) to classify the soils in the two soil classifications displayed. The Unified Soil Classification System (USCS) is widely used in science and engineering. The AASHTO soil classification system is used more within the transportation area, and it is the most applicable to this study. The maximum density and optimum moisture content values are needed for construction quality control, and the soil specific gravity value allows weight and volume relationships and conversion between volumetric and gravimetric moisture content measurements.

3.2 Structure

The pavement structure of the test sections consisted of a 76-mm (3-in.) thick asphalt layer over a 230-mm (9-in.) thick crushed stone base course directly resting on the subgrade soil. The subgrade soil thickness was 3.35 m (11 ft). A thick portland cement concrete slab placed at the bottom of the subgrade simulated bedrock. Figure 5 shows a cross section of the test sections.
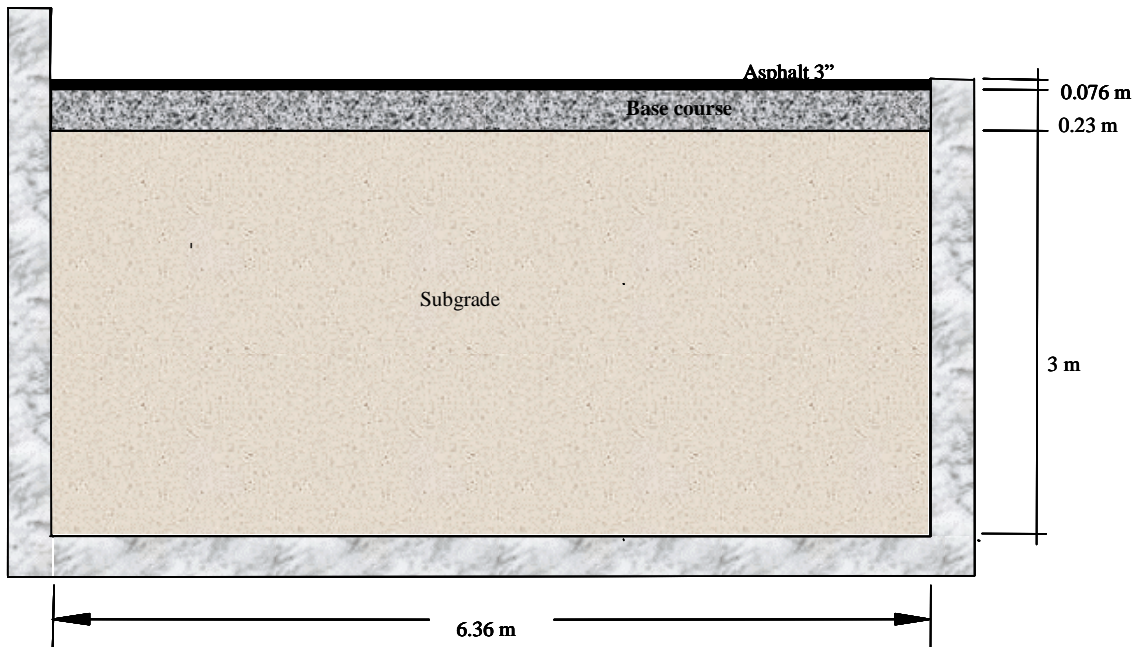
Figure 5. Transversal cross section.

Portland cement concrete walls delimit the test section on three sides. A concrete ramp was built on the remaining side. For practical purposes, the concrete floor, ramp, and walls, coupled with the top asphalt layer, constitute a sealed system for moisture. Figure 6 shows the empty test basins before construction of the subgrade began. The effectiveness of this system to hold the subgrade moisture was confirmed by the many soil moisture measurements during construction, traffic, and forensic evaluation at the end of the test period.

Figure 6. Empty test basins.

The thicknesses and properties of the asphalt layer and base course were constant parameters in these experiments. The variables were the subgrade soil type, moisture content and traffic load intensity.

3.3 Sensors

The test sections were instrumented with sensors that measured stress, strain, deformation, temperature, and soil moisture.

3.3.1 εmu Soil Strain Coils

The εmu coil system of measurement was invented at the University of Nottingham in the United Kingdom (Dawson, 1994), but the εmu coils used in this study were manufactured at CRREL in Hanover, New Hampshire. The system works with pairs of electromagnetic induction coils. One coil is externally energized. A second coil placed at a close distance experiences electromagnetic induction and produces a voltage that

varies with the distance between the coil pair. The induced voltage is calibrated against a

series of inter-coil distances to produce a correlation as shown in Figure 7. Coil pairs

were formed in the coaxial and coplanar modes. The coaxial mode was used to measure

vertical deformation, and the coplanar mode to measure longitudinal and transverse

directions relative to the direction of

traffic.

Coaxial Case
$y = 8.5996x^{-0.3984}$
$R^2 = 0.998$

Coplanar Case
$y = 7.1753x^{-0.2693}$
$R^2 = 0.999$

Inter-coil Distance (in)

Sensor output (Volts)
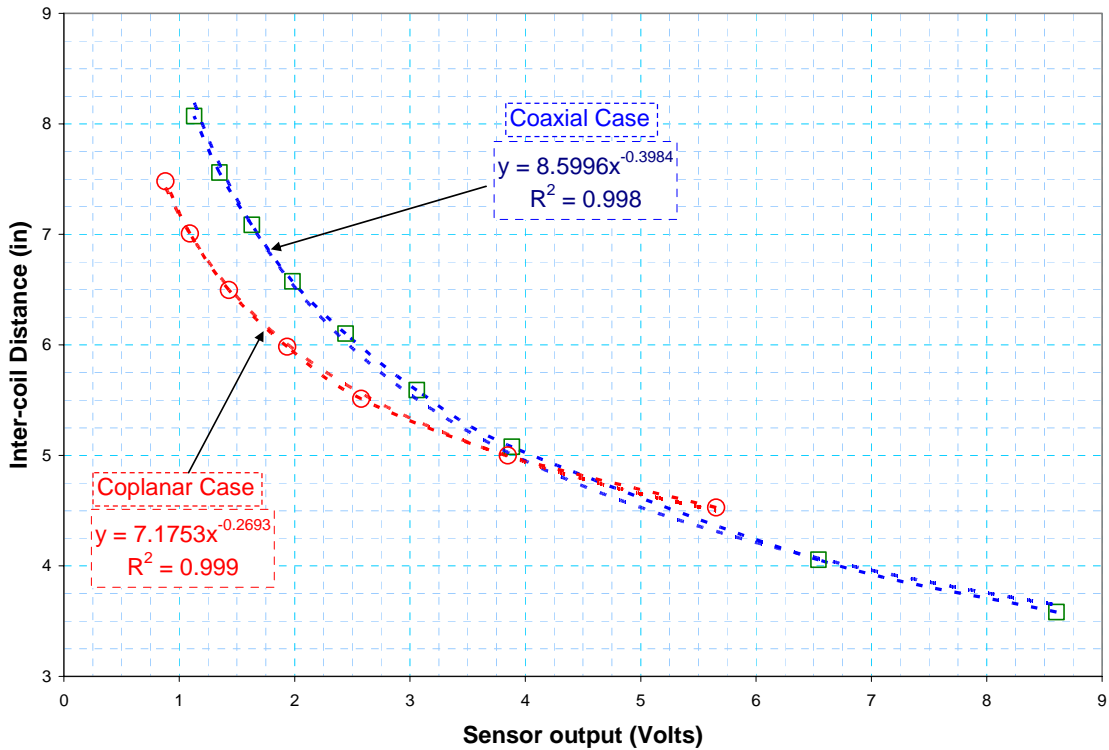
Figure 7. Voltage–distance correlation for   mu coils.

Figure 8. Ɛmu coils to measure longitudinal and transversal deformations.

Figure 8 shows three ɛmu coils arranged in coplanar mode to measure transversal and longitudinal deformations relative to the direction of traffic. The center coil, called "the sender," is the one externally energized with alternating current. This generates a magnetic flux field. The side coils, called "the receivers," placed within the magnetic flux field generate an electric current that is non-linearly related to the distance between the coils. The sender coil can also form pairs with receiver coils above and below, thereby measuring vertical deformation in coaxial mode. With this type of arrangement, deformation is measured in the vertical, longitudinal, and transversal directions. Stacks of ɛmu coils were embedded in the test sections in this study. The vertical deformations can be added to obtain the total vertical deformation. Measurements of deformations in individual layers allow the separate computation of deformations in the asphalt concrete, base course, and subgrade regions of the pavement structure. Comparing the initial inter-coil distances to those after and during traffic events allows the derivation of permanent

and resilient strains attributed to mid-points between coil pairs. A mobile εmu sensor was placed on top of the asphalt surface to measure the deformation and strain within the asphalt layer by forming a pair with a sensor placed immediately below the asphalt layer.

The εmu coil system suffers from the confounding of voltages resulting from the relative displacement between a pair of coils and that produced by the electromagnetic flux caused by the passing of any iron containing body, such as the steel in truck bodies. In our experimental setting, we were able to measure the signal generated by the moving wheel assembly with the tires suspended in the air at a height of only few millimeters. This signal was subtracted from the composite signal to obtain a signal that represented the distance or change of distance between coil pairs, and thereby corrected for the effect of the moving iron mass in the tire assembly.

3.3.2 Stress Sensors

During the experimental design phase of this study, an evaluation of commercially available soil stress cells was conducted at the University of Massachusetts (Zhang et al., 1995). The objective of this evaluation was to identify the best available stress cell type for use in our test sections. This study recommended the selection of stress cells manufactured in Denmark and distributed by Dynatest, Inc. These stress cells were found to produce better linearity and conformance, and lower hysteresis. However, it was found that these cells were prone to output drifts with time and with temperature changes. This would be a major problem with static stress measurements, but not for the short durations typical of dynamic traffic events. The diameter of these cells made them adequate for measurements in fine-grained soils. For coarser soils, such as those in the base course, Geokon® stress cells were selected because of their larger diameter. In later

test sections, a new generation of smaller Geokon stress cells was used to replace damaged Dynatest stress cells. The replacement was made after careful side-by-side assessments and because of lower cost and faster supply from the Geokon manufacturer who is in CRREL's local area. The diameter of the Dynatest stress cells is 68 mm (2.7 in.). The diameter of the Geokon stress cells used in the base course was 223 mm (9 in.), and the diameter of those used in the subgrade was 100 mm (4 in.). All the stress cells were calibrated by the manufacturer.
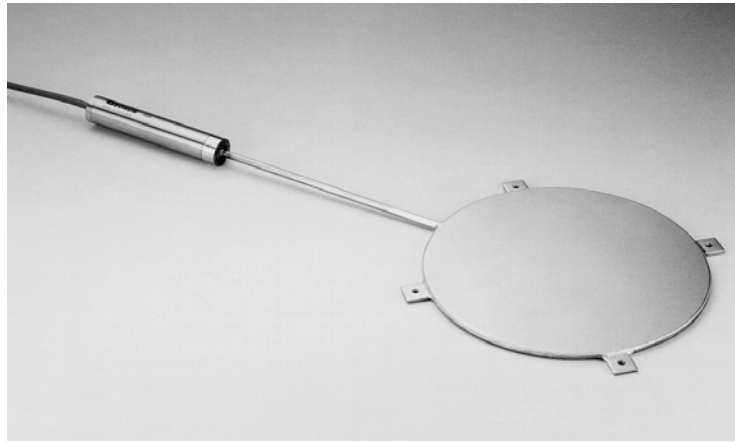
Figure 9. Geokon® stress cell.
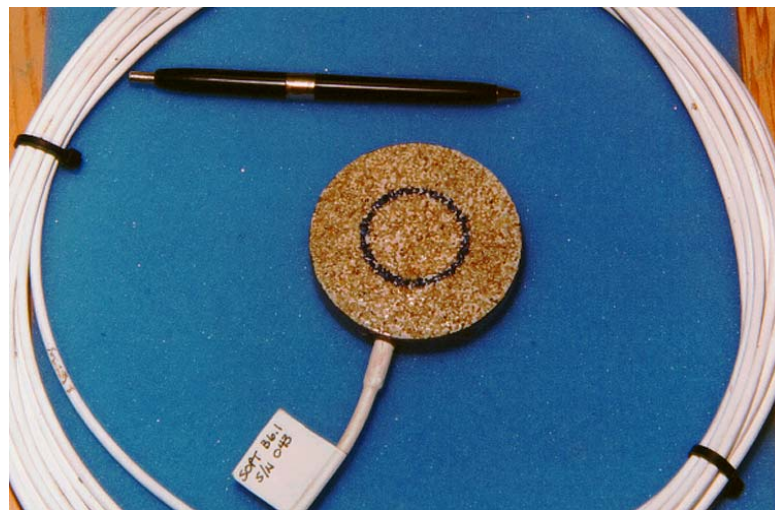
Figure 10. Dynatest® stress cell.

Figure 11. Triaxial set of Geokon® stress cells.

3.3.3 Moisture Sensors

Two types of moisture sensors were used in these experiments. In the early test sections, Vitel Hydra® sensors were embedded in the base course and the subgrade. These sensors measure moisture indirectly through high-frequency (50-MHz) complex dielectric constant measurements. The dielectric constants of water, soil particles, and air are approximately 80, 4, and 1, respectively. The dielectric constants of the soil–water–air composite increase as the moisture content increases. Therefore, volumetric moisture content can be indirectly measured through the use of appropriate calibration functions.
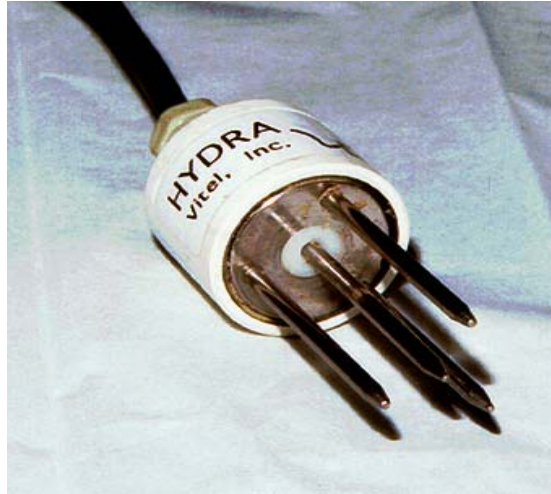
Figure 12. Vitel Hydra® moisture gauge.

During the length of this study, the manufacturer of the Vitel Hydra sensors experienced very significant business convolutions and technical support was less than desired. This led to the adoption of another type of moisture sensors for the latter test sections: the Campbell Scientific® reflectometer soil moisture probes model CS615 shown in Figure 13. These sensors measure the oscillation frequency between two rods embedded in the moist soil. The oscillation frequency is related to the dielectric constant that changes with moisture content, and, to a lesser degree, with temperature. The sensor readings are also affected by salinity, mineralogy, and the presence of organic materials. These sensors alone are not accurate enough for this study, but this deficiency was corrected by oven dry measurements during construction and during the forensic evaluation.

Moisture sensors were located at three depths at each of three horizontal locations. There were moisture sensors in the middle of the base course, and in the subgrade at 15 cm (6 in.) and 61 cm (2 ft) below the top of the subgrade.
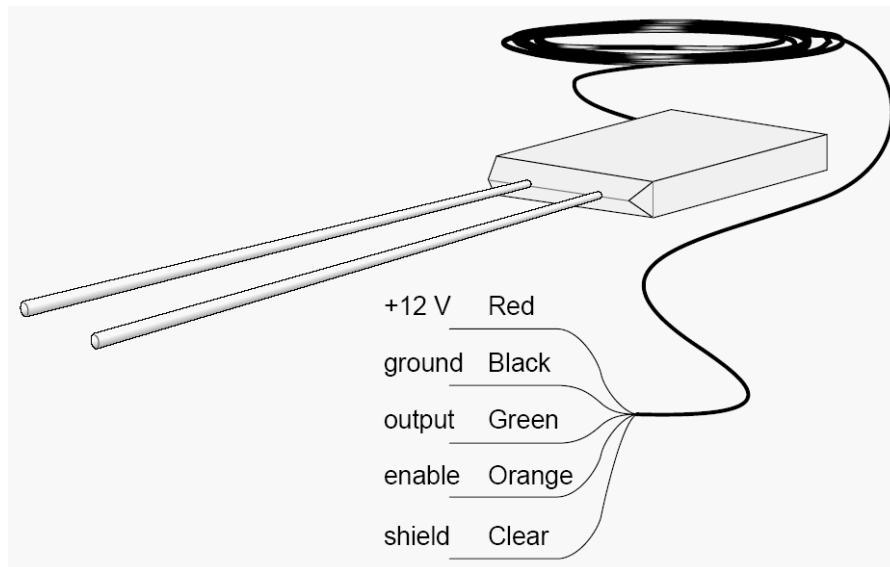
Figure 13. Campbell Scientific® reflectometer model CS615.

3.3.4 Temperature Sensors

Thermocouples were installed in the air and embedded in the test sections at several depths to monitor the pavement temperature and the air temperature over the test sections. The thermocouples have an accuracy of ± 0.5 C. The subsurface temperature sensors were installed at three horizontal locations within the test section in the asphalt concrete, base course, and at two depths into the subgrade.

Figure 14 displays a cross section of a typical test sections showing the locations of εmu coil sensors.
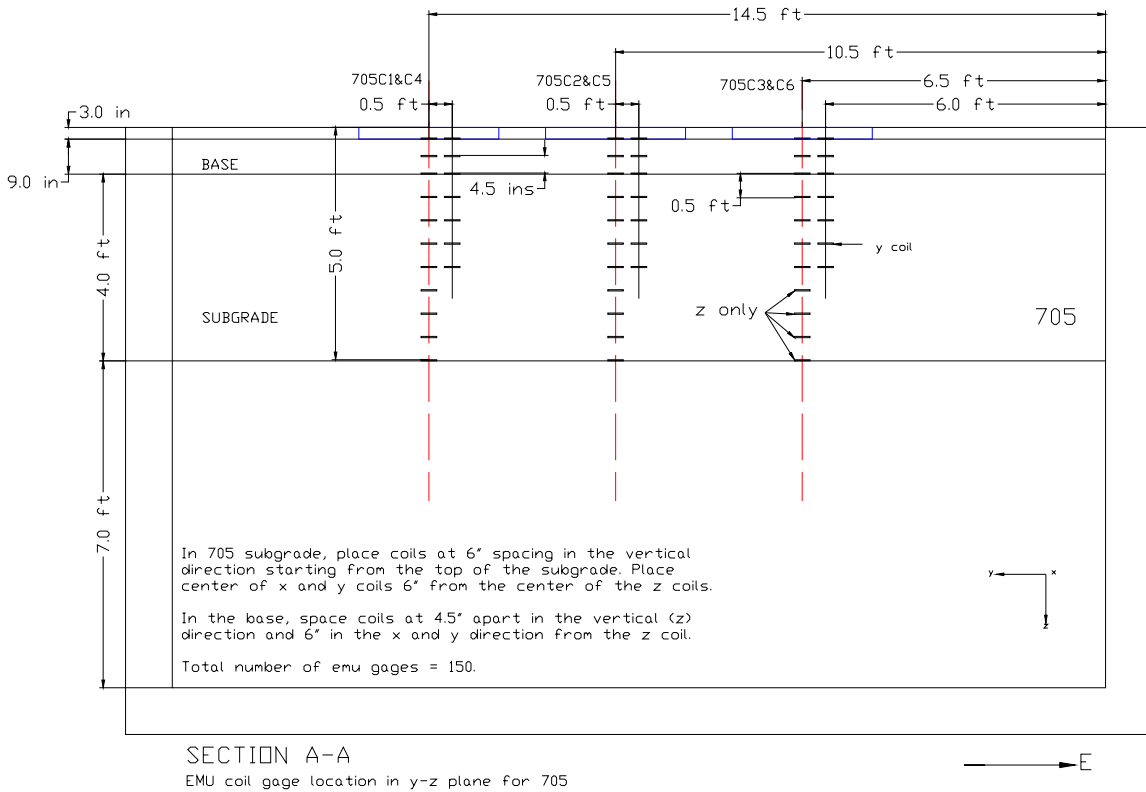
Figure 14. Cross section of test section showing ɛmu sensor locations.

3.4 Data Acquisition System

The temperature and soil moisture data were collected using a commercially available data logger recording one set of data every 4 hours.

The load-induced stresses, strains, and deformations were measured with the embedded sensors described above and their signals were processed and recorded by a custom-made data acquisition system. This was necessary because we could not find a suitable commercially available data logger. The ɛmu coil system requires specialized electronics and automation to acquire the data. The ɛmu coils must be read in small sets so that only one ɛmu coil is externally energized at a time. A system of relays is built into

the data acquisition system to measure the full set of coil pairs without interference. The

data acquisition system hardware and software were developed at CRREL by an in-house

team that included an electronic engineer, a LabView® programmer, and a pavement

engineer.

Figure 15 shows a part of the hardware of the data acquisition system. Among

other hardware, there are signal amplifiers, low-pass and hi-pass filters, and bridge

balancing adjustments.

Figure 16 shows another portion of the data acquisition system. This portion

contains the sensor input connections and a system of relays.

A personal computer houses the custom-made data acquisition software

developed in the LabView programming environment. Figure 17 shows a screen capture

from the data acquisition software that includes the display of εmu signals corresponding

to the vertical, longitudinal, and transversal.
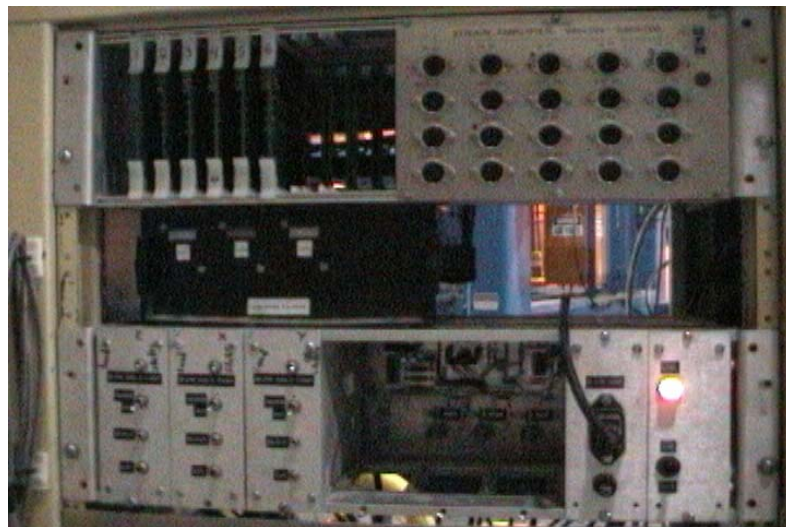
Figure 15. Signal conditioning hardware in the data acquisition system.
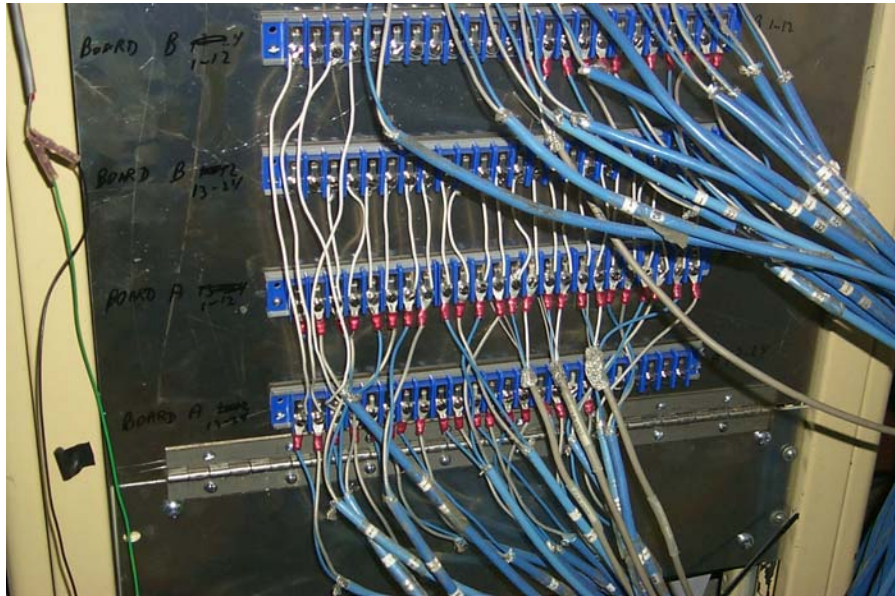
Figure 16.   mu connections and relay hardware.

Figure 17. Data acquisition software.

3.5 Construction of the Test Sections

The test sections were constructed indoors at the Frost Effects Research Facility (FERF) in Hanover, New Hampshire, using ordinary, full-size construction equipment as shown in Figure 18. However, the quality control standards were higher than those commonly found in field construction. The subgrade was placed and compacted in 152-mm (6-in.) layers.

Figure 18. Construction equipment.

The subgrade soil was placed in a moisture condition dryer than the final condition. The soil was spread and roto-tilled in place. Then, water was added in small increments using a volume meter control connected in line with a hose. The area was divided into elements to ensure that water was delivered uniformly throughout the test area. A nuclear moisture-density gauge was used as the primary quality control instrument to ensure that the target moistures and densities were achieved within a narrow tolerance band. Once the desired subgrade moisture was achieved, a steel roller

was used to obtain the desired density, according to the results of laboratory modified Proctor tests.

Once the moisture and density were attained, sensors were installed at the planned locations within the current soil layer. This process requires much care to ensure that every particle of soil removed during the sensor and cable installation is returned to its original location, and that the density and moisture are restored.

Figure 19. Nuclear moisture-density gauge measurements.

Figure 20. Sensor installation.

Figure 21. Ɛmu coils being installed.

This process continued layer by layer until the top of the subgrade. The soil layer

construction and sensor installation tasks were intertwined. Elevations were monitored

and adjusted with the help of a surveyor level. The elevation controls were most stringent

at the top of the subgrade, and later at the top of the base course. The base course was

placed in two equal layers through a process similar to that of the subgrade, but without

roto-tilling.

Paving of the test sections was done by a local contractor. The asphalt mixture

was produced at a local hot-mix asphalt (HMA) plant. The paving contractor provided a

grader machine to ensure uniform grade. The asphalt layer thickness was controlled

carefully to obtain uniformity throughout the test section. Mixture temperature during the

paving operation was monitored to ensure that compaction was conducted at an

appropriate temperature range. Density was monitored with a nuclear gauge set in the

backscatter mode.

Figure 22. Paving operation.

Figure 23. Nuclear gauge monitoring asphalt concrete density.

CHAPTER 4

ACCELERATED PAVEMENT TESTING

4.1 Definition

Accelerated pavement testing (APT) is the application of controlled traffic to a pavement structure to determine pavement response and performance in a compressed period of time. A heavy vehicle simulator (HVS) enables automated application of traffic loads of known intensity, speed, tire configuration, and tire pressure.

4.2 Purpose and Advantages of APT

The purpose of APT is to determine the performance of a pavement structure subjected to a given traffic regime in less time than an equivalent in-service pavement under conventional traffic (Hugo and Epps, 2004), with better control of traffic parameters, more precise measurements, and less risk to the public.

APT constitutes an effective, efficient, and safe way to evaluate new pavement materials (Perkins and Cortez, 2004), the effect of new vehicles, new tire configurations (Fernandes et al., 2006), and new design methodologies (Chen et al., 2006). Full-scale pavement test sections can be tested until distress is more severe than that permissible in pavements in service owing to liability concerns. For example, rutting in excess of 32 mm (1.25 in.) can be tolerated in APT experiments, while in field highway pavements, rutting is limited to less than half of this value to avoid accidents and related litigation.

APT can be used to develop, calibrate, and validate pavement models, particularly in facilities where the environmental parameters (i.e., air temperature, pavement temperature, moisture, etc.) can be controlled. One such facility is the FERF, where the experiments in this study were conducted.

APT on full-scale pavement test sections is an intermediate experimental method between small-scale laboratory experiments and uncontrolled field test sections. Laboratory triaxial tests on pavement materials can simulate repeated, cyclic loading, but they lack the stress rotations that occur in real pavements upon the rolling of traffic loads. Also, with rolling traffic loads, the magnitude and shape of the stress and strain signals differ between horizontal longitudinal and horizontal transversal directions. In laboratory triaxial tests the horizontal stresses and strains are symmetrical around the cylinder's axis.

APT can also be used to develop and validate construction, rehabilitation and maintenance strategies (Hugo, 2004).

Results from APT have been used to substantiate pavement management and road use taxation, such as delimiting the spring thaw weakening period (Saarelainen et al., 1999) and overload pavement utilization fees.

In pavement subgrade performance study, APT was used to establish load-response relationships for flexible pavements built with several subgrade soils, each at several moisture contents. The data collected from these experiments is used to support the development of pavement performance models and to evaluate other existing models.

4.3 CRREL's Heavy Vehicle Simulator

Accelerated traffic was applied to the test sections in this study by means of CRREL's Heavy Vehicle Simulator, hereafter simply referred as the HVS. The HVS was manufactured in South Africa by a division of Dynatest, Inc., headquartered in Florida. The model of the HVS is Mark IV

The HVS is 4 m wide, 23 m long and 4 m high [English units?]. The machine weighs about 45,000 kg (99,208 lb). The HVS is capable of using several tire sizes and types. In our experiments, the HVS tire assembly consisted of a set of dual tires. The tires were Michelin® model XZY-1 Accuride 22.5x8.25. Figure 25c shows the tire diameter, contact band width, and space between the tires.
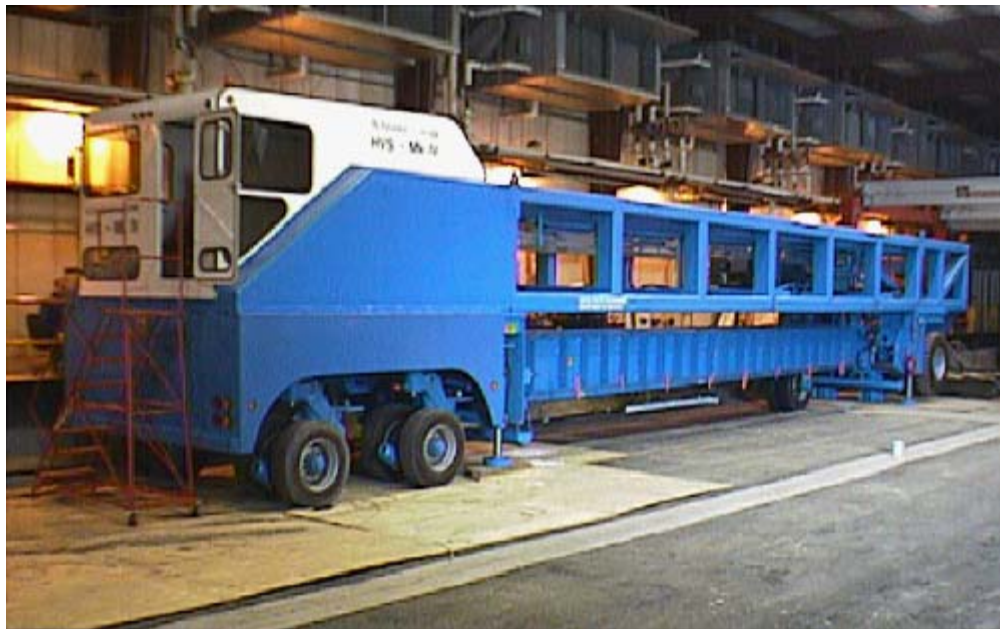
Figure 24a. Heavy vehicle simulator.

Figure 24b. Dual tire assembly.
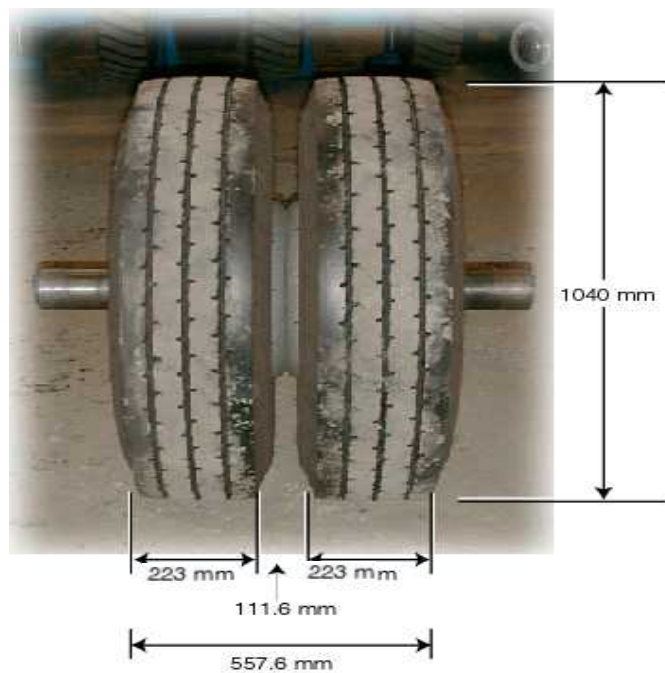
Figure 24c. Dual tire assembly dimensions.

The HVS is capable of applying load in the range from 18 to 200 kN (4 to 45 kips), provided that the tire used is also capable of supporting these loads. The HVS loads used in our experiments ranged from 18 to 97.9 kN (4 to 22 kips).

HVS loads are applied to one half of a standard axle. Therefore, to produce a standard 80-kN (18-kip) load, the HVS load must be 40 kN (9 kips) as illustrated in Figure 25. The interpretation of HVS loads reported in the literature must be conducted with this geometry in mind.
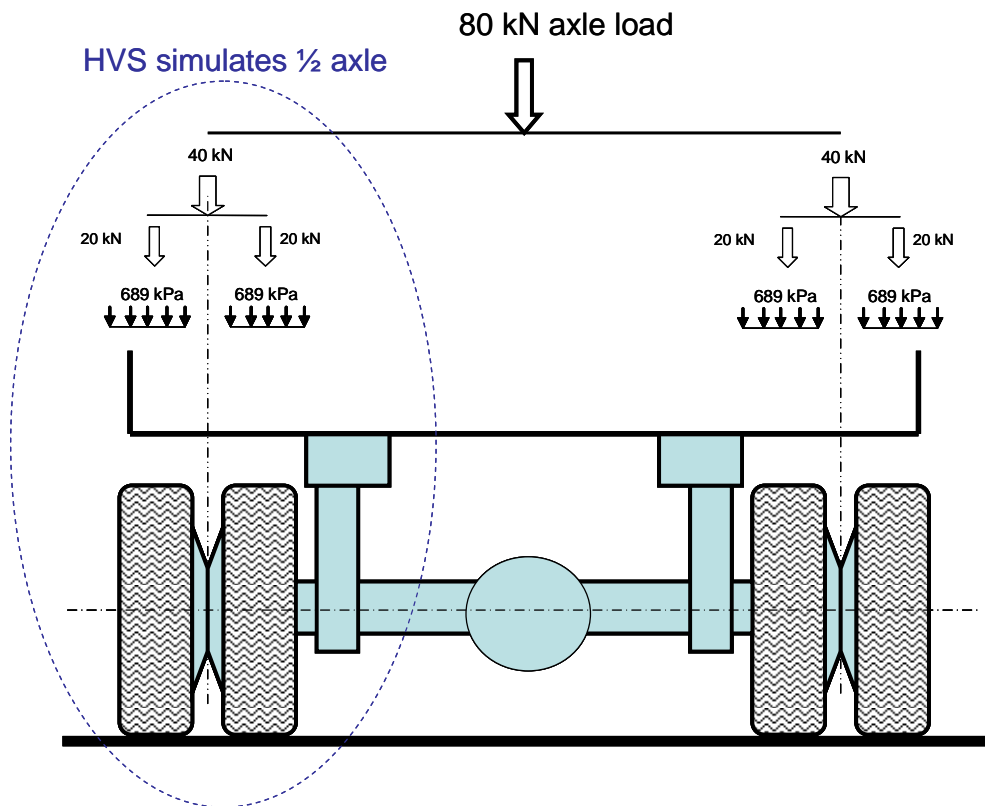
Figure 25. HVS ½ axle simulation.

As shown in Figure 26, the traffic tests were conducted unidirectionally at constant speed of 12 km/hr (7.5 miles/hr) over a pavement length of 6.1 m (20 ft), excluding acceleration and deceleration zones. The traffic speed in the HVS is limited by the mechanical strength of its components that must endure one event of rapid acceleration and one of rapid deceleration for each traffic pass. Speed is an important factor in the generation of stress and strain in a pavement structure (Lourens 1995).
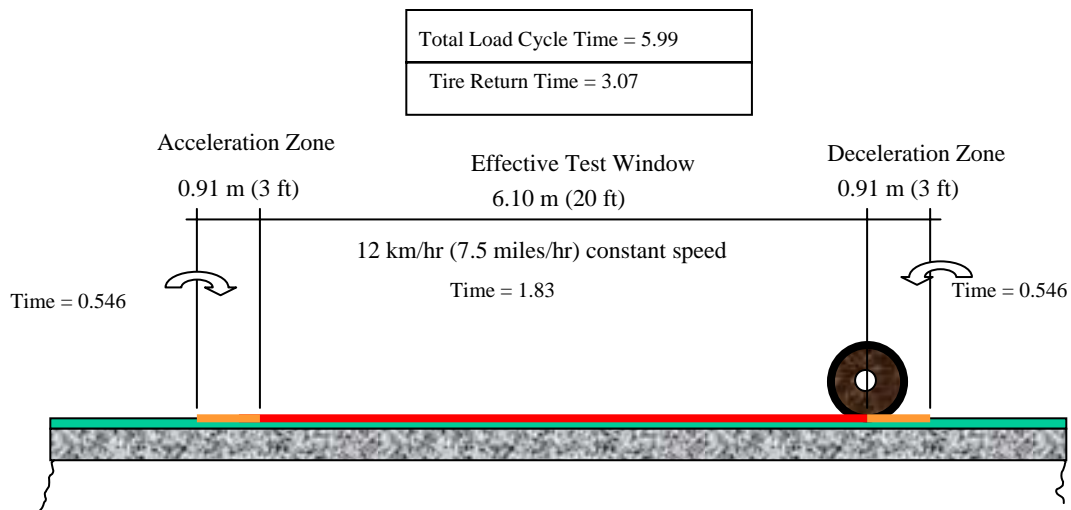
Figure 25. HVS traffic cycle.

The HVS produces the required traffic loads by means of a fast hydraulic system controlled by a wireless network of three computers.

The traffic on these experiments was evenly wandered over the test window so that a total width of 0.91 m (3 ft) would be contacted by the tires. The wander intervals were approximately 50 mm (2 in.).

Permanent deformation of the pavement surface (rutting) was measured before, after, and at various stages of the traffic tests. A laser profilometer made in South Africa by the HVS manufacturer was used to scan series of cross sections that helped monitor the development of rutting, longitudinally and transversally. The profilometer is controlled by specialized software hosted by a notebook computer. Figure 26 shows a view of the profilometer and Figure 27 shows a typical rutting cross section assembled from profilometer measurements.

Figure 26. Laser profilometer.
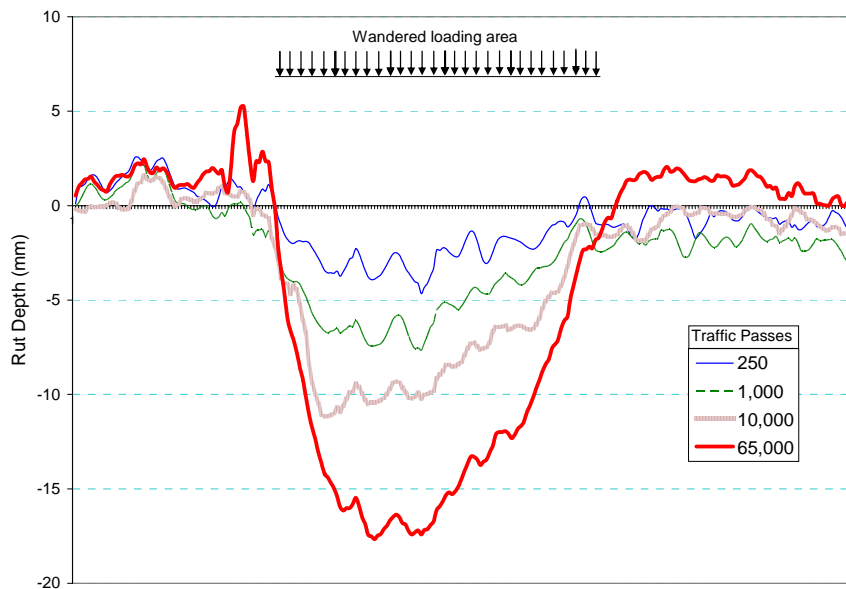
Figure 27. Typical rutting transversal cross section.

4.4 Frost Effects Research Facility

The experiments reported in this report were conducted in the Frost Effects

Research Facility (FERF). The FERF is a 2,700-m^2 (29,000 ft^2) environmentally

controlled building where full-scale pavement test sections can be built and tested year

round with the help of specialized equipment and staff. Powerful refrigeration and

heating equipment makes possible adequate control of temperature, and the closed-cell

design enables the control of soil moisture. Simulation and manipulation of a water table

is possible, but not used in this study. Ground freezing also is possible, but not used

during this project.

The FERF main building is 56 m (184 ft) long by 31 m (102 ft) wide. In addition,

the FERF has a soil storage building and a materials testing laboratory. Figure 28 shows

an outside view of the facility, and Figure 29 shows an inside view of the main testing

area.

Figure 28. Outside view of the FERF.

Figure 29. Inside view of the FERF.

The FERF capabilities are unique in that it has a heavy vehicle simulator coupled with a building equipped with powerful refrigeration and heating equipment that allows control of temperature, accelerated simulation of winters and water tables.

CHAPTER 5

TEST RESULTS

5.1 Data Management

The data collected in this study were very extensive. The data include:

1. Sensor spatial (x, y, z) location.

2. Sensor calibrations.

3. Material characterization tests.

4. Construction quality control tests.

5. Falling-weight deflectometry.

6. In-service moisture and temperature.

7. Applied load intensity.

8. Surface profilometry.

9. Static permanent deformation.

10. Dynamic resilient deformation.

11. Stress.

12. Forensic explorations.

Some of the above data, such as the construction quality control test data, were collected only to ensure compliance with the test plan. The experimental test data have been organized into a database for use by this and other researchers.

The test sections were numbered from 701 to 712. This numbering system was useful only during the execution of the experiments for project and data management. The relationships between test section numbers and the subgrade soil and moisture content are contained in Table 1.

5.2 Surface Permanent Deformation

5.2.1 Measurement Method

Surface vertical permanent deformation (rutting) represents the cumulative vertical deformation of the various layers within a pavement structure. In other words, the sum of the vertical deformations in the asphalt, base, and subgrade layers manifests itself at the top of the pavement in the form of rutting. Rutting measurements were obtained by means of a computer-controlled laser profilometer. Measurements conducted before traffic served as the baseline for subsequent measurements at the end of traffic and at several intermediate stages. Figure 27 show a typical rutting cross section. Figure 30 shows a typical longitudinal rutting graph. To build the longitudinal cross section, 20

transversal rutting cross sections were needed. Each data point on this graph represents the rutting at the center of the tire path over the effective test window. A test window is the area where the HVS traffic is applied. The effective test window is the area of the test window where full load is applied at constant speed. This excludes the acceleration and deceleration zones.
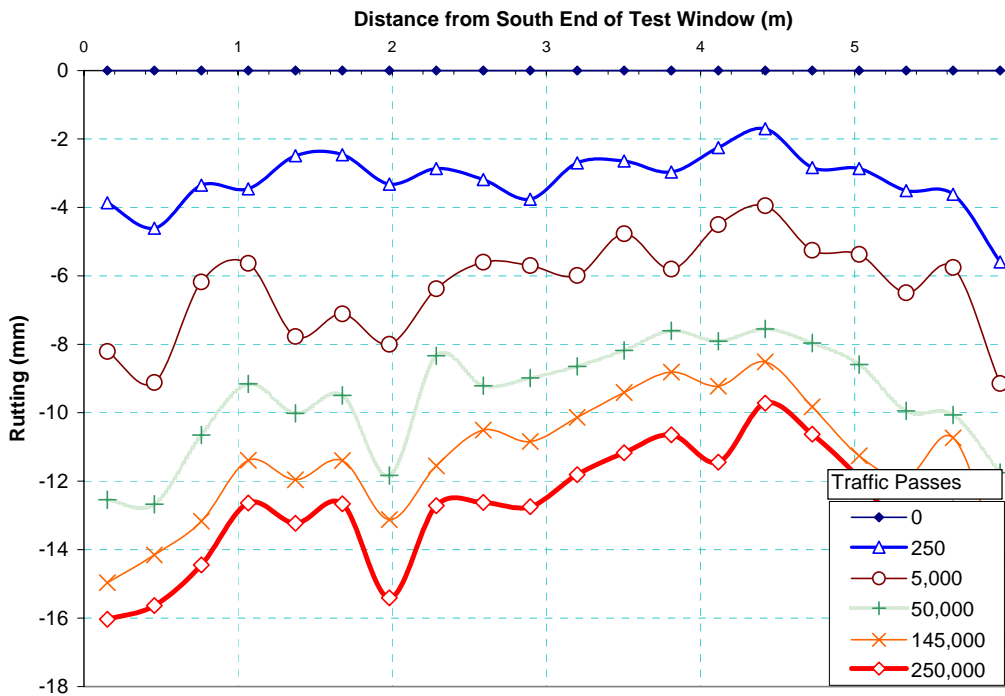
Figure 30. Typical longitudinal rutting graph.

From graphs such as Figure 30, the average rut depth of the longitudinal profile was plotted against the number of traffic passes; the results are shown in graphs such as Figure 31.

5.2.2 Subgrade AASHTO Type A-2-4

This subgrade soil is a mixture of sand, silt, and some gravel. Figure 4 shows the particle size distribution for this and the other subgrade soils used in this study. The portion of this soil that passed the standard sieve number 200 is referred to as "the fines portion." Atterberg tests on the fines portion of this soil indicated that this soil lacked cohesion. Although not measured in the laboratory, during the construction of the test sections, it was observed that water added on top of a layer of this soil drained rapidly to lower layers. Test sections 701, 707, and 703 were built with this subgrade soil conditioned at moisture contents of 10, 12 and 15%, respectively. The term "conditioned" is used here to indicate that, during the test section construction, the soil was placed first at relatively low moisture content, and then water was added until it reached the intended moisture content. The soil layer was then compacted to the specified density. According to modified Proctor tests, the optimum moisture content for this soil was 10% when the maximum density was 1934 kg/m^3 (120.7 lb/ft^3).
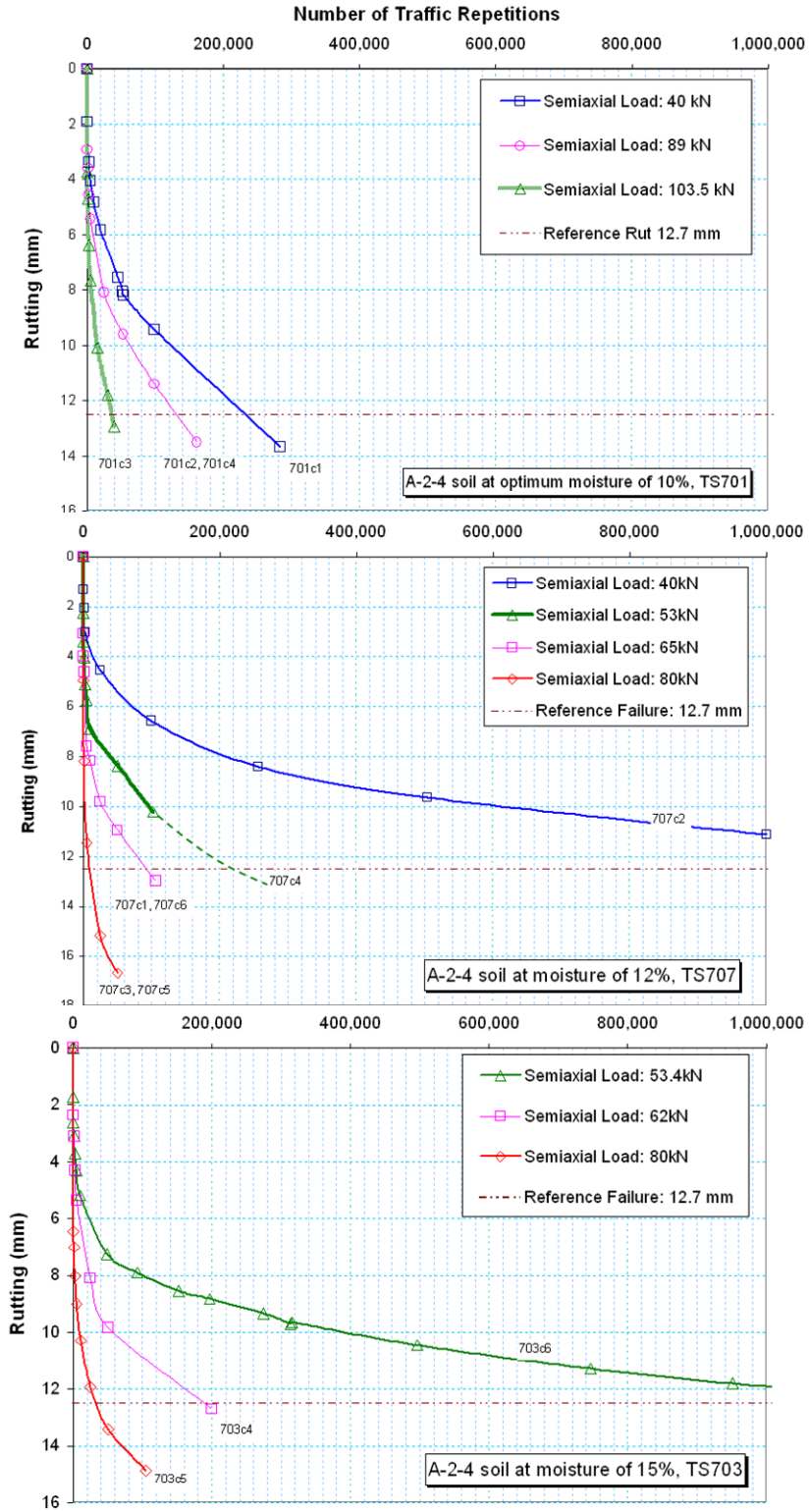
Figure 31. Rut development with A-2-4 subgrade soil.

5.2.3 Subgrade AASHTO Type A-4

      This is a silty soil that has low plasticity. The liquid limit was 28%, the plastic

limit was 10, and therefore the plasticity index was 18. According to the modified proctor

test, the optimum moisture content was 17% by weight, and its maximum density was

1780 kg/m^3 (111.1 lb/ft^3). Although not measured in the laboratory, during the

construction of the test sections, it was observed that water added on top of a layer of this

soil drained relatively fast to lower layers. Test sections number 702, 704, and 705 were

built with this subgrade soil conditioned at moisture contents of 17, 19 and 23%

respectively.
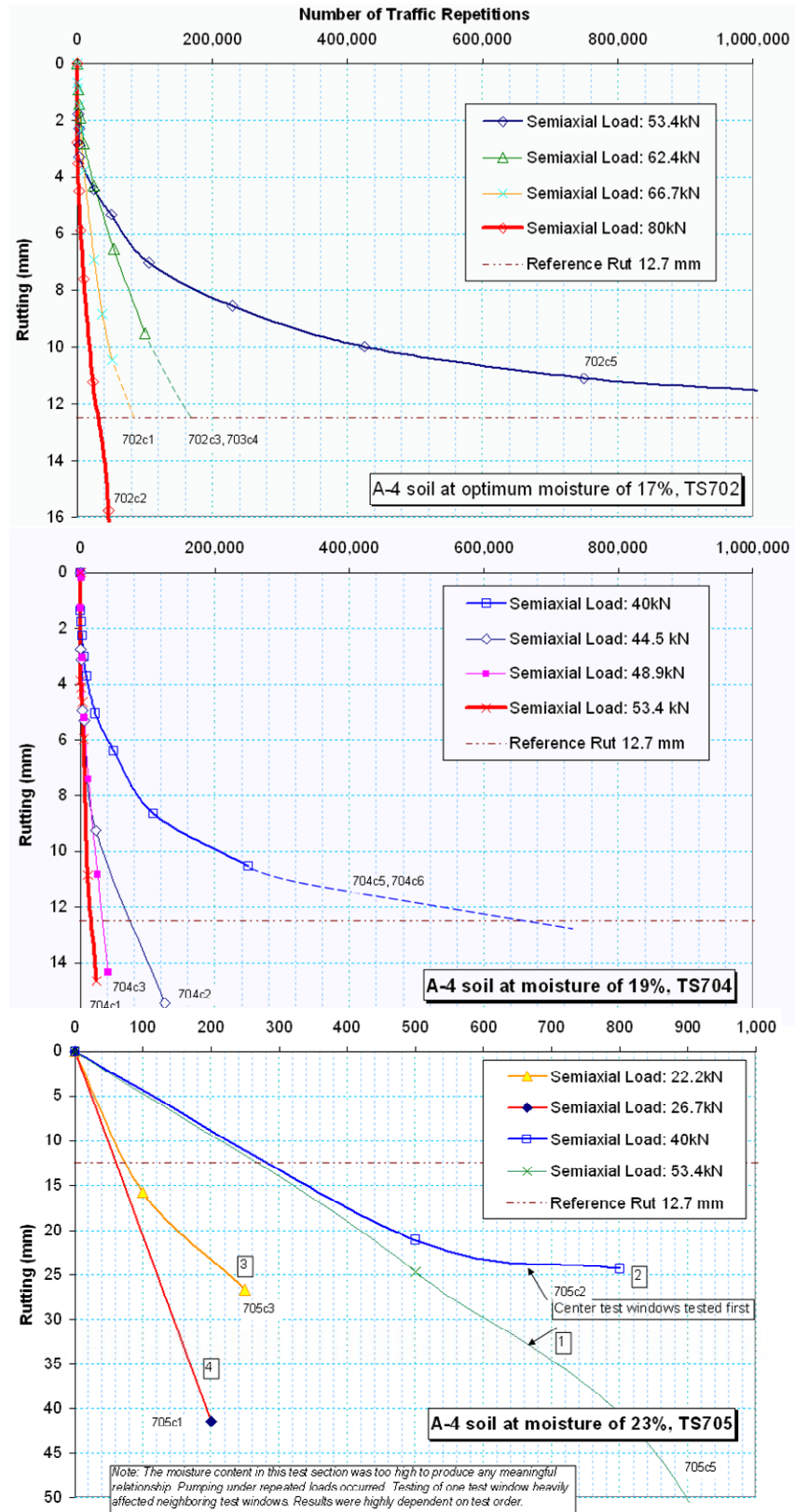
Figure 32. Rut development with A-4 subgrade soil.

5.2.4 Subgrade AASHTO Type A-6

This soil is classified as clay that has low-plasticity. According to the particle size distribution shown in Figure 4, this soil is a mixture of soil particles of silt with clay. Compared to the A-4 soil, the A-6 soil has higher clay content. The liquid limit was 29%, the plastic limit was 16, and therefore the plasticity index was 13. According to the modified proctor test, the optimum moisture content was 16% by weight, and its maximum density was 1791 kg/m^3 (111.8 lb/ft^3). Compared to the A-4 soil, this soil retained moisture more easily. During the construction of the test sections, it was observed that water added on top of a layer of this soil was absorbed more slowly than with the A-4 soil. Test sections number 709, 708, and 706 were built with this subgrade soil conditioned at moisture contents of 16, 19 and 22% respectively.
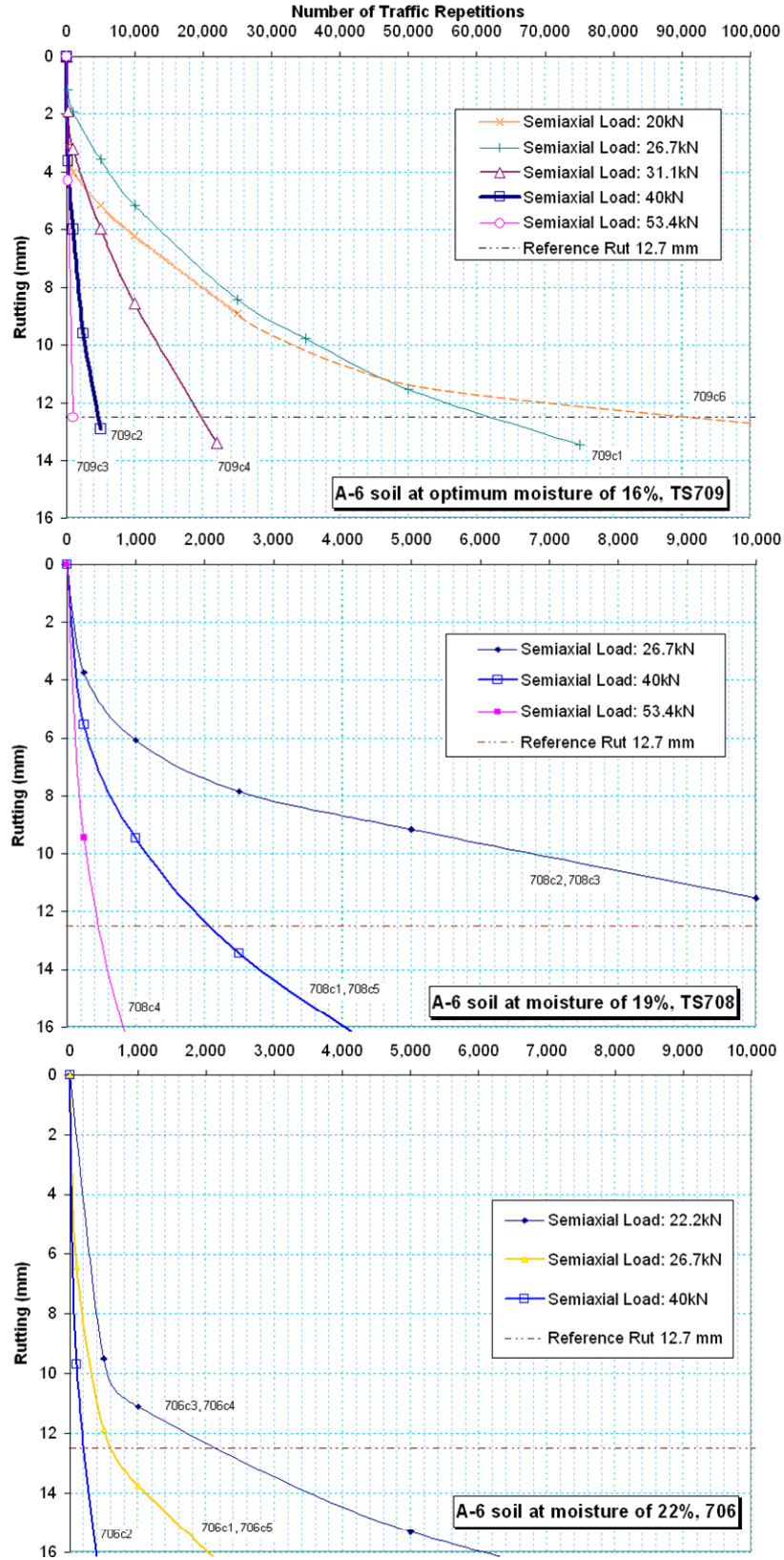
Figure 33. Rut development with A-6 subgrade soil.

5.2.5 Subgrade AASHTO Type A-6 / A-7-5

Soil classification is based on a combination of particle size analysis and Atterberg limits. An initial set of tests conducted on samples taken from the field excavation site indicated that this soil was type A-7-6. However, later tests conducted on representative samples from the delivered stock pile indicated a spread of liquid limit and plastic limit values that moved the classification to a zone spanning the soil types A-6 and A-7-6. Therefore, the soil was classified as a borderline soil between types A-6 and A-7-6. Moreover, the performance of the test section built with this subgrade soil was closer to that of the test sections built with soil classified as A-6. Although the soil classification systems have sharp transitions, real soils are more of a continuum in terms of their mixtures of silt and clay particles, and consequently, in terms of their behavior. The liquid limit was 40%, the plastic limit was 19, and therefore the plasticity index was 21. According to the modified proctor test, the optimum moisture content was 17% by weight, and its maximum density was 1800 kg/m^3 (112.4 lb/ft^3). Compared to the A-6 soil, this soil retained moisture more easily. During the construction of the test sections, it was observed that water added on top of a layer of this soil was absorbed more slowly than with the A-6 soil. Test section number 710 was the only one built with this soil. Because only one test section was built with this soil at one moisture level, its test results will be used in the data analysis only as reference.
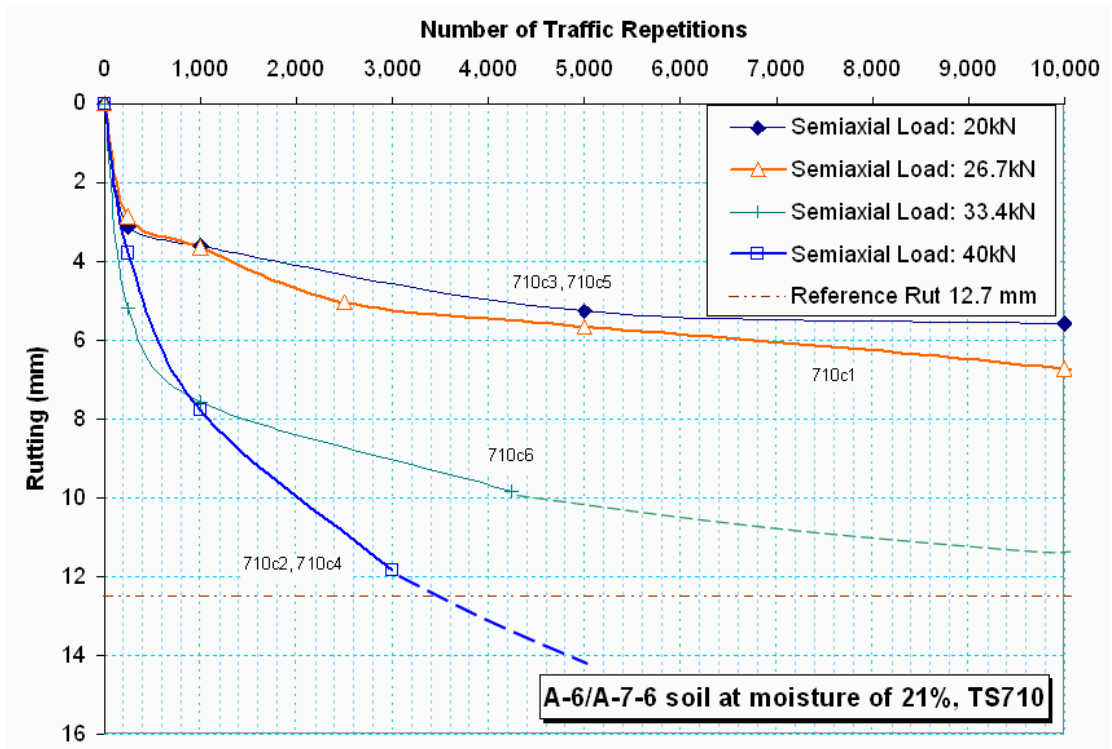
Figure 34. Rut development with A-6 / A-7-6 subgrade soil.

5.2.6 Subgrade AASHTO Type A-7-5

When this soil was procured, the intent was to find a soil classified as AASHTO A-7-6. An initial set of tests conducted on samples taken from the field excavation site indicated that this soil was type A-7-6. However, later tests conducted on representative samples from the delivered stock pile indicated a spread of liquid limit and plastic limit values that spanned the border between soil types A-6 and A-7-6, but the majority of measurements were within the A-7-5 zone. Therefore, the soil was classified as type A-7-5. The average liquid limit was 55%, the plastic limit was 34, and therefore the plasticity index was 21. According to the modified proctor test, the optimum moisture content was 20.5% by weight, and its maximum density was 1700 kg/m^3 (112.4 lb/ft^3). During the construction of the test sections, it was observed that water added on top of a layer of this

soil was absorbed slower than with the A-6 soil. The A-7-5 soil was clearly more

cohesive. The overall soil behavior was more clay like. Test sections number 712 and 711

were built with this soil at gravimetric moisture contents of 20 and 25% respectively.
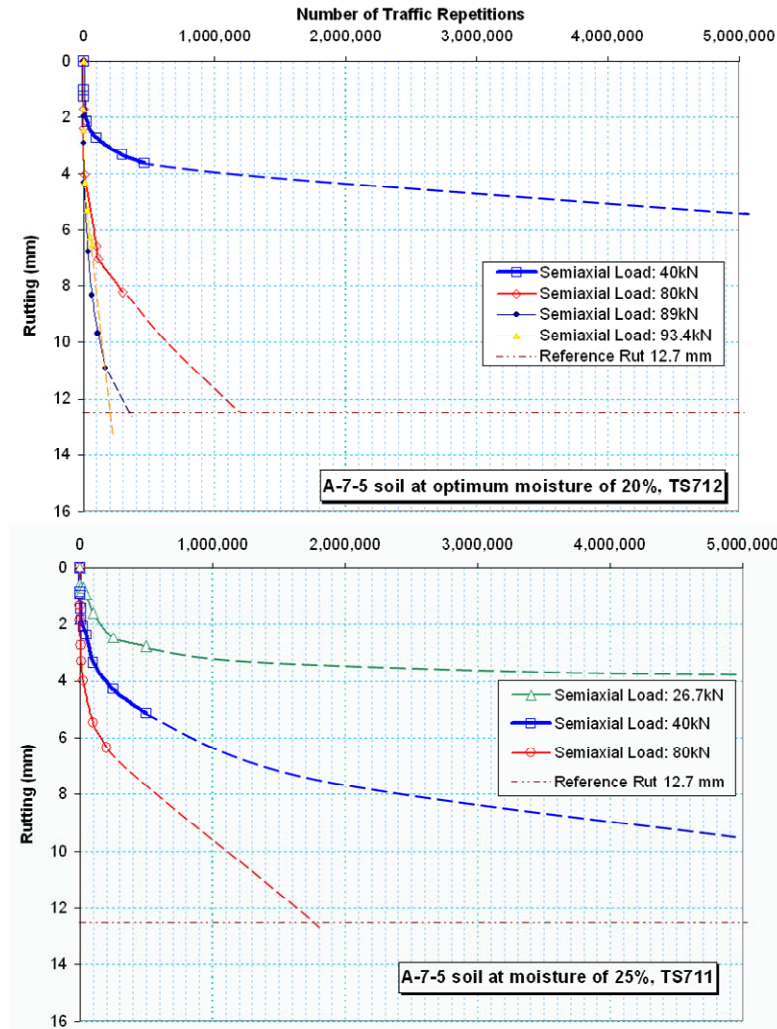
Figure 35. Rut development with A-7-5 subgrade soil.

5.2.7 Effect of Moisture on Traffic Repetitions to Failure

For this analysis, failure was defined as the development of 12.7 mm (0.5 in.) of

total pavement rut. For each subgrade soil type and each moisture level, Figure 36 shows

the number of traffic repetitions accumulated when the total rut depth on top of the

asphalt reached 12.7 mm. The data suggest that moisture significantly reduces the

number of traffic repetitions to failure, except for soil type A-2-4 where the trend was

reversed for the range of moisture values used in this study. Higher moisture conditions

may result in reduced performance for this soil as it did for the other soils.
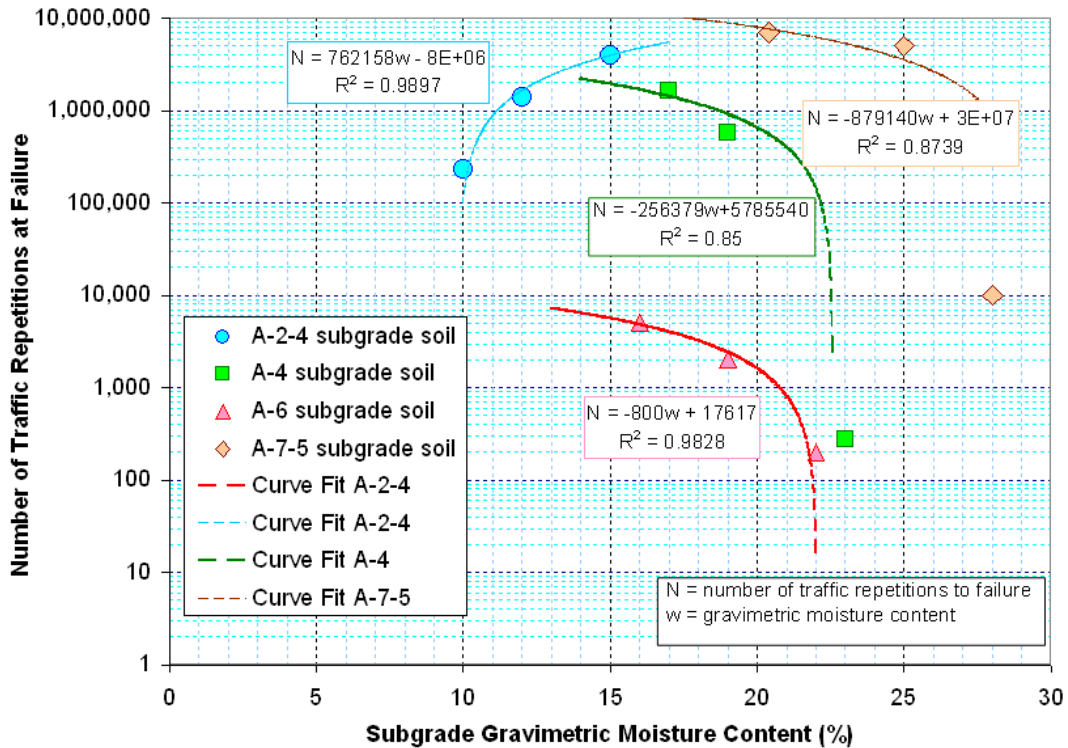
Figure 36.   Effect of Moisture on Traffic Repetitions to Failure.

5.3 Subsurface Permanent Deformation

5.3.1 Measurement Method

Stacks of εmu coils were embedded in the test sections. Three stacks of coils were

arranged so that measurements in the vertical, longitudinal, and transversal directions

could be obtained as shown in Figure 37. The vertical deformations in the lowest layers

were negligible for most test sections, except those with very wet subgrade soils. The

sum of vertical deformations in all the layers matched the surface rutting measured with the laser profilometer. A mobile coil was placed on top of the asphalt surface to make a pair with the shallowest coil located just beneath the asphalt layer. The permanent deformation in the asphalt layer was measured in this way. Because the horizontal components of deformation in the lowest layers are small compared to the signal noise, the lowest layers only contained vertical coil pairs.
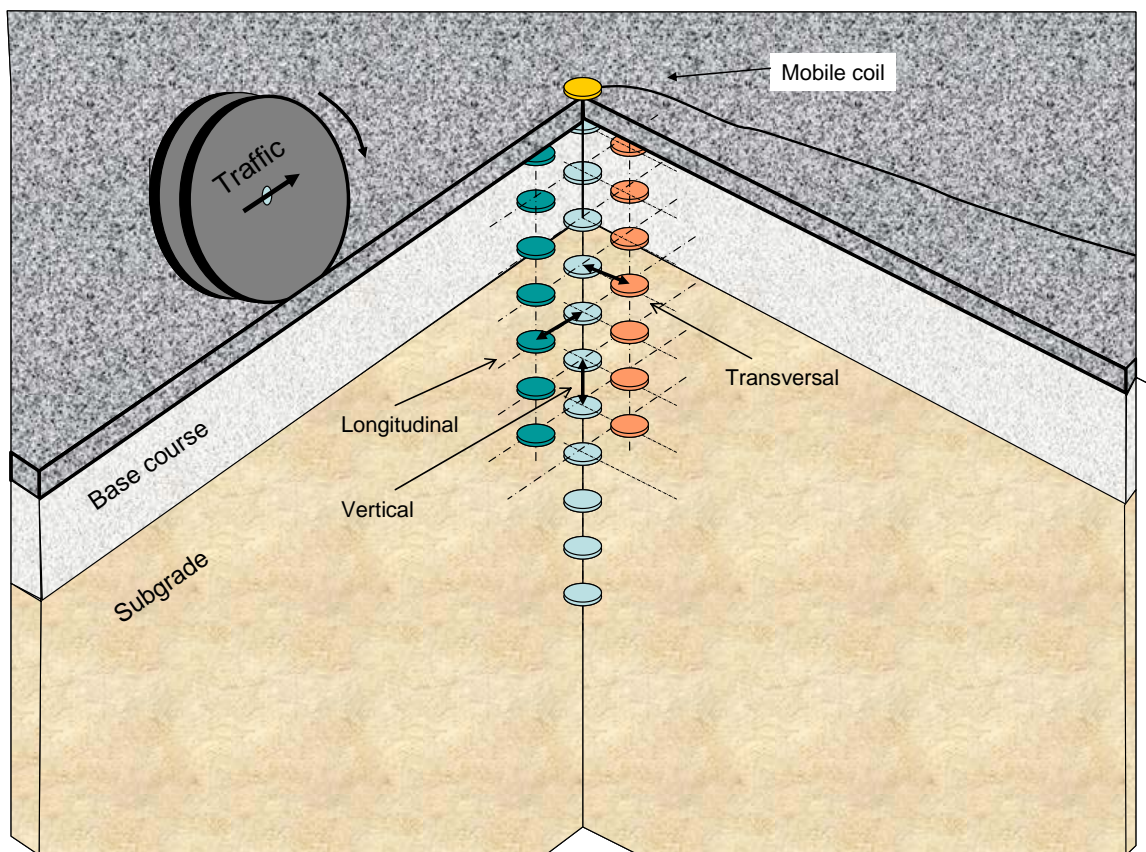
Figure 37. εmu coil stacks.

5.3.2 Subsurface Permanent Deformation with Subgrade AASHTO Type A-2-4

This subgrade soil was a mixture of sand, silt and gravel. Figure 4 shows the grain size distribution for this soil. One test section was built at optimum moisture content

determined by the modified proctor method to be 10 percent by weight. Two wet-of-
optimum test sections were built at 12 and 15 percent moisture. Comparing the rut
developments among these test sections, it appears that moisture contents in the range of
these experiments had beneficial effect. However, this trend may be reversed at higher
moisture content, bur this hypothesis was not tested in this study. Figure 38 suggests that
higher loads caused vertical deformations to grow deeper in the pavement structure.
Vertical deformations were higher near the top of the subgrade.

5.3.3 Subsurface Permanent Deformation with Subgrade AASHTO Type A-4

This was a silty subgrade soil with 17 percent optimum moisture content and
1780 kg/m^3 (111.1 lb/ft^3) maximum density. Permanent deformations grew deeper with
higher moisture content.

5.3.3 Subsurface Permanent Deformation with Subgrade AASHTO Type A-6

This was a silty clay subgrade soil with 16 percent optimum moisture content and
1791 kg/m^3 (111.8 lb/ft^3) maximum density. The distribution of permanent deformations
between the 16 and 19 percent moisture contents were very similar to each other. For the
case of the subgrade at 23 percent moisture content the deformations grew deeper and
larger with heavier loads.

5.3.4 Subsurface Permanent Deformation with Subgrade AASHTO Type A-7-5

This was a silty clay soil with higher clay content. Only two test sections were
built with this soil. The first test section the subgrade soil was at optimum moisture

content of 20 percent. The subgrade in the second test section was at 25 percent

gravimetric moisture content. The change of moisture contents between these test

sections did not caused significant changes in the permanent deformation measurements.

In both cases, the subgrade was relatively strong, and most of the vertical permanent

deformation occurred in the base course.

5.3.5 Subsurface Permanent Deformation with Subgrade AASHTO Type A6/A-7-6

The permanent deformation behavior in the test section built with this borderline

soil was similar to that of the test sections built with soil classified as A-6. At 21 percent

moisture content, this subgrade soil was relatively soft. Under these conditions, most of

the permanent deformation occurred in the subgrade, and with higher loads, the

deformations were deeper in the subgrade as shown in Figure 42.
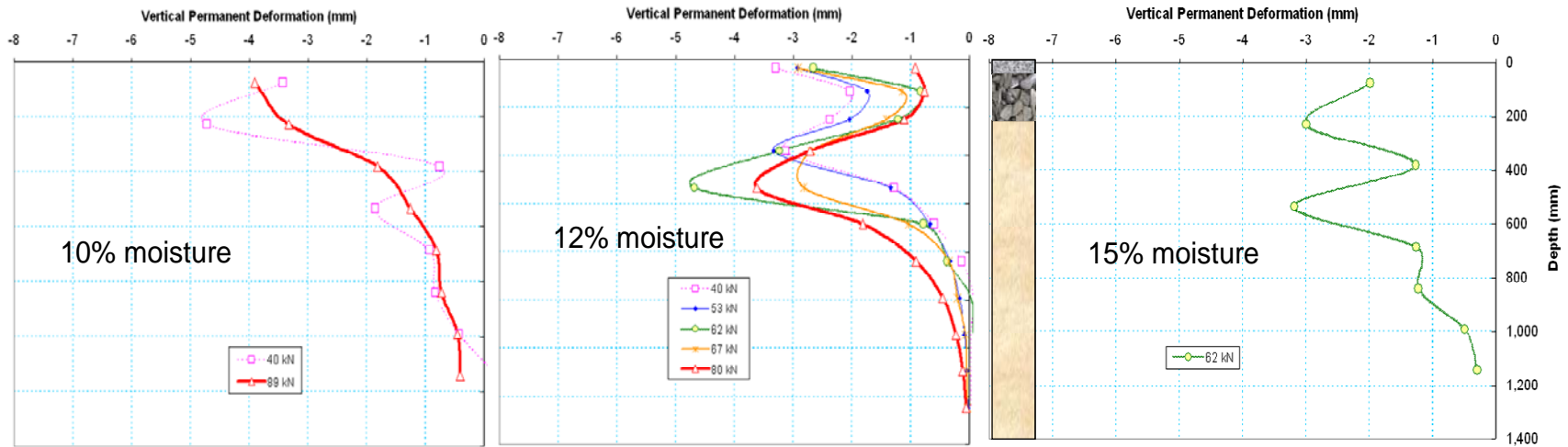
Figure 38. Subsurface deformation with subgrade soil type A-2-4.
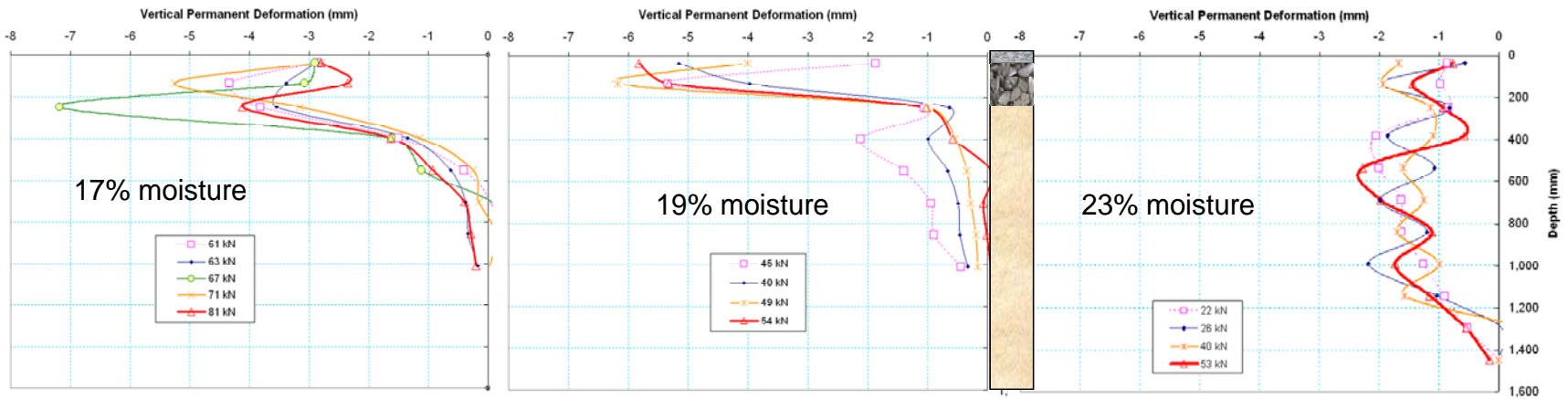
Figure 39. Subsurface deformation with subgrade soil type A-4.
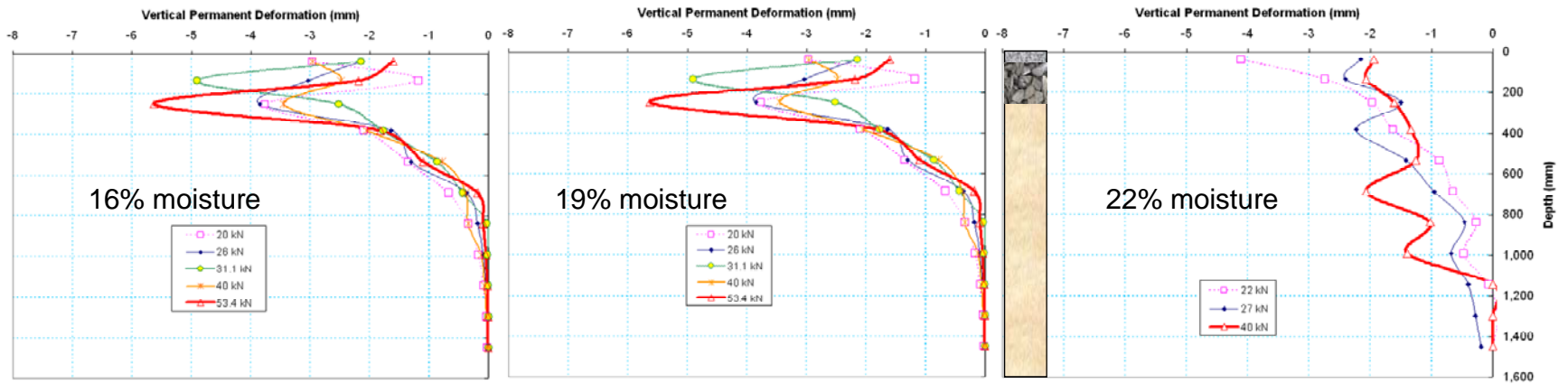
Figure 40. Subsurface deformation with subgrade soil type A-6.
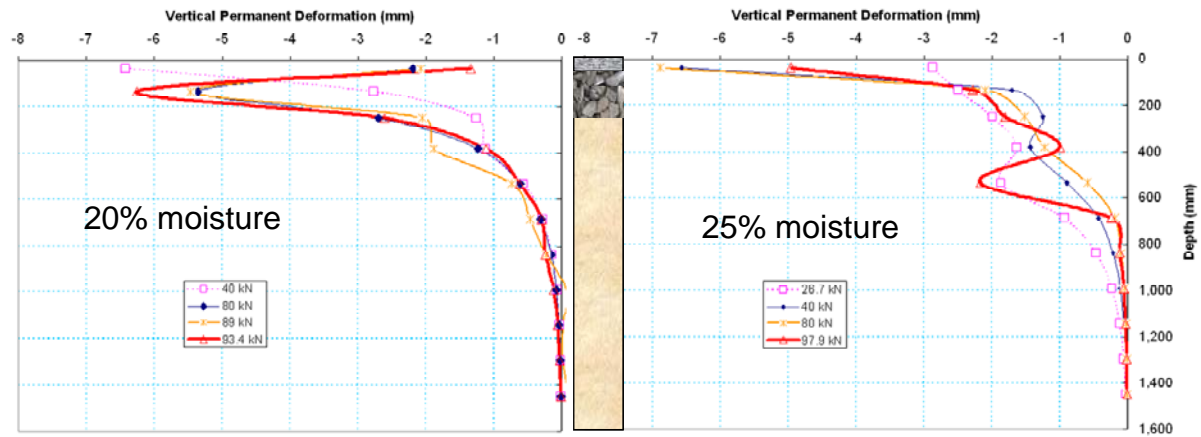
Figure 41. Subsurface deformation with subgrade soil type A-7-5.
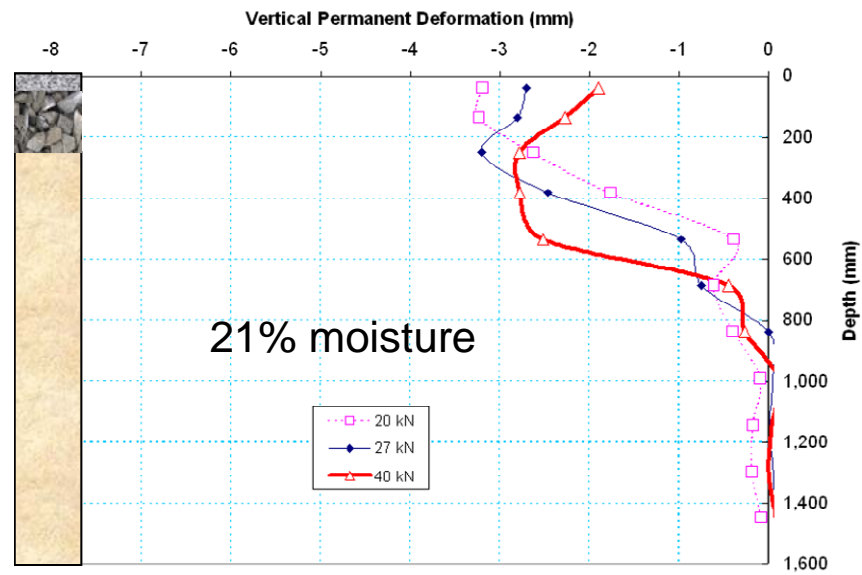
Figure 42. Subsurface deformation with subgrade soil type A-6 / A-7-6.

5.4 Subsurface Resilient Strain

5.4.1 Measurement Method

The same stacks of εmu coils embedded in the test sections that were described in section 5.3.1, were also used to make dynamic measurements of resilient deformation. In this case, the measurements were conducted while the tires were rolling and pressing down on the test window, applying the prescribed loads. During these measurements, the tire assembly was centered on the test window and no wander was allowed for the measurement passes. All other times, the HVS traffic was wandered as previously described. The signals generated by the moving iron mass in the wheel assembly were subtracted from the sensor output as described in section 3.3.1. The net sensor output was then converted to engineering units of deformation through the corresponding calibration curves as explained in section 3.3.1. Based on the initial distance between εmu coil pairs and the resilient deformation, resilient strain values were obtained.

5.4.2 Resilient Strain with Subgrade AASHTO Type A-2-4

Figures 43 and 44 show resilient strain measurements taken at a series of traffic pass levels. Resilient strains initially increased as the number of traffic passes increased and then remained practically constant. This behavior is known as strain hardening. This was the case for both the base and the subgrade at various moisture contents and load intensities. The measurements shown in Figure 44b at a depth of 534 mm are an exception to this trend. The reason for this difference was not established.

The data shows that resilient strain was largest in the middle of the base course. Resilient strain decreased with depth in the subgrade.
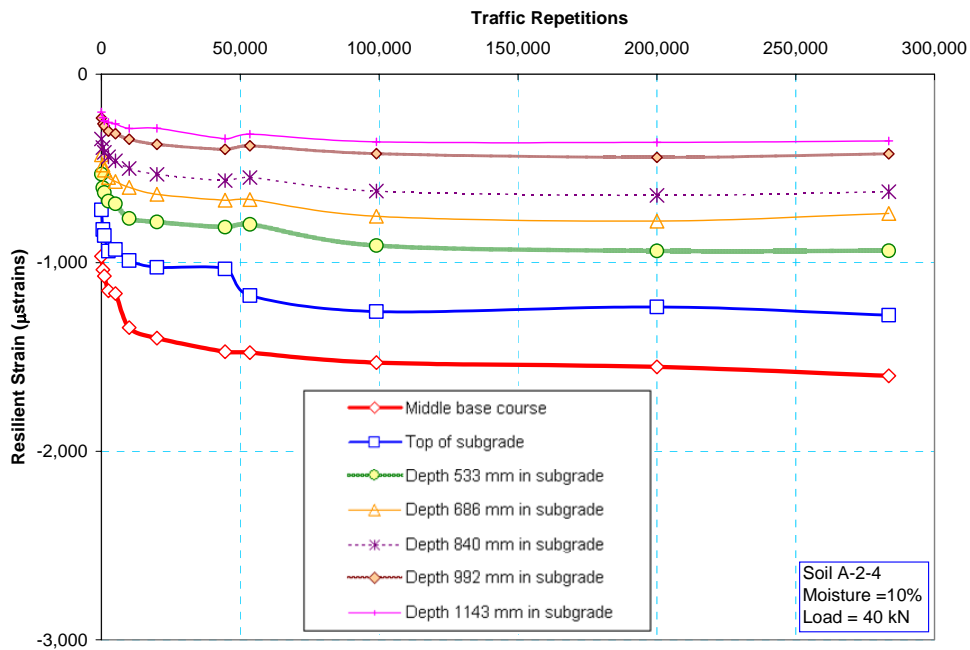
Figure 43a. Resilient deformation with subgrade soil type A-2-4 at 10% moisture content and 40 kN HVS load.
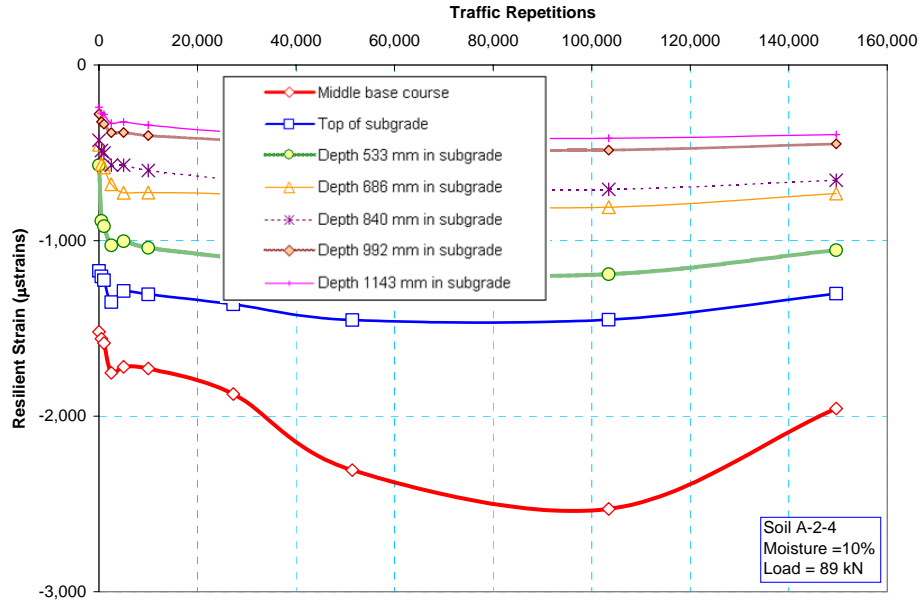
Figure 43b. Resilient strain with subgrade soil type A-2-4 at 10% moisture content and 89 kN HVS load.
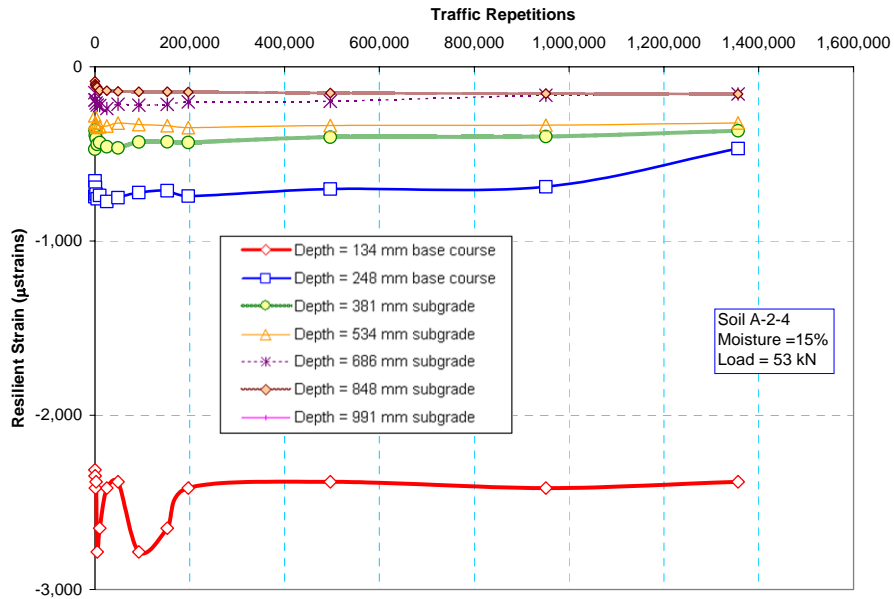
Figure 44a. Resilient strain with subgrade soil type A-2-4 at 15% moisture content and 53 kN HVS load.
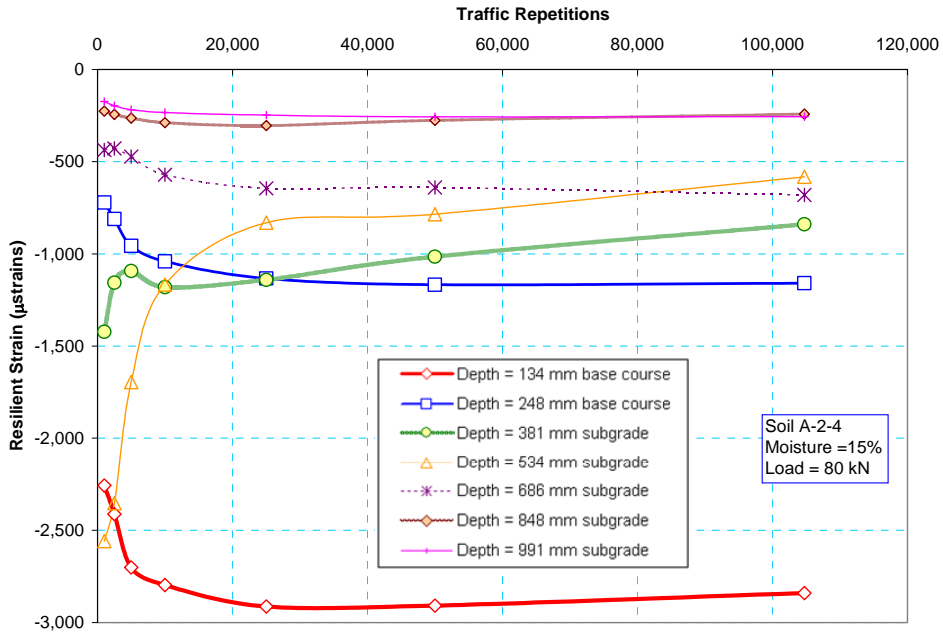
Figure 44b Resilient strain with subgrade soil type A-2-4 at 15% moisture content and 80 kN HVS load.

5.4.3 Resilient Strain with Subgrade AASHTO Type A-4

For most of the resilient strain measurements, there was an initial gradual increase with traffic repetitions followed for constant values for the rest of the traffic repetitions. resilient strain increased. At optimum moisture condition, higher loads increased the strains primarily in the base course and the top of the subgrade. Deeper locations were not significantly affected by higher load intensity.

Comparing Figures 45a and 46b, it can be seen that the increase in moisture content caused significant increase in the strain at the top of the subgrade.
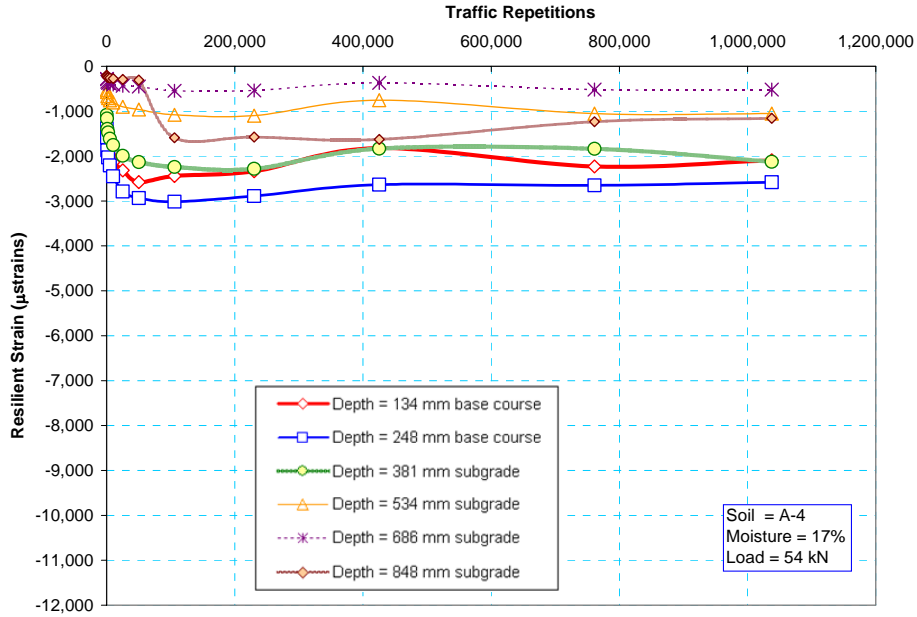
Figure 45a. Resilient strain with subgrade soil type A-4 at 17% moisture content and 54 kN HVS load.
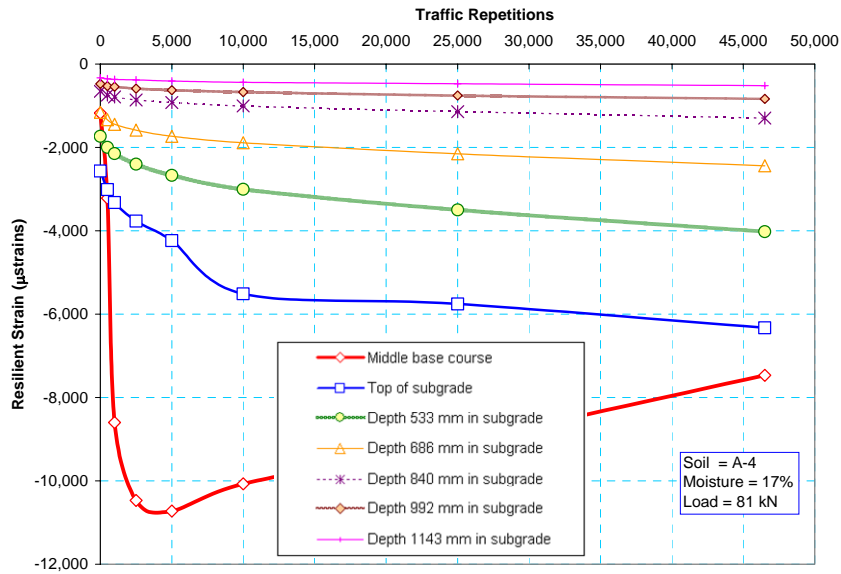
Figure 45b. Resilient strain with subgrade soil type A-4 at 17% moisture content and 81 kN HVS load.
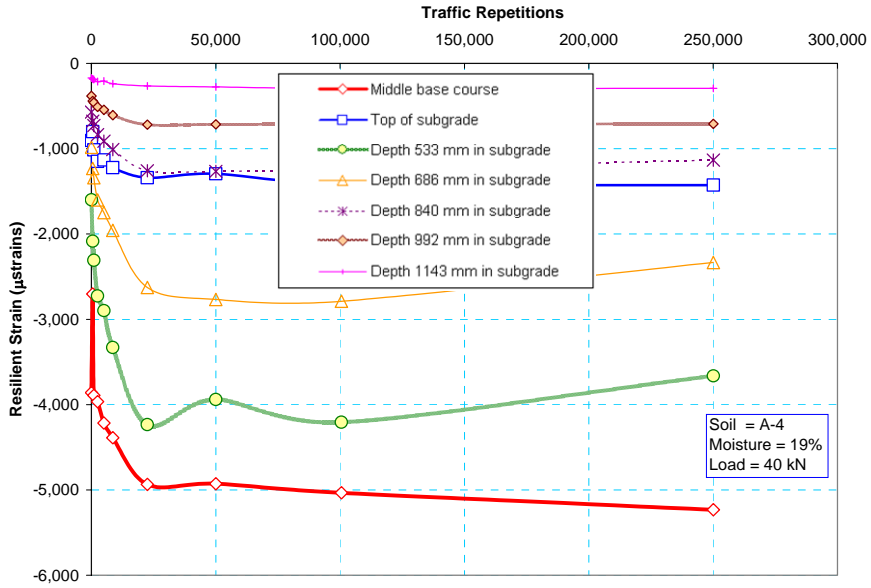
Figure 46a. Resilient strain with subgrade soil type A-4 at 19% moisture content and 40 kN HVS load.
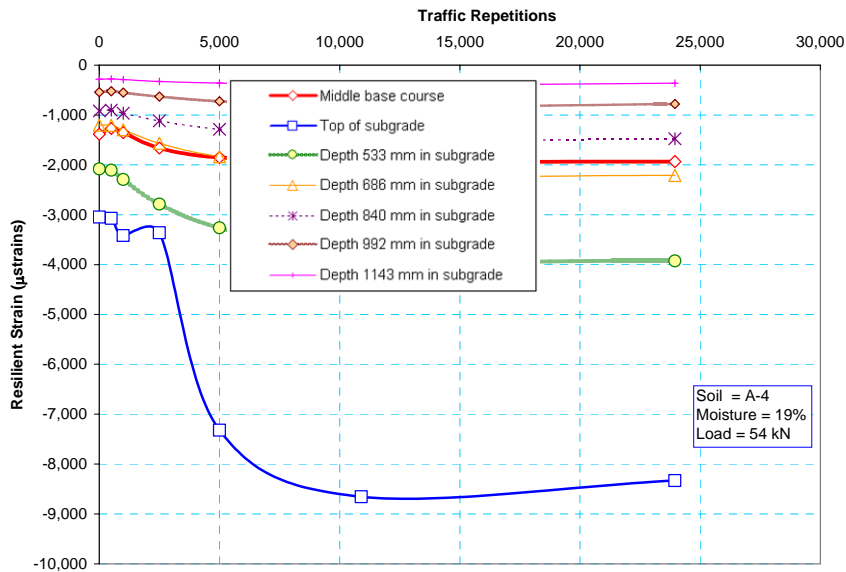
Figure 46b. Resilient strain with subgrade soil type A-4 at 19% moisture content and 54 kN HVS load.

5.4.4 Resilient Strain with Subgrade AASHTO Type A-6

Unlike the trends observed in test sections with other soil types, the largest resilient strains with subgrade soil type A-6 were located at the top of the subgrade for all load intensities, but the strains grew deeper into the subgrade as the subgrade moisture content increased.
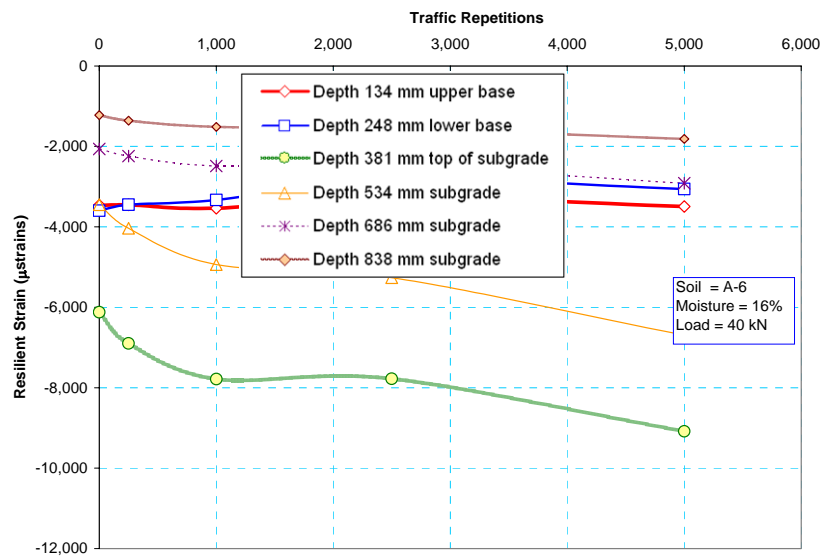
Figure 47a. Resilient Strain with subgrade soil type A-6 at 16% moisture content and 40 kN HVS load.
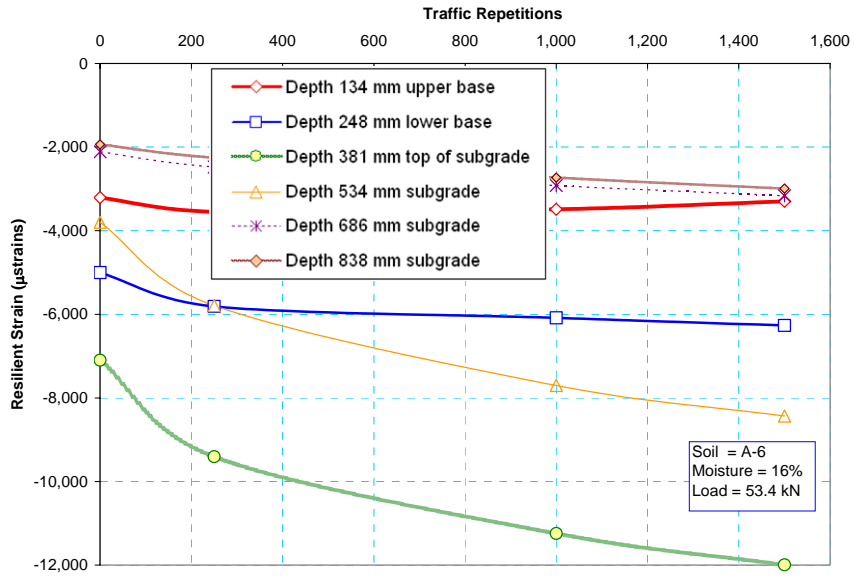
**Figure 47b. Resilient Strain with subgrade soil type A-6 at 16% moisture content
and 53.4 kN HVS load.**
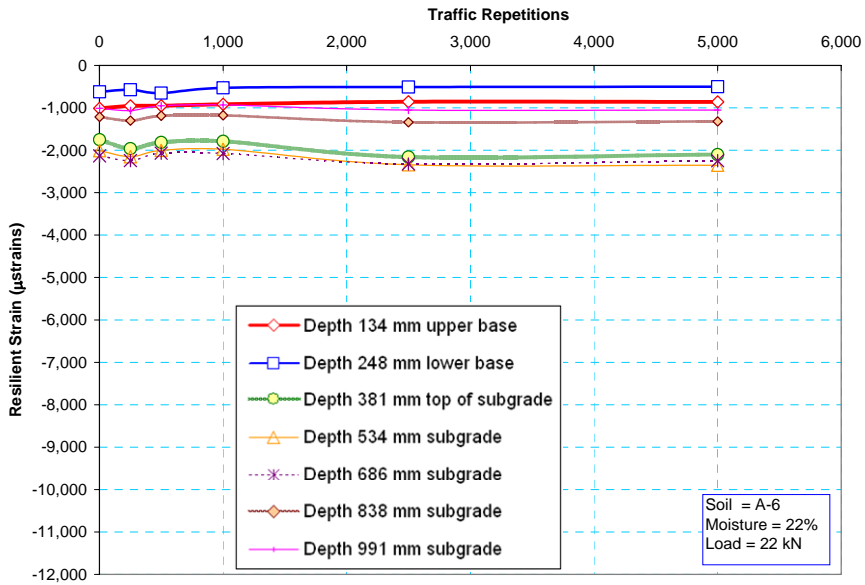
**Figure 48a. Resilient Strain with subgrade soil type A-6 at 22% moisture content
and 22 kN HVS load.**
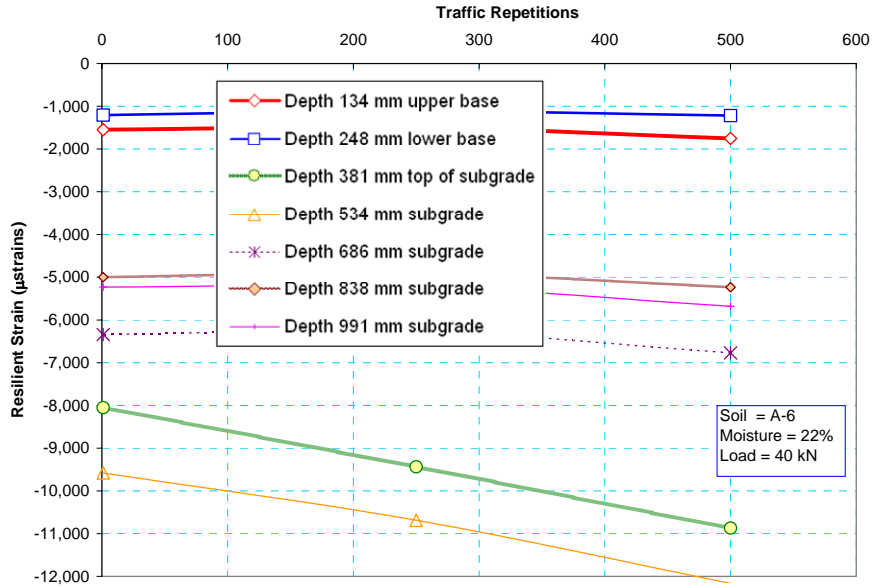
Figure 48b. Resilient strain with subgrade soil type A-6 at 22% moisture content and 40 kN HVS load.

5.4.5 Resilient Strain with Subgrade AASHTO Type A-7-5

Within the range of subgrade moisture contents included in these experiments, the subgrade remained relatively strong throughout the traffic tests. The resilient strains remained almost constant at most depths within the subgrade, but changed more in the base course. For the upper locations, resilient strain increased proportional to load intensity.
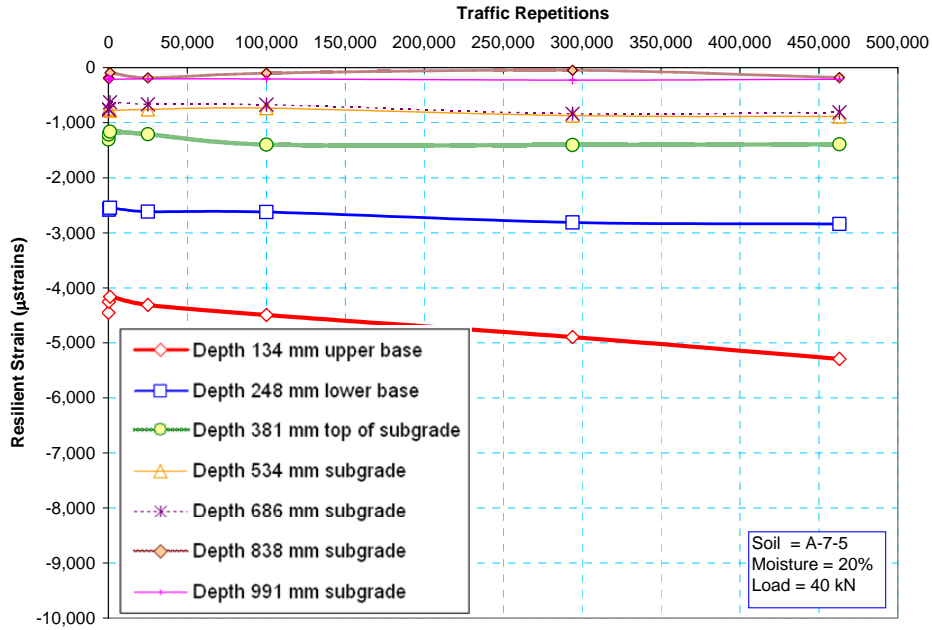
Figure 49a. Resilient strain with subgrade soil type A-7-5 at 20% moisture content and 40 kN HVS load.
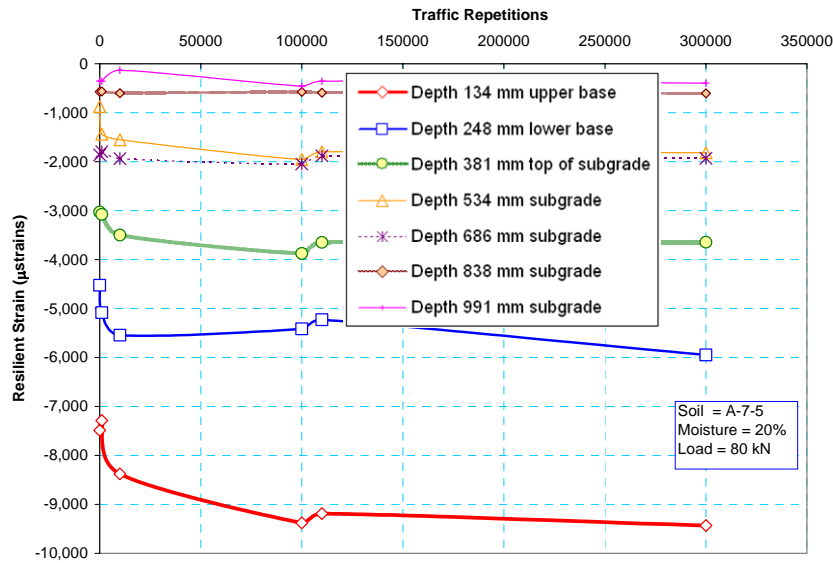
Figure 49b. Resilient strain with subgrade soil type A-7-5 at 20% moisture content and 80 kN HVS load.
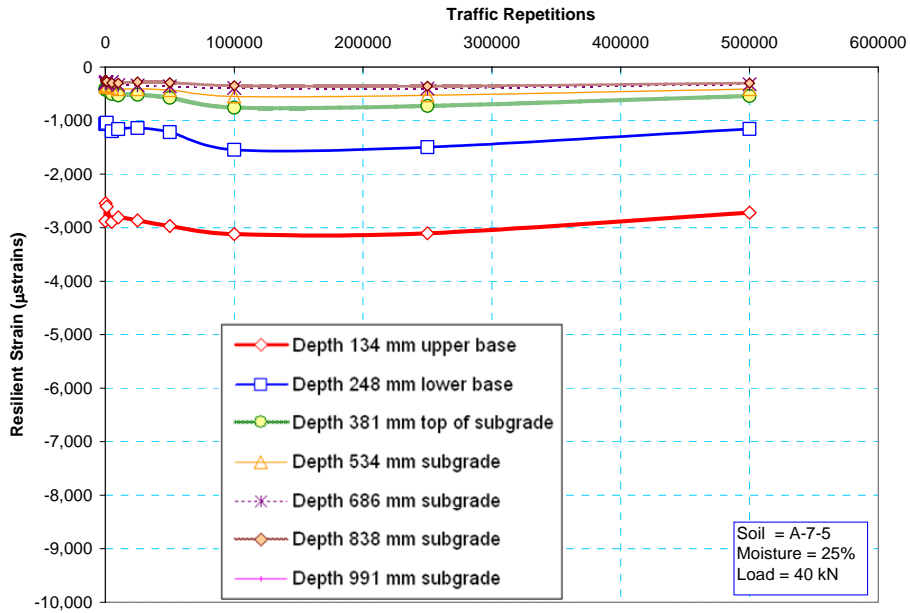
**Figure 50a. Resilient strain with subgrade soil type A-7-5 at 25% moisture content and 40 kN HVS load.**
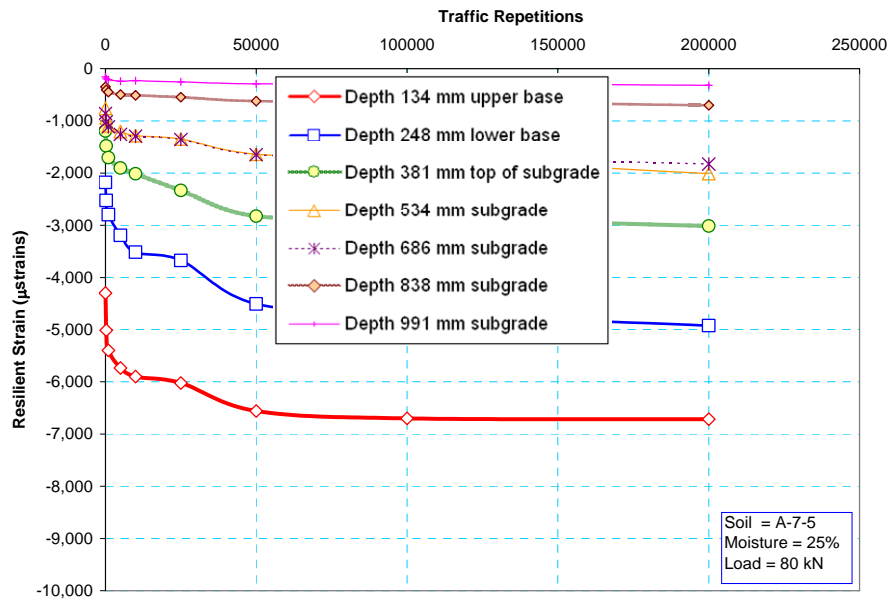

Figure 50b. Resilient strain with subgrade soil type A-7-5 at 25% moisture content and 80 kN HVS load.

5.5 Stress

5.5.1 Measurement Method

Stress cells were installed at various locations within the base and subgrade layers. Two types of stress cells were used: Geokon® earth pressure cells in the base and subgrade, and Dynatest® pressure cells in the subgrade. The larger Geokon cells were appropriate for both the base course material and for the fine-grained subgrades. The smaller Dynatest cells were appropriate for the subgrade, but were too small for measurements with the larger particles found in the base course. More detailed description of these sensors can be found above in section 3.3.2. Most measurements were conducted while the loaded tires were rolling over the test window containing sensors located under the center line of the tire path. The survivability rate of the stress sensors was poor. Some of the Geokon stress cells leaked oil and had to be refurbished for use in the latter test sections. Some of the Dynatest sensors broke within the sensor (open circuit), and some of the signal conditioning electronic components failed at various points. This resulted in significant number of stress measurements missing.

5.5.2 Stress Data

The following graphs show the test data from selected test windows for each combination of soil and moisture content. The complete set of measurements can be found in the project database contained in the attached compact disc.

Generally, stress increased as the load intensity increased, but the relation was non-linear. Additionally, as the load intensity increased, there was re-distribution of stress from the upper layers to lower layers.
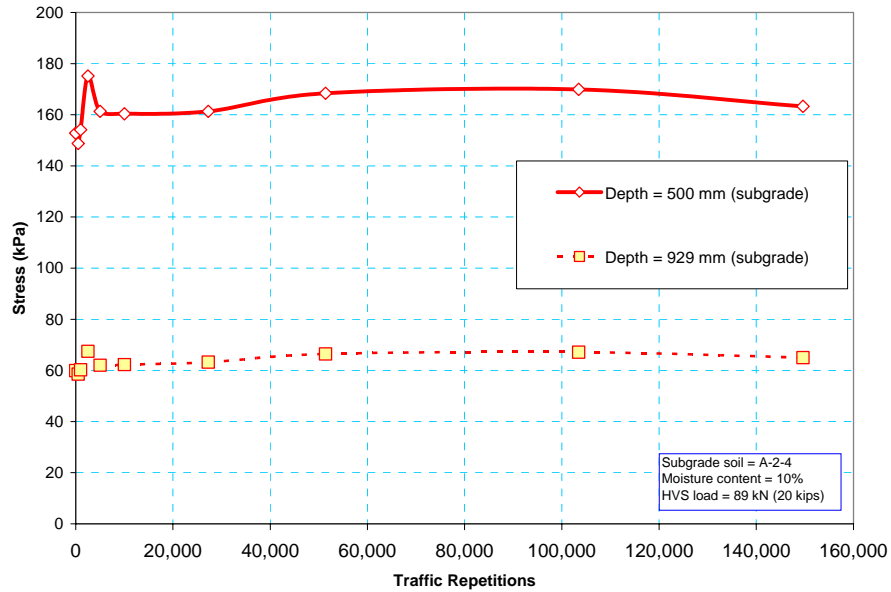
Figure 51a. Stress with subgrade A-2-4 at 10% moisture and HVS load of 89 kN.
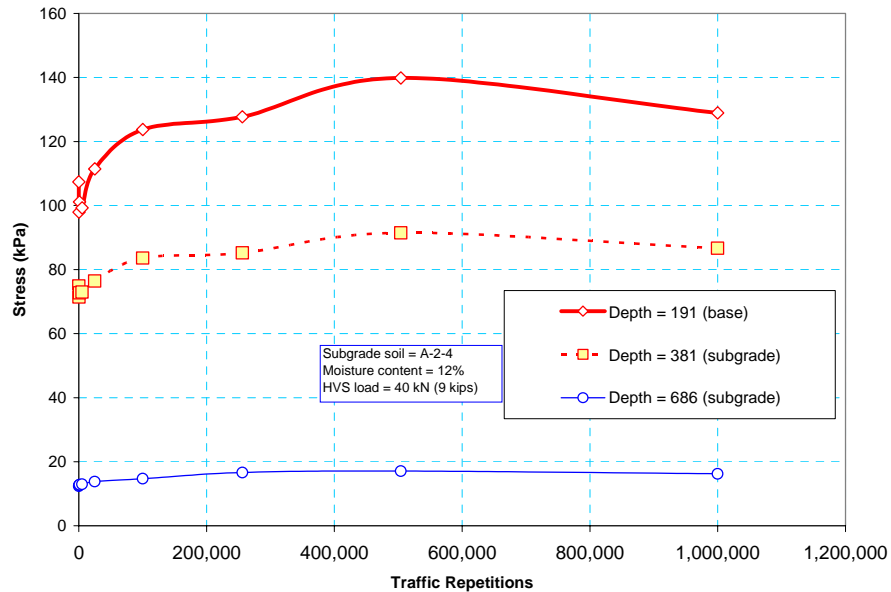
Figure 51b. Stress with subgrade A-2-4 at 12% moisture and HVS load of 40 kN.
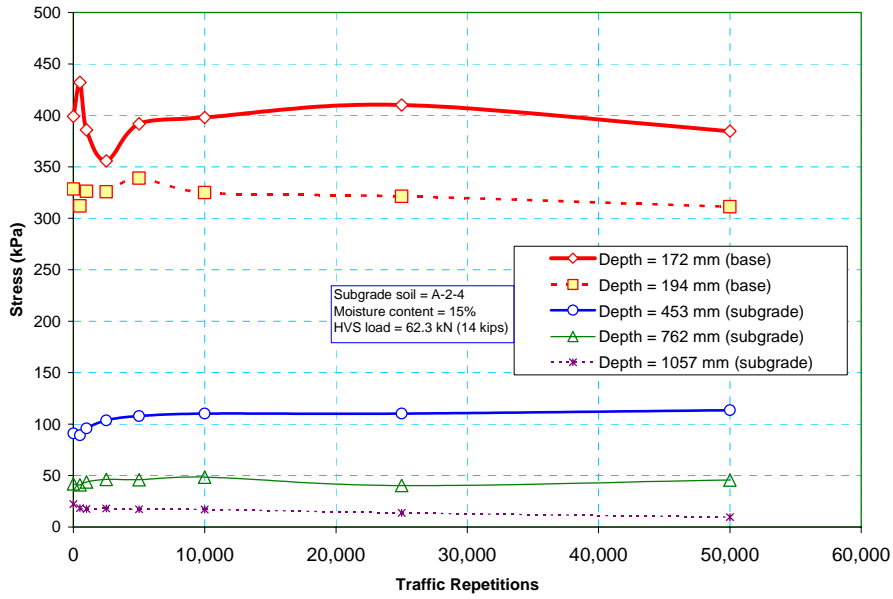
Figure 51c. Stress with subgrade A-2-4 at 15% moisture and HVS load of 62.3 kN.
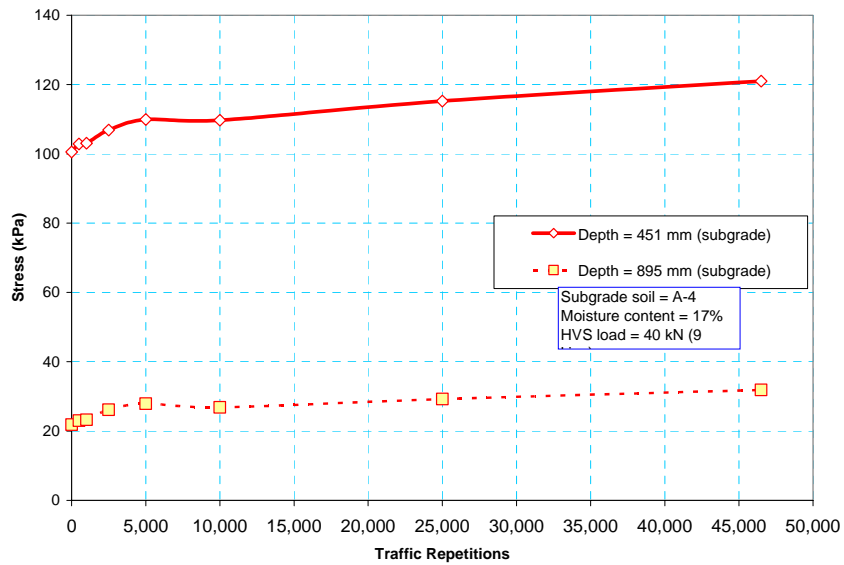
Figure 52a. Stress with subgrade A-4 at 17% moisture and HVS load of 40 kN.
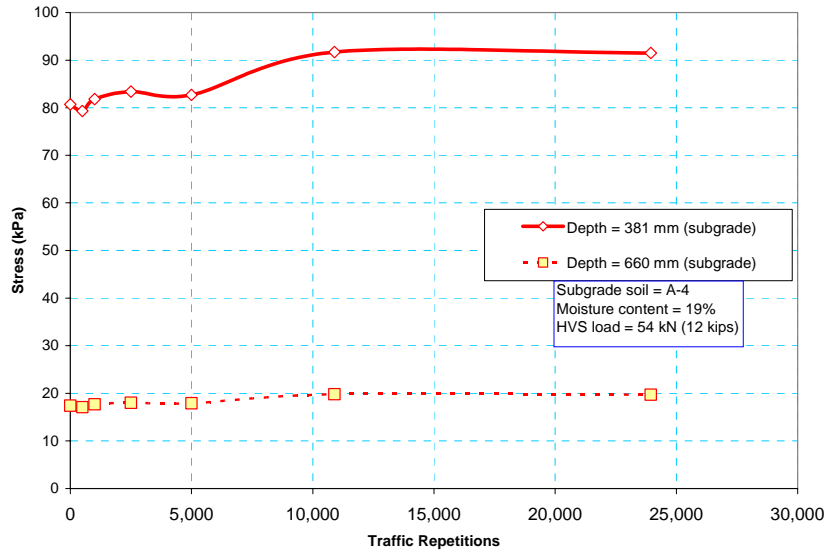
Figure 52b. Stress with subgrade A-4 at 19% moisture and 54 kN HVS load.
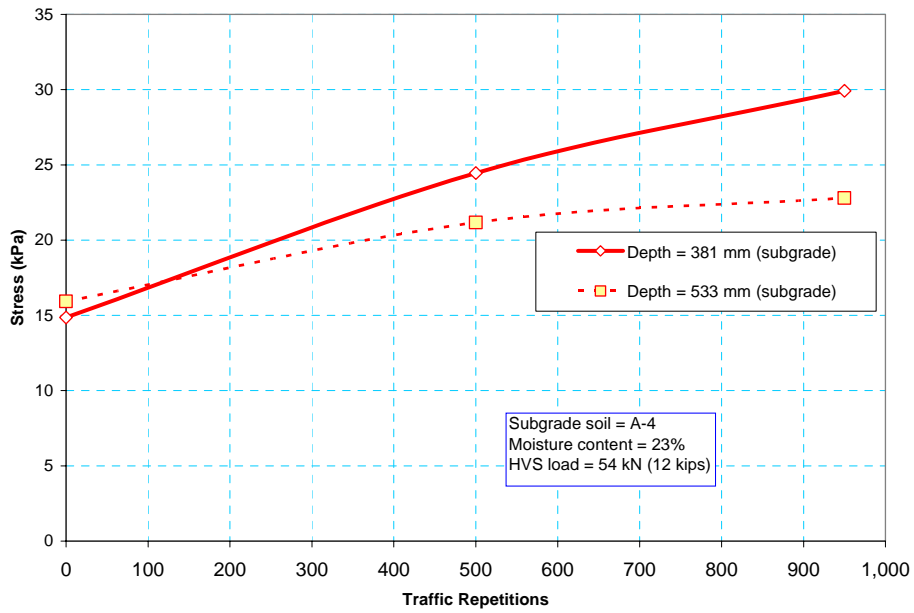
Figure 52c. Stress with subgrade A-4 at 23% moisture and HVS load of 54 kN.
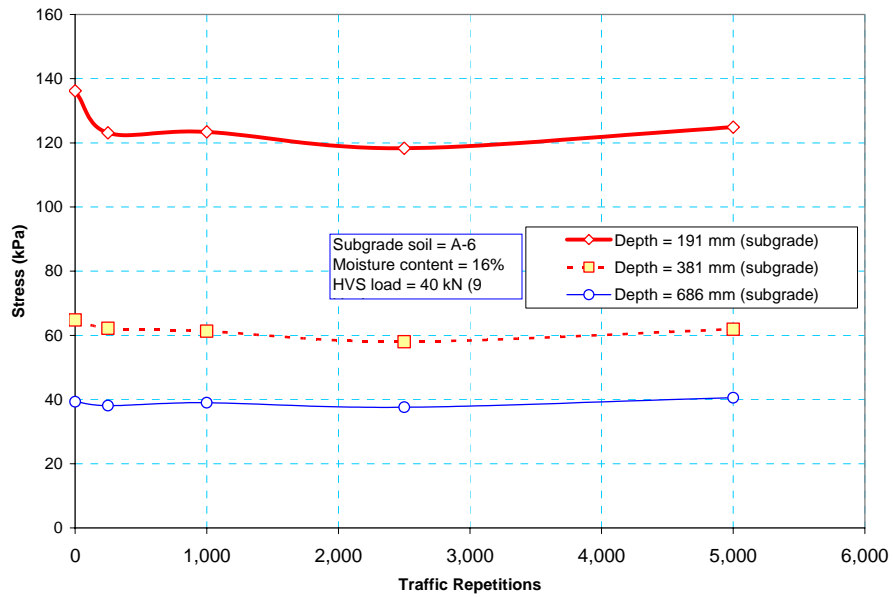
Figure 53a. Stress with subgrade A-6 at 16 %moisture and HVS load of 40 kN.
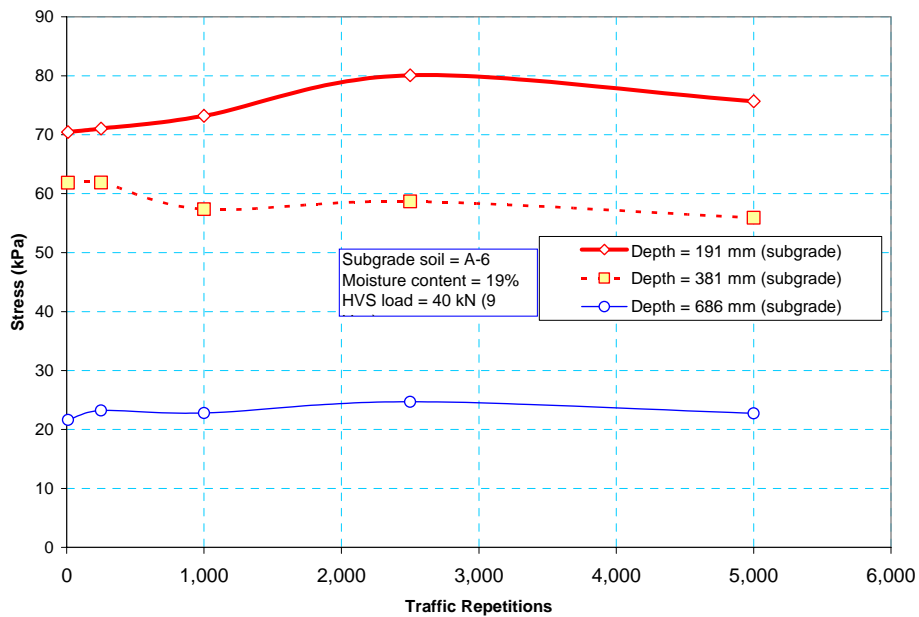
Figure 53b. Stress with subgrade A-6 at 19% moisture and HVS load of 40 kN.
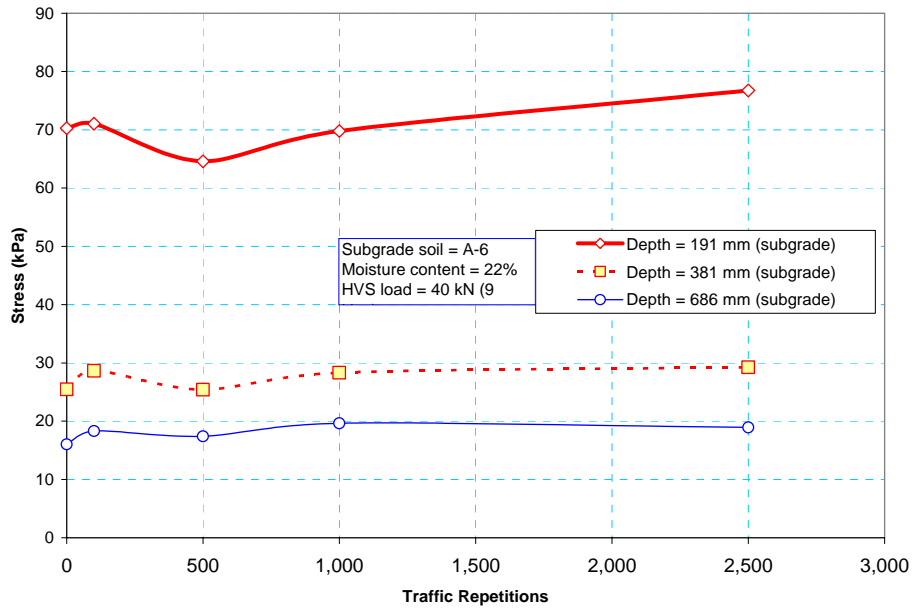
Figure 53c. Stress with subgrade A-6 at 22% moisture and HVS load of 40 kN.
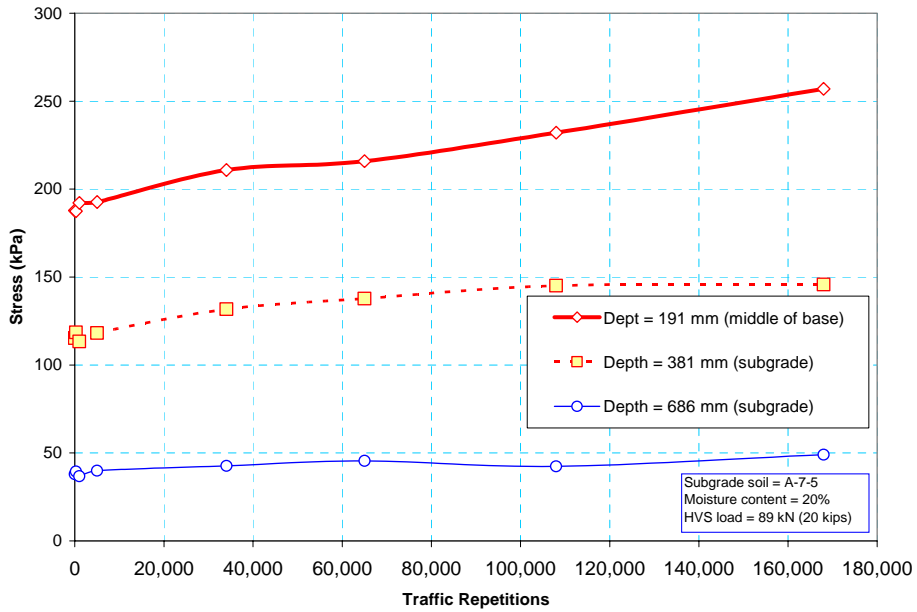
Figure 54a. Stress with subgrade A-7-5 at 20% moisture and HVS load of 89 kN.
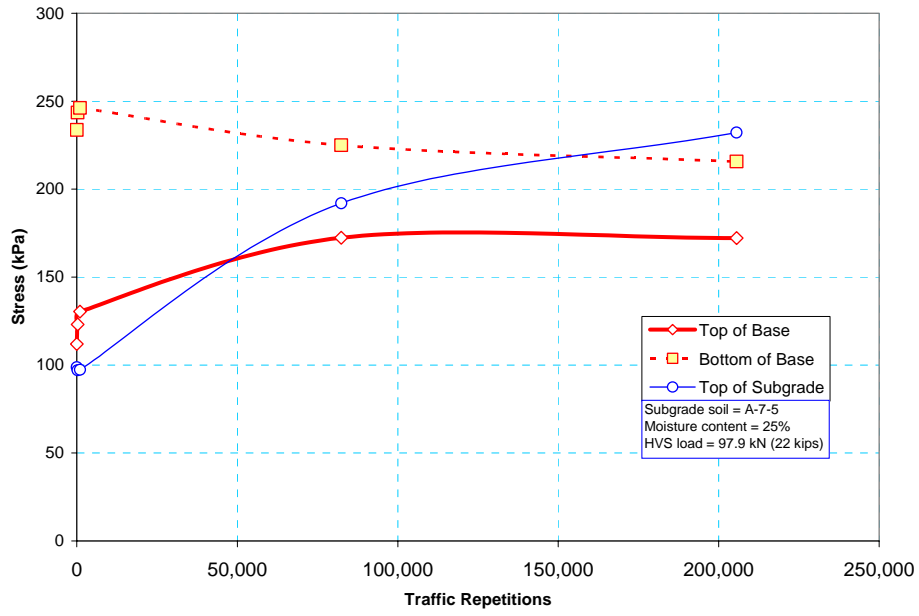
Figure 54b. Stress with subgrade A-7-5 at 25% moisture and HVS load of 97.9 kN.

CHAPTER 6

DATA ANALYSIS AND MODELING

6.1 Failure Criteria

The Asphalt Institute and the Shell failure criteria based on limiting the resilient strain at the top of the subgrade in flexible pavements were examined in view of the test results obtained from the test sections in this study. Figure 55 presents the test results plotted together with the above mentioned criteria. The data obtained with the subgrade soil type A-2-4 is in reasonable agreement with the established criteria, but significant deviations were observed for the other soil types. The data suggests that failure criteria must be a function of soil type and moisture condition.
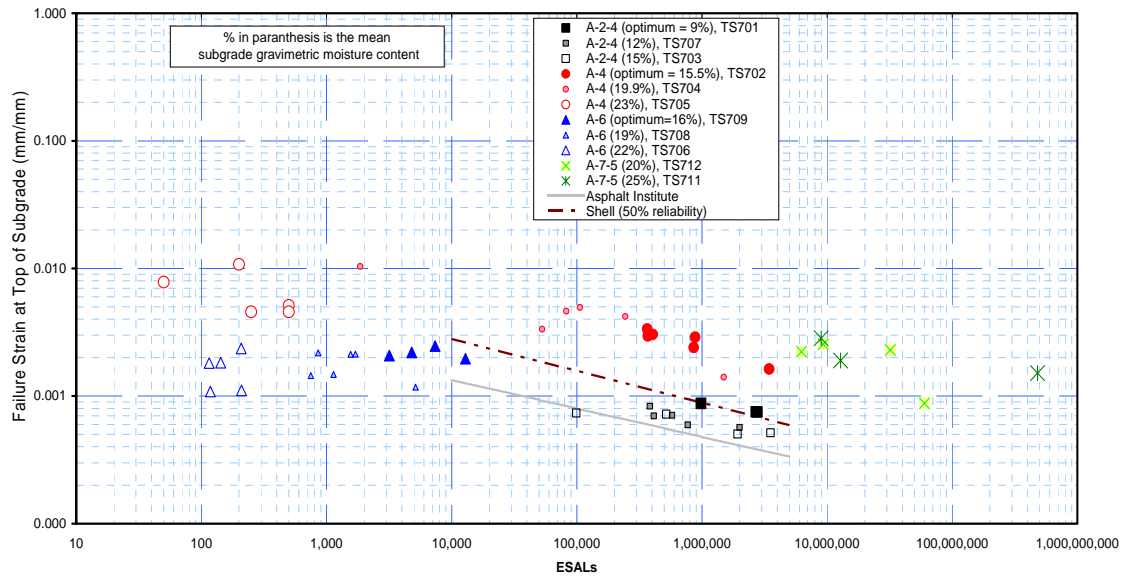
Figure 55. Top of subgrade vertical resilient strain at failure.

6.2 Virtual Sensor Experimental and Analytic Method

Sensor installation requires extreme care to preserve the density and moisture of the subgrade soil so that the soil surrounding the sensors can correctly represent the soil in the rest of the soil layer. In the design of full-scale pavement experiments, it is desired to have many sensors embedded in the test sections. However, excessive sensors may significantly disturb the soil density and moisture, thereby decreasing the reliability of a test results. Under the assumption that stress and strain would be maximized at points under the center of the tire path, sensors were installed only at these locations. A method was devised to create a system of virtual sensors that generated detailed cross sections of stress and strain without the expense of more sensors and the potential disturbance to the soil layers.
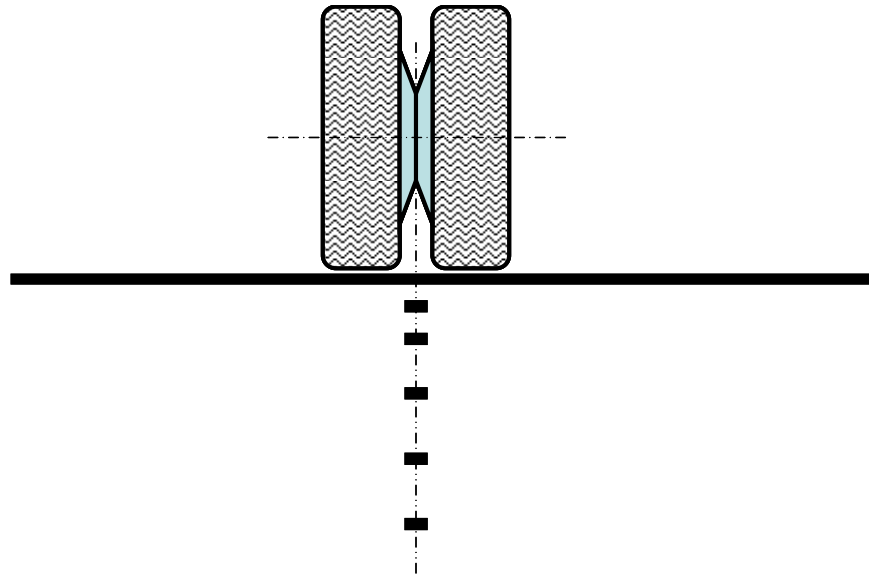
Figure 55a. Real sensors.
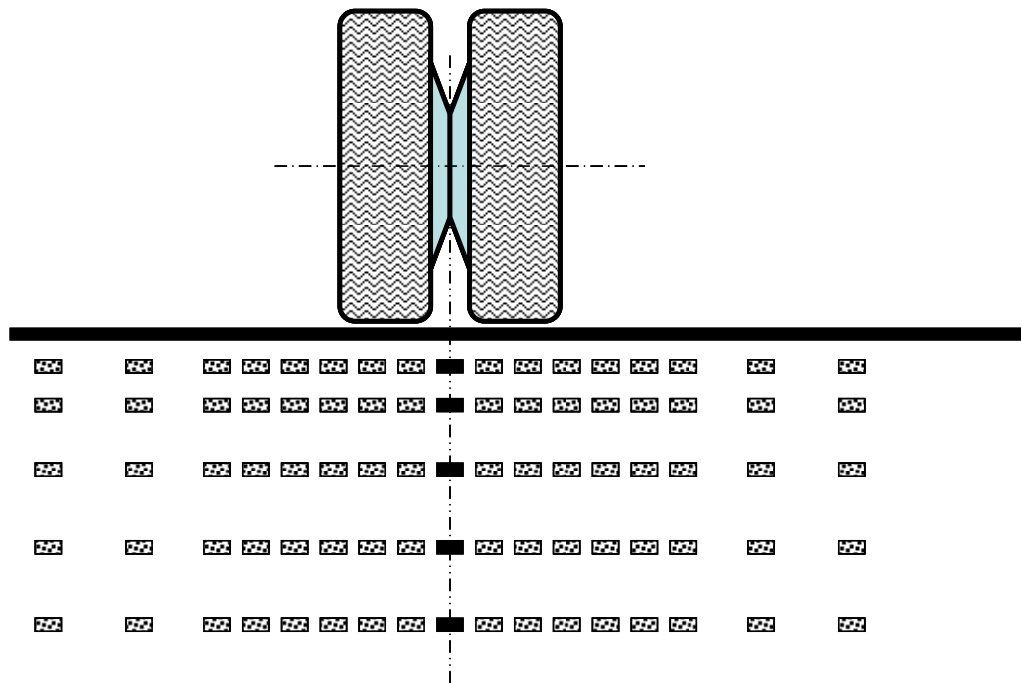
Figure 55b. Real sensors augmented with virtual sensors.

Figures 55 illustrate the real and virtual system of sensors. The number and

location of sensors in these figures is not intended to accurately reflect the numbers of

stress and strain sensors in the actual test sections, but only to illustrate the principle of

virtual sensors. Figure 55a shows a sample of real sensors installed under the center of the tire path. Figure 55b shows the number of sensors augmented by several more sensors located at a series of offset distances from the center line. Instead of installing these sensors, the response of the real sensors were recorded at a series of replicate traffic repetitions conducted with the tire assembly moved to corresponding offset positions relative to the real sensors. The real sensors are shown in solid black color in Figure 55. The virtual sensors were drawn filled with dots. The products of the virtual sensor method are the resilient deformation and stress cross sections shown in subsequent figures.

The virtual sensor method was not included in the original experimental plan. It was originally developed while checking for influence of traffic loads applied to one test window on adjacent test windows. The original experiments were conducted while traffic testing Test Window 708c3. In that test window, the applied load was 31.1 kN (7 kips). Virtual sensor experiments were later conducted in Test Windows 712c5 and 712c6 using offsets and four load levels: 26.7 kN (6 kips), 40 kN (9 kips), 80 kN (18 kips), and 97.9 kN (22 kips). The latter test windows were replicates of each other. They were built with subgrade soil type A-7-5 at optimum gravimetric moisture content of 20%.

6.3 Strain Cross Sections

Figures 56 through 68 show cross sections of vertical, longitudinal and transversal resilient strain produced with four different load intensities. These cross sections were constructed with the virtual sensor method. Figure 56 displays the resilient strain

measurements conducted during the testing of Test Window 708c3 loaded with HVS load of 31.1 kN (7 kips). This test section was built with soil AASHTO type A-6 at 19 percent moisture content (3 percent wet of optimum). Originally, this data was acquired to evaluate the extent of interaction between neighboring test windows, and later it was recognized as a valuable method to obtain detailed strain and stress cross sections. The method now called Virtual Sensor Method was applied in full in test windows 712c5 and 712c6 that corresponded to the subgrade soil type A-7-5 at optimum moisture content.
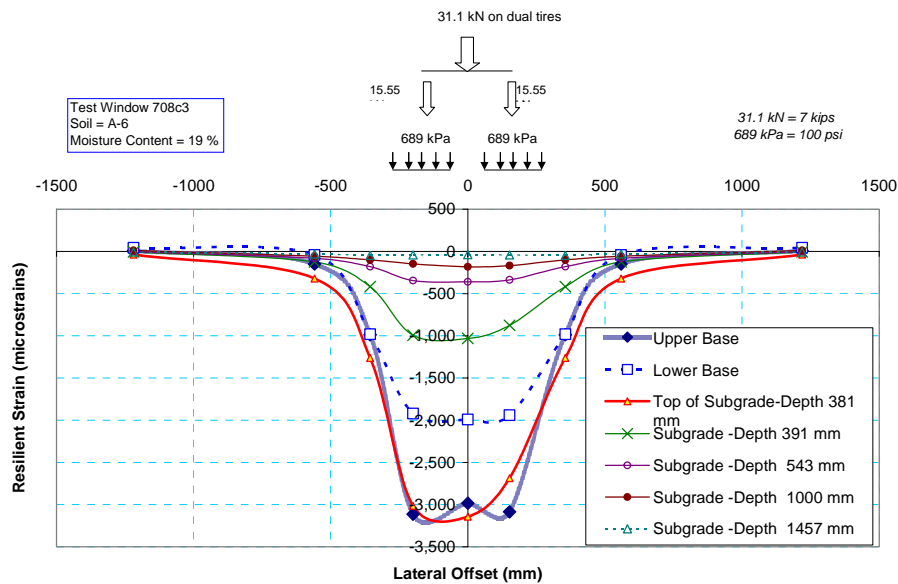
Figure 56. Vertical resilient strain cross section with subgrade soil A-6 at 19% and HVS load of 31.1 kN (7 kips).

Figure 56 shows that, for this case of subgrade soil type and moisture condition, the resilient strains at the top of the subgrade and those at the top of the base course were similar in value. The strains at shallow depths showed the influence of the space in between the two tires. This effect was not seen at deeper depths because of superposition of the loads from the two tires in the dual-tire assembly used in these tests. Notice that the

strain and stress cross sections for the subgrade soil type A-6 at 19 percent gravimetric moisture content are not exactly symmetrical because measurements were made on the complete right side and partly on the left side.

Figures 57 through 68 present the resilient strain test results in Test Section 711 that corresponds to a subgrade soil type A-7-5 at optimum moisture content. Four load intensity levels were included. The lowest level of 26.7 kN (6 kips) corresponds to 66.7 percent of the standard axle load of 80 kN (18 kips) because the HVS load represents one half of a truck axle as illustrated in Figure 25. The next HVS (1/2 axle) load level used in the virtual sensor experiments was 40 kN (9 kips) that corresponds to the full axle standard axle load of 80 kN (18 kips). Most experiments reported in the literature are referenced to this load level. The third load level was exactly twice the standard axle load. The highest load level used in these virtual experiments was 97.8 kN (22 kips) of HVS load corresponding to a full axle load of 195.6 kN (44 kips). Although the HVS is designed to apply (half axle) loads up to 200 kN (45 kips), the load limit in our experiments was determined by the design load of the dual tires.

Figures 57 through 60 present the vertical component of strain, each at one of the four load levels described above. Similarly, Figures 61 through 64 present the longitudinal component of strain, and Figures 65 through 68 present the strain measurements in the direction transversal to the tire path.
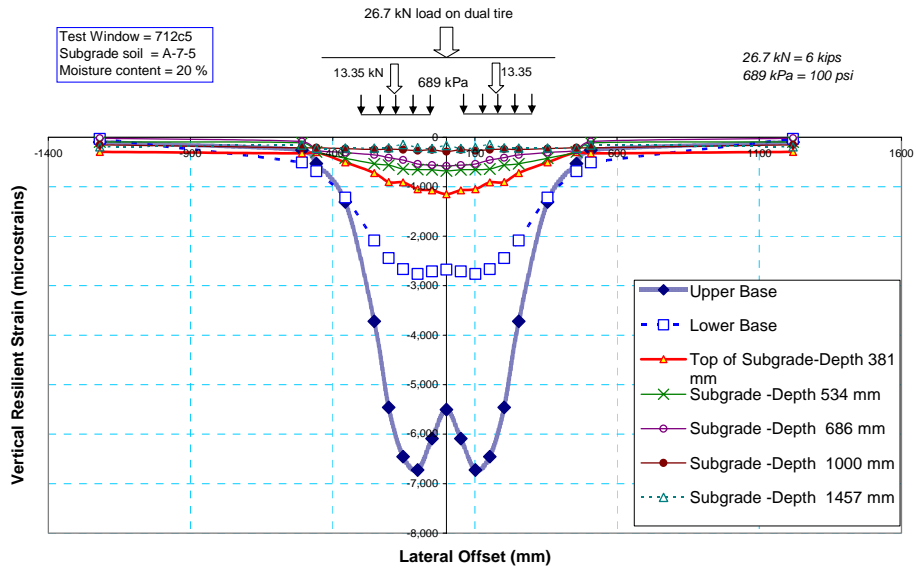
**Figure 57. Vertical resilient strain cross section with subgrade soil A-7-5 at 20%
and HVS load of 26.7 kN (6 kips).**
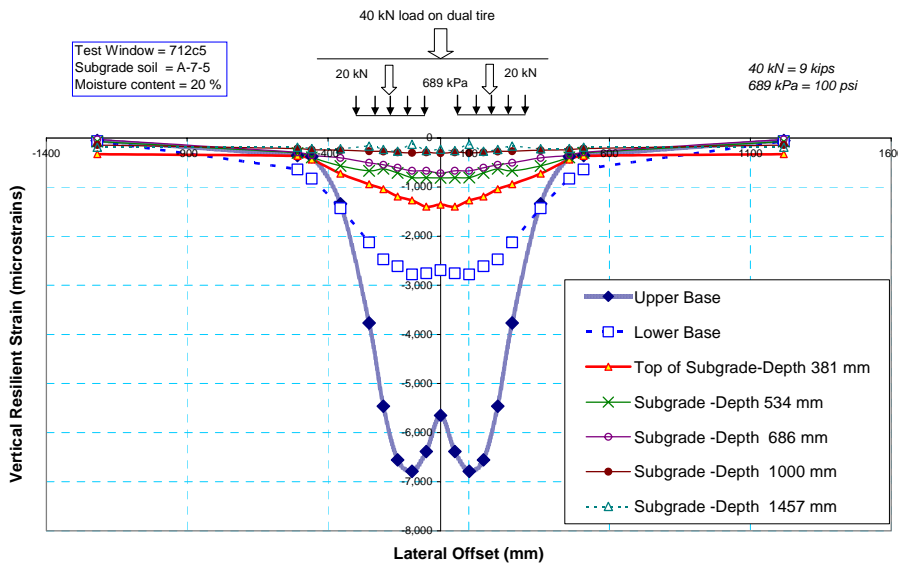
**Figure 58. Vertical resilient strain cross section with subgrade soil A-
7-5 at 20% and HVS load of 40 kN (9 kips).**
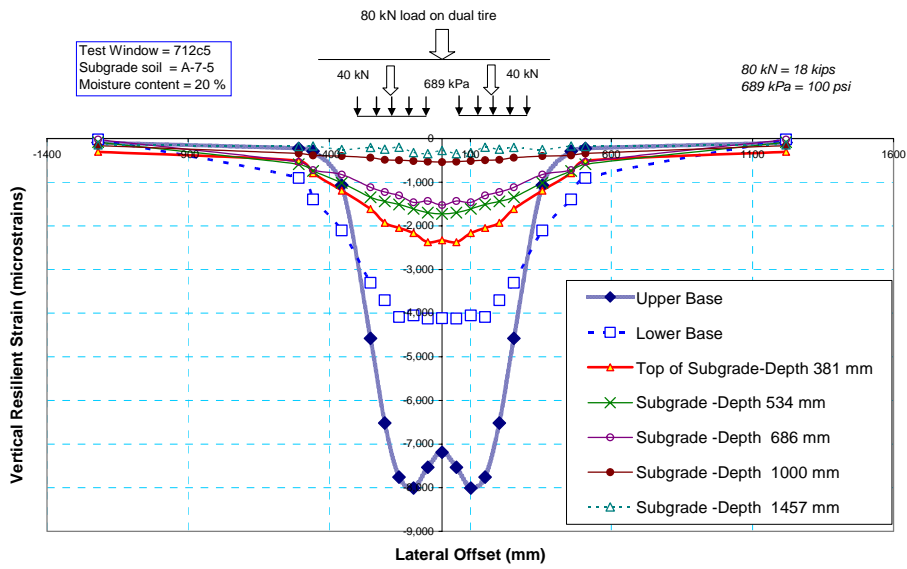
Figure 59. Vertical resilient strain cross section with subgrade soil A-7-5 at 20% and HVS load of 80 kN (18 kips).
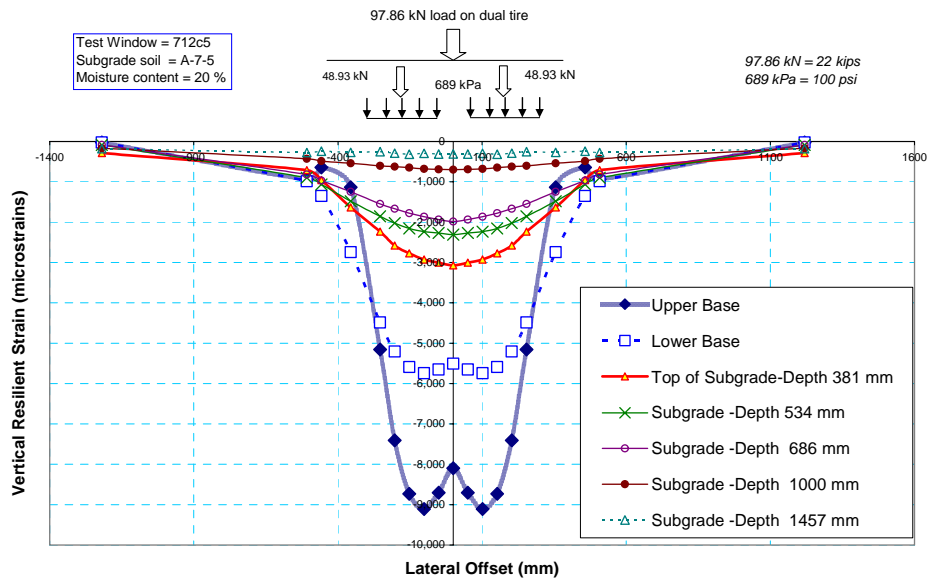
Figure 60. Vertical resilient strain cross section with subgrade soil A-7-5 at 20% and HVS load of 97.9 kN (22 kips).

In the strain and stress cross section figures, the loads applied by a set of dual tires are shown approximately scaled in width to the lateral offset distances of the sensors. The tire inflation pressure was kept constant at 689 kPa (100 psi) throughout these experiments.

Strains were largest in the upper half of the base course followed by the lower half of the base course and, much smaller in the subgrade. As expected, strains continue to decrease with depth. The depths indicated in the figures are relative to the upper surface of the asphalt concrete. At the standard axle load level, the strains at a depth of 1.0 m (39.4 in.) could not be discerned from the normal electronic noise in the sensor output. At the heaviest load level, the strains measurements at a depth of 1.0 m (39.4 in.) could be reliably measured, but the strain at a depth of 1.5 m (59 in.) was read with difficulty from within the normal electronic noise band.

It should be noted that all the strain and stress cross sections in Figures 57 through 68 show perfect symmetry because the measurements were conducted on one side only at offset distances of 0, 51, 102, 152, 203, 254, 356, 457, 508 and 1219 mm (0, 2, 4, 6, 8, 10, 14, 18, 20 and 48 in.). Should the measurements were conducted on both sides, some asymmetry would occur in the measured values due to normal random variability.
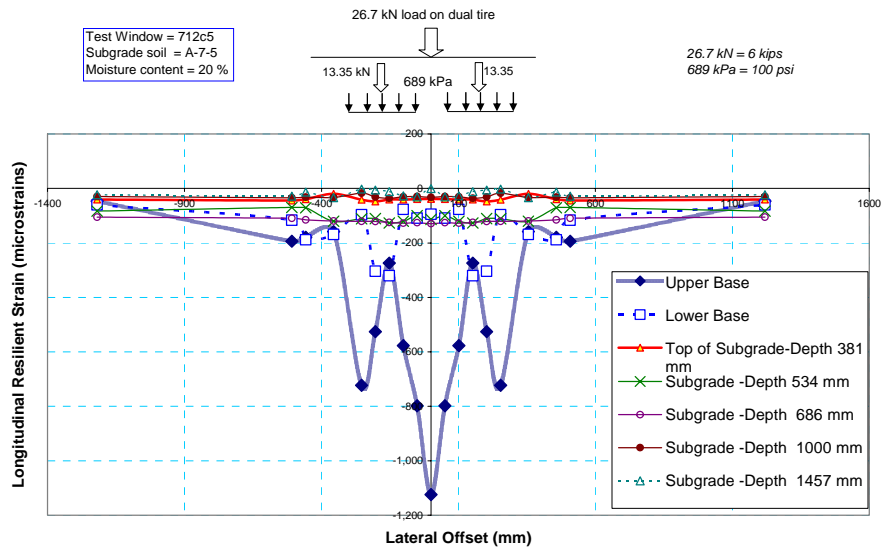
Figure 61. Longitudinal resilient strain cross section with subgrade soil A-7-5 at 20% and HVS load of 26.7 kN (6 kips).
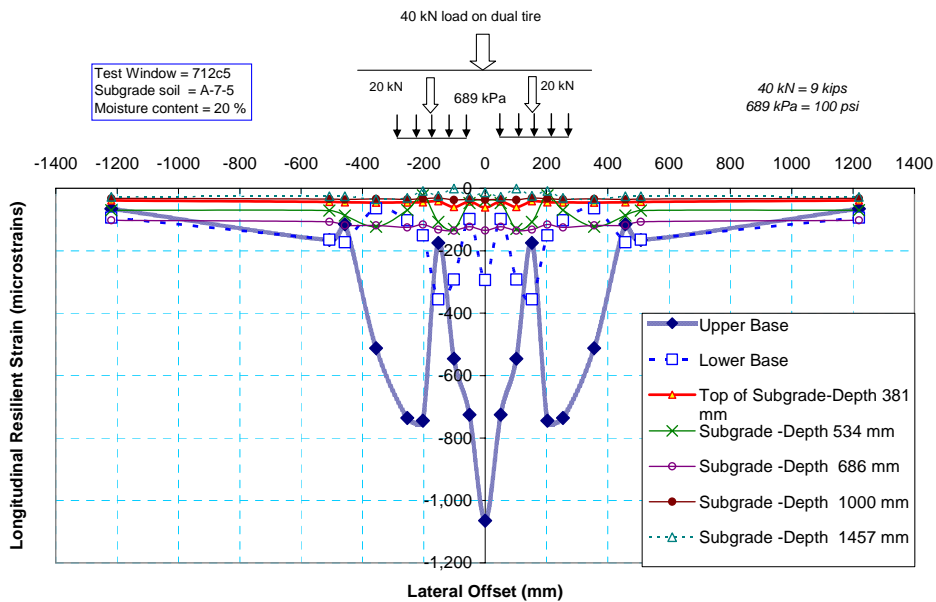
Figure 62. Longitudinal resilient strain cross section with subgrade soil A-7-5 at 20% and HVS load of 40 kN (9 kips).
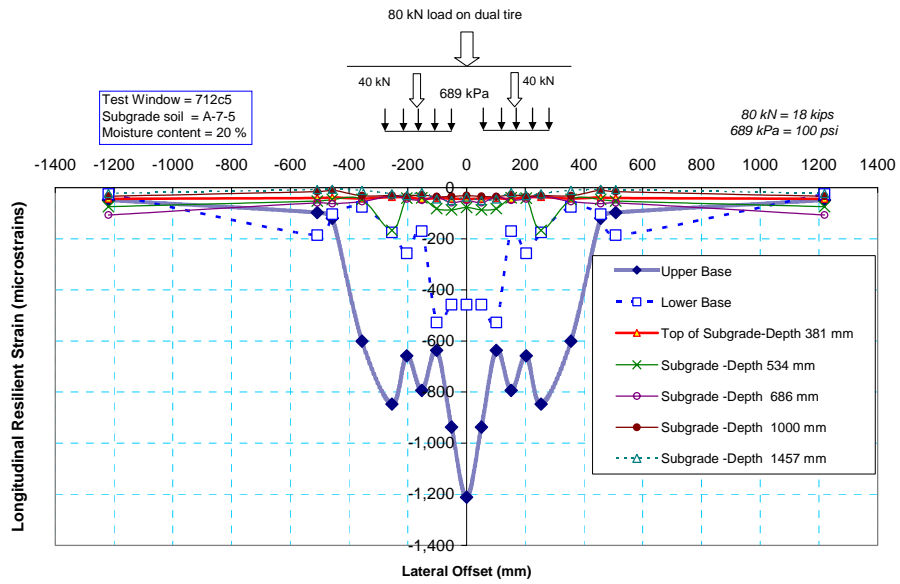
Figure 63. Longitudinal resilient strain cross section with subgrade soil A-7-5 at 20% and HVS load of 80 kN (18 kips).
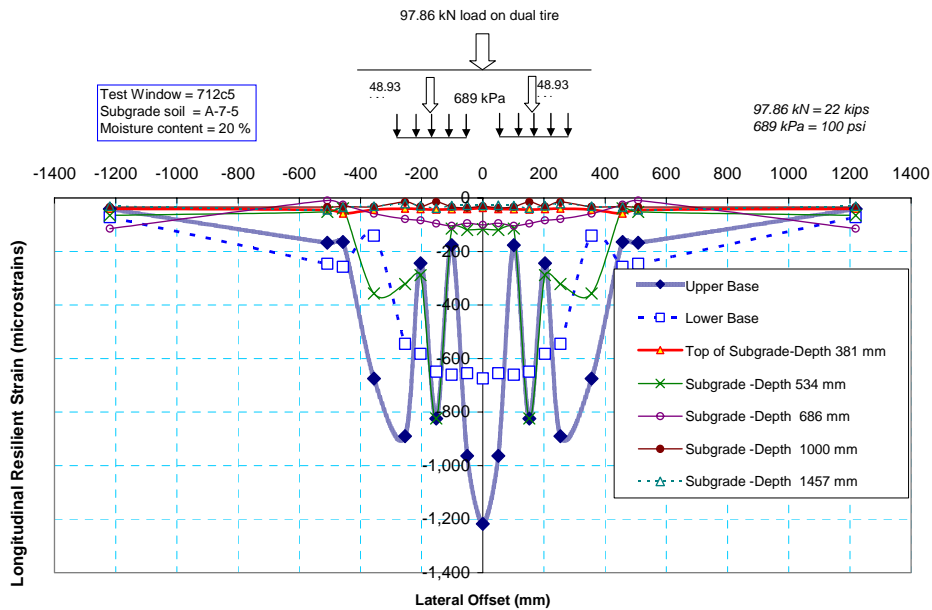
Figure 64. Longitudinal resilient strain cross section with subgrade soil A-7-5 at 20% and HVS load of 97.9 kN (22 kips).

Longitudinal strain measurements shown in Figures 61 through 64 display pronounced changes in strain values across lateral offsets. This may be due to restraint imposed by the vertical tire loads. The magnitudes of the longitudinal strains were approximately 15 percent of those in the vertical direction. Except for the heaviest load level, the strains in the subgrade were very small compared to those in the base course.

Figures 65 through 68 indicate that the transversal strains were relatively large in the upper half of the base course, and rapidly decreased with depth. At the standard axle load, the transversal strain in the upper region of the base course was 35 percent of the vertical strain at the same depth. The measured transversal strain values in the subgrade were very small and hardly readable at the standard axle load level and below. The transversal strains in the subgrade were distinguishable, but still small for the heavier load levels.

Comparing the vertical, longitudinal and transversal resilient strains at the top of the subgrade for the standard axle load level, it was found that the longitudinal and transversal strains were approximately 12 and 4 percent of the vertical strain respectively.
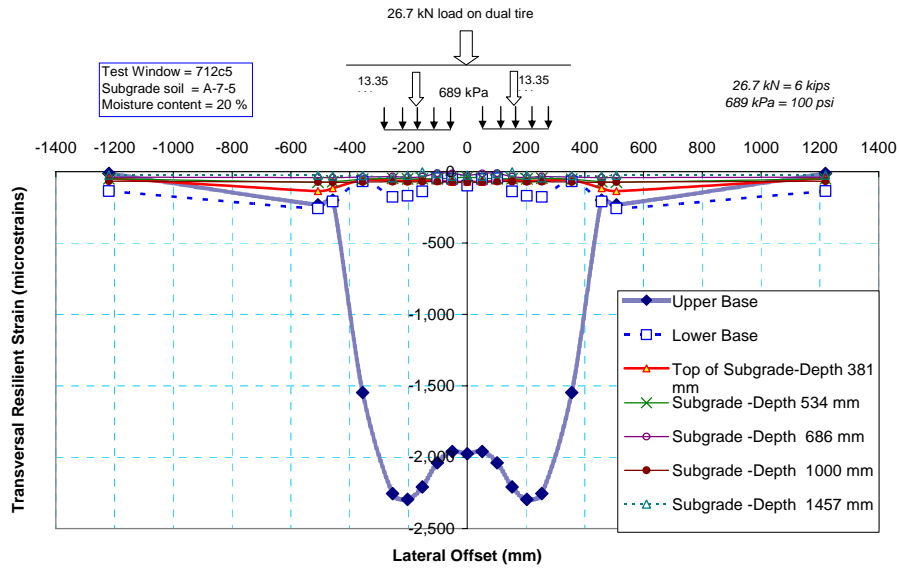
**Figure 65. Transversal resilient strain cross section with subgrade soil A-7-5 at 20% and HVS load of 26.7 kN (6 kips).**
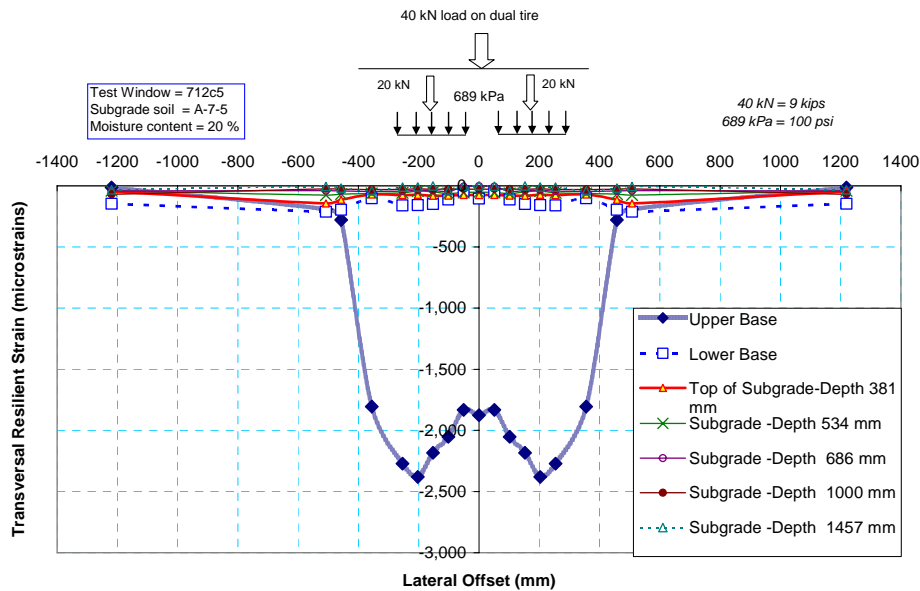

Figure 66. Transversal resilient strain cross section with subgrade soil A-7-5 at 20% and HVS load of 40 kN (9 kips).
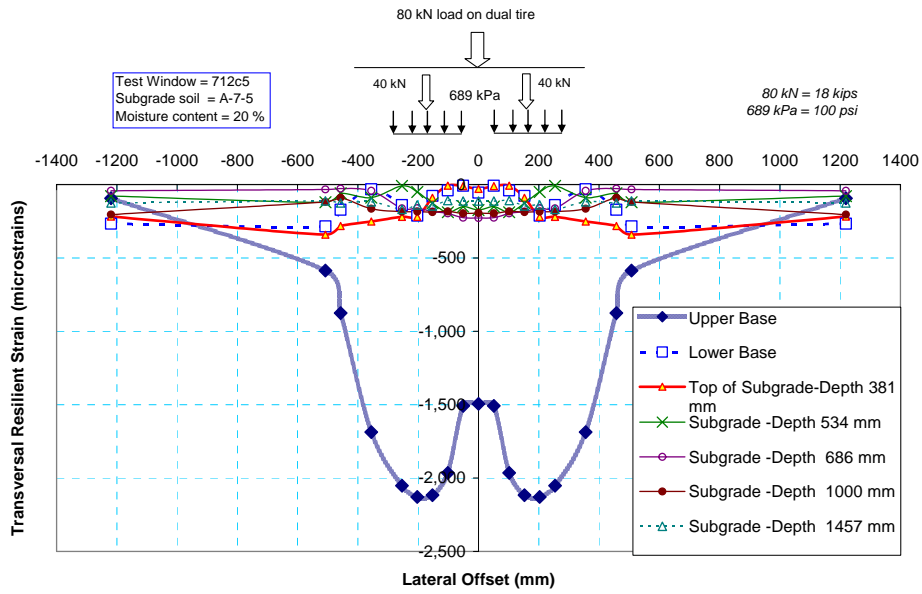
Figure 67. Transversal resilient strain cross section with subgrade soil A-7-5 at 20% and HVS load of 80 kN (18 kips).
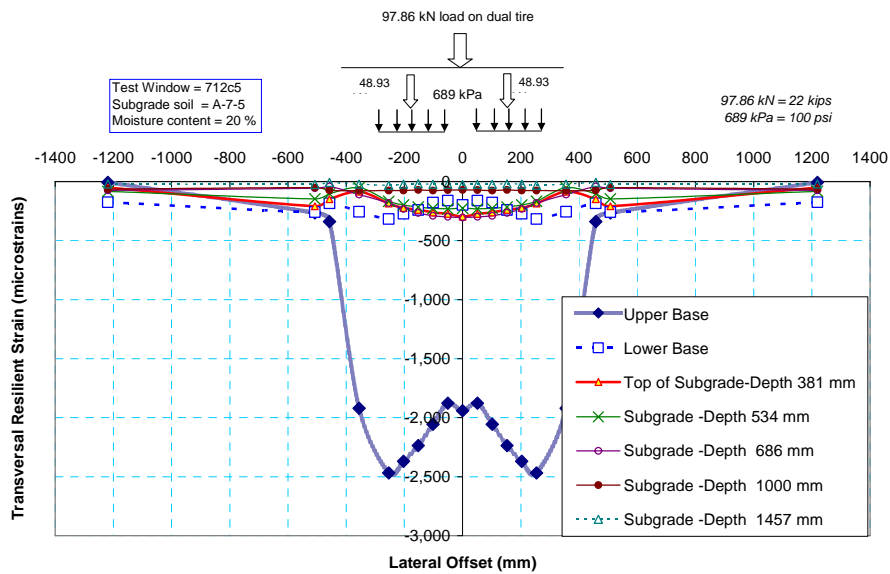

Figure 68. Transversal resilient strain cross section with subgrade soil A-7-5 at 20% and HVS load of 97.9 kN (22 kips).

6.4 Stress Cross Sections

Stress measurements were conducted simultaneously with the strain measurements in the virtual sensor experiments described above. However, fewer stress sensors were included in the test sections compared to the number of strain sensors. Therefore, the measurements of Test Windows 712c5 and 712c6 were combined to increase the number sensor locations jointly representing Test Section 712. This test section was built with a subgrade soil type A-7-5 at optimum moisture content. The following stress profiles include measurements taken with both Geokon and Dynatest stress cells.
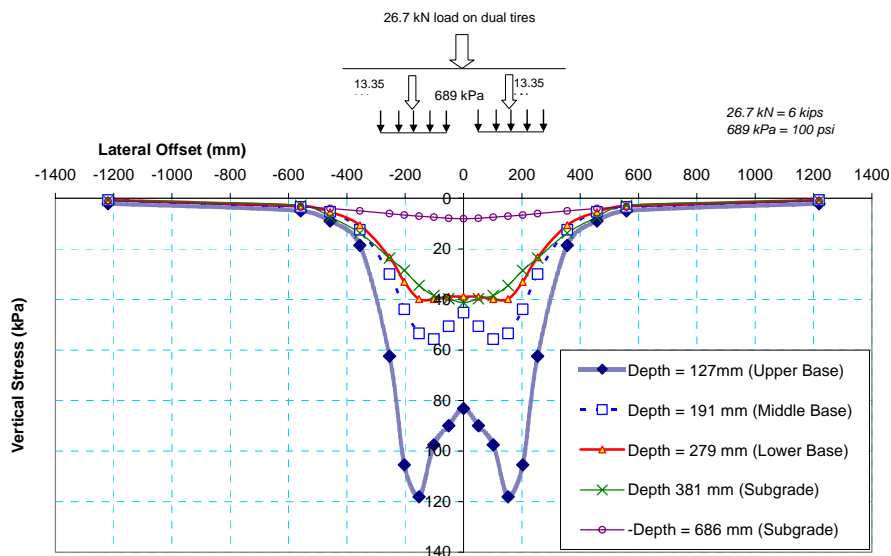
Figure 69. Vertical stress in test section with subgrade A-7-5 at 20% moisture content and HVS load of 26.7 kN (6 kips).
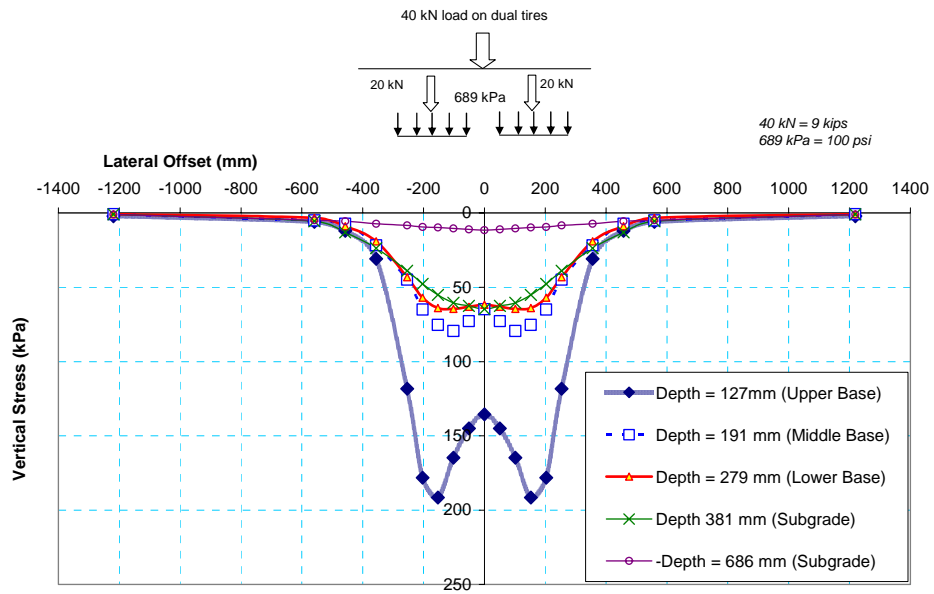
Figure 70. Vertical stress in test section with subgrade A-7-5 at 20% moisture content and HVS load of 40 kN (9 kips).
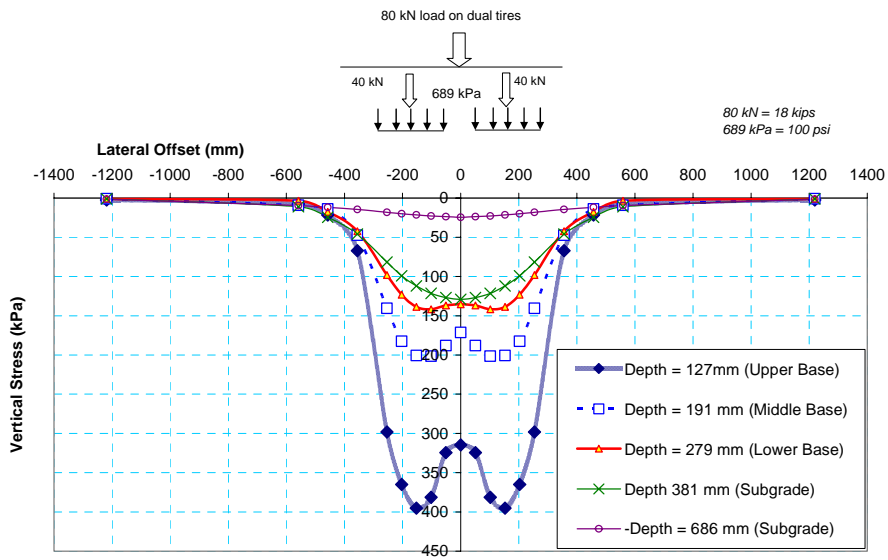
Figure 71. Vertical stress in test section with subgrade A-7-5 at 20% moisture content and HVS load of 80 kN (18 kips).
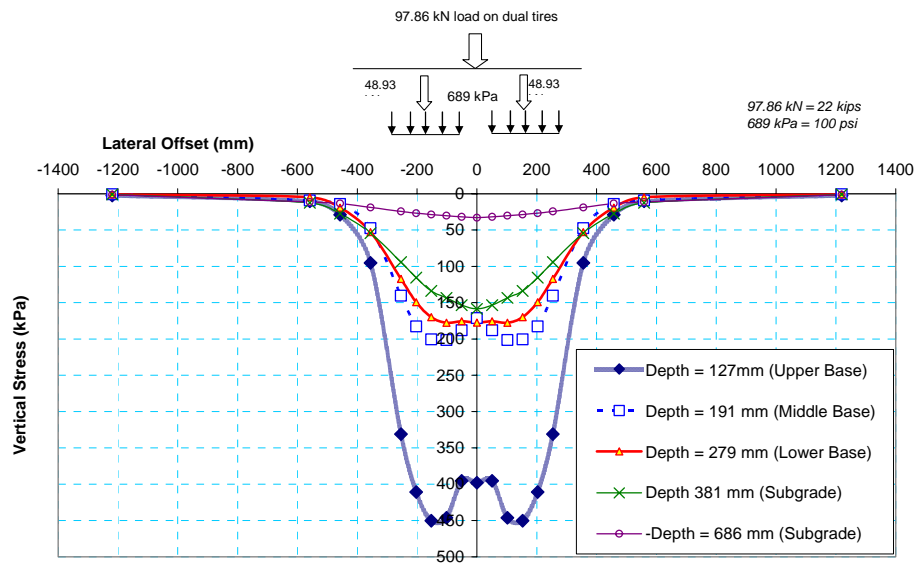
Figure 72. Vertical stress in test section with subgrade A-7-5 at 20% moisture content and HVS load of 97.9 kN (22 kips).

As expected, vertical stress decreased with depth. At shallow depths the stress curves displayed lower stress at the center aligned with the space between the two tires. The absence of this feature at deeper locations indicates overlapping of the stresses emanated from the two tires.

The stress at the top of the subgrade increased almost linearly in proportion to the increase in tire loads.

Stress decreased rapidly as the offset distance increased. By an offset distance of 0.5 m (20 in.), the magnitudes of the stresses at all depths were already insignificant. This confirms that the pavement effectively behaved as a flexible pavement.
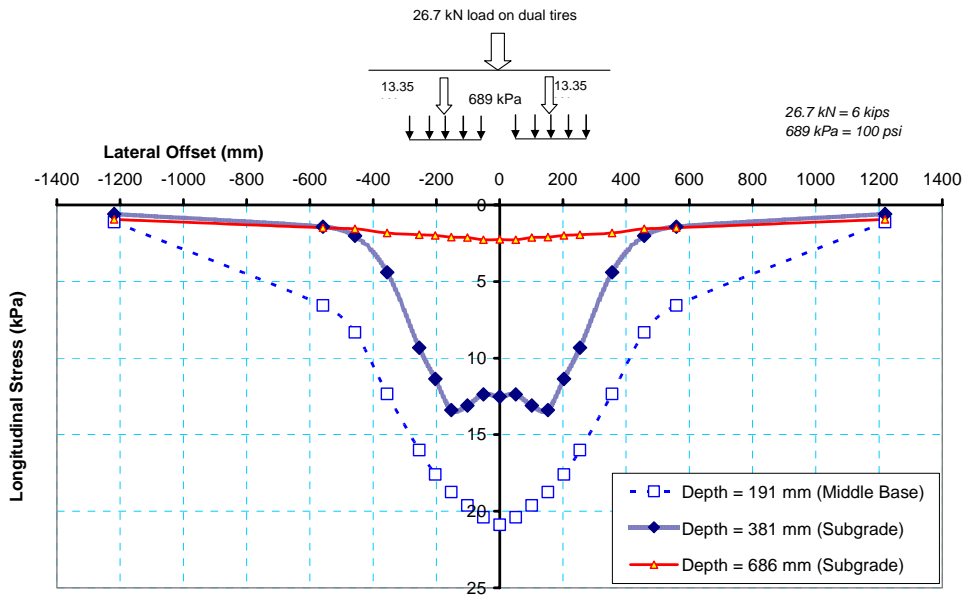
Fi

gure 73. Longitudinal stress in test section with subgrade A-7-5 at 20%

moisture content and HVS load of 26.7 kN (6 kips).
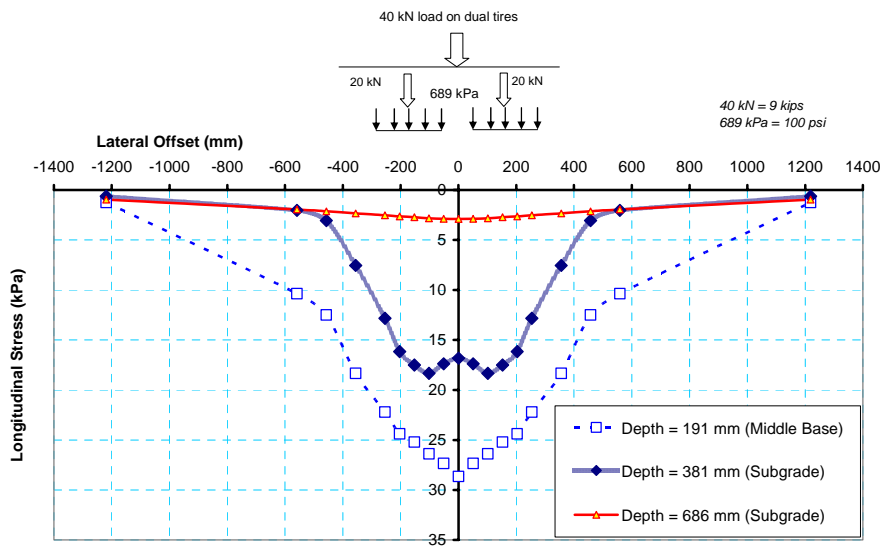
Figure 74. Longitudinal stress in test section with subgrade A-7-5 at 20% moisture content and HVS load of 40 kN (9 kips).
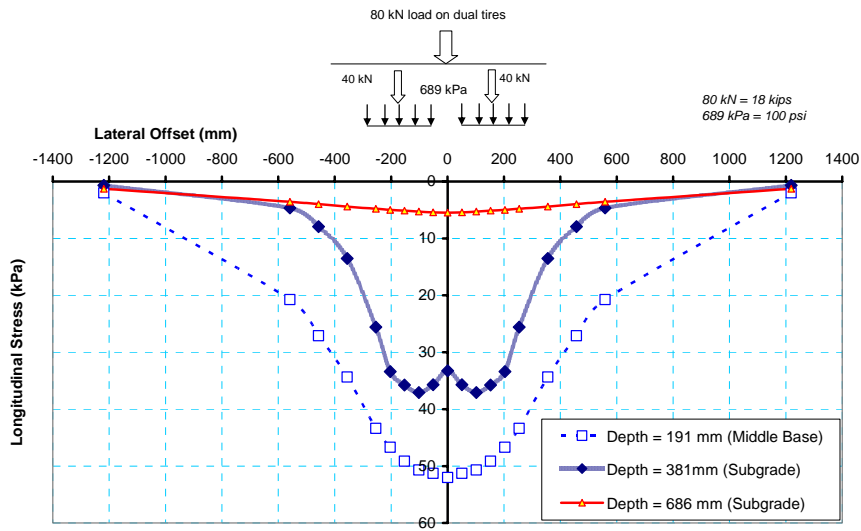
Figure 75. Longitudinal stress in test section with subgrade A-7-5 at 20%

moisture content and HVS load of 80 kN (18 kips).
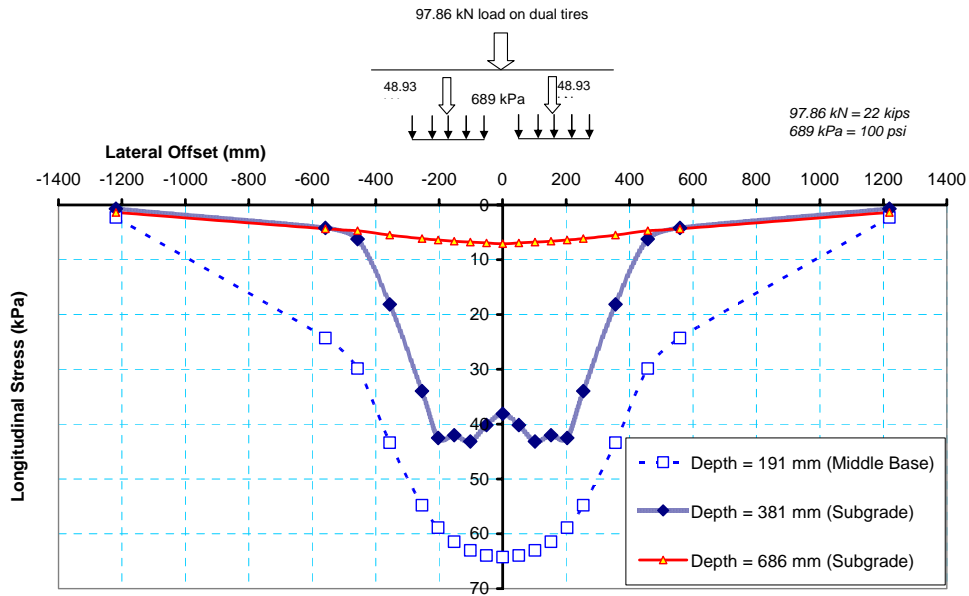
Figure 76. Longitudinal stress in test section with subgrade A-7-5 at 20% moisture
content and HVS load of 97.9 kN (22 kips).

Figures 73 through 76 show the longitudinal component of stress. The data suggests that for this pavement structure made with a relatively strong subgrade, the longitudinal stresses in the base course were higher than the longitudinal stresses in the subgrade. This is consistent with existing theories such as that contained in Boussinesq's equations (Ahlvin, R.G. and Ulery, H.H., 1962) for a homogeneous half space.

The data suggests that for the range of loads covered in these experiments, the relationship between load and stress at a given point is approximately linear. This may not be the case with extremely small and extremely large loads beyond the domain of these experiments.

The stiffness of the soil that supports a stress cell may also affect its ability to register the correct stress value. Also the cell diameter compared to the soil particle size may be a factor. The cell diameter must be sufficiently large to sample a sufficiently large area to be representative without stress concentrations. In the case of our pavement structure, the base course was made of crushed stone with relatively large particles up to 38 mm (1.5 in.) in size. The subgrade was made of a cohesive fine grained soil that was well compacted at optimum moisture content.
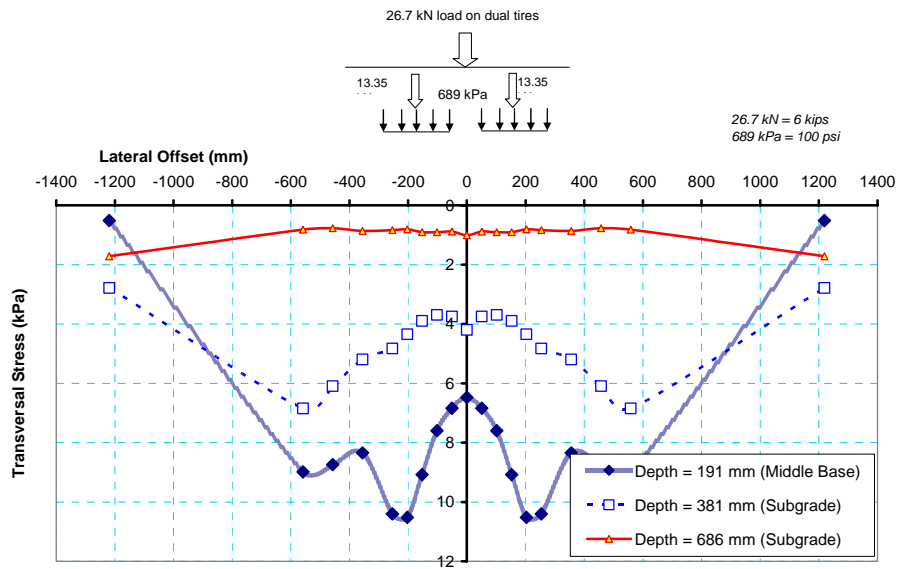
Figure 77. Transversal stress in test section with subgrade A-7-5 at 20% moisture content and HVS load of 26.7 kN (6 kips).
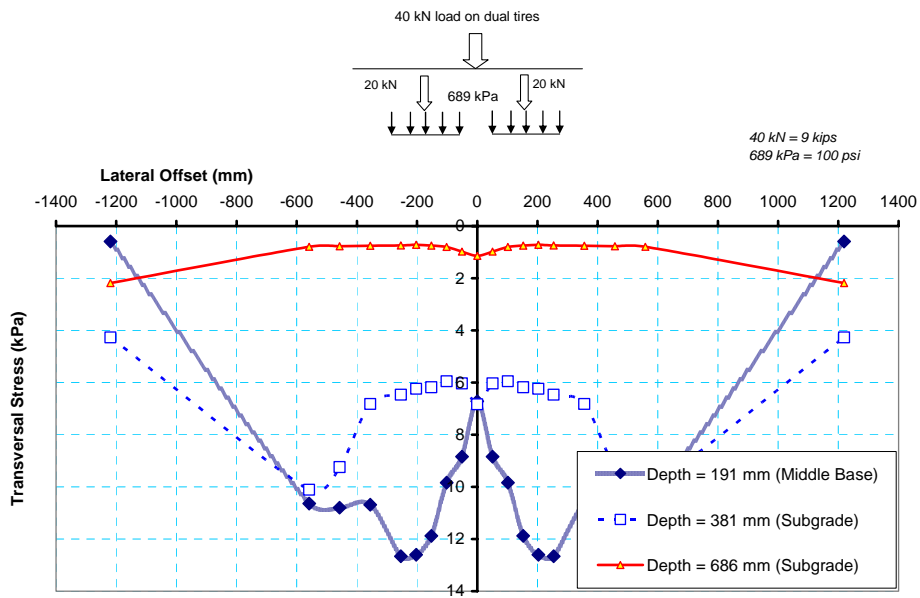
Figure 78. Transversal stress in test section with subgrade A-7-5 at 20% moisture content and HVS load of 40 kN (9 kips).
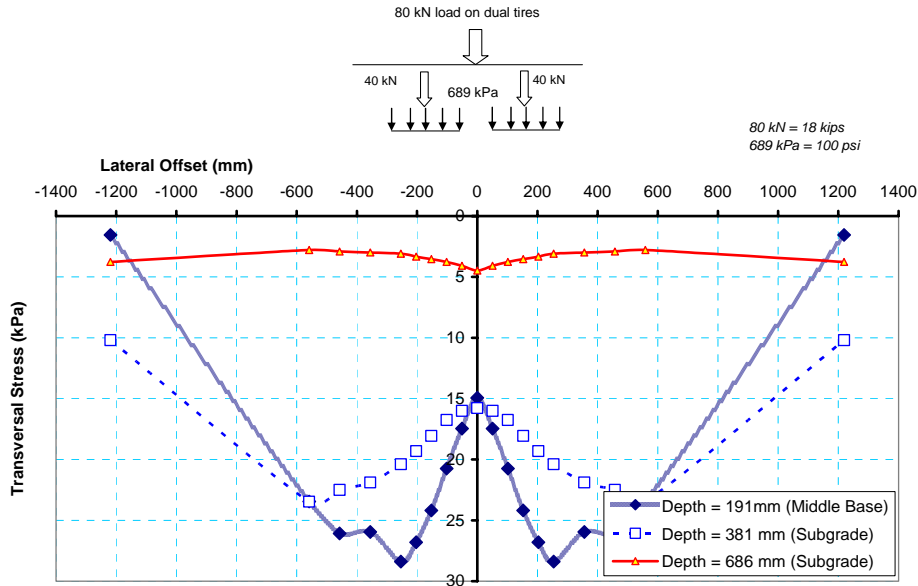
Figure 79. Transversal stress in test section with subgrade A-7-5 at 20% moisture content and HVS load of 80 kN (18 kips).
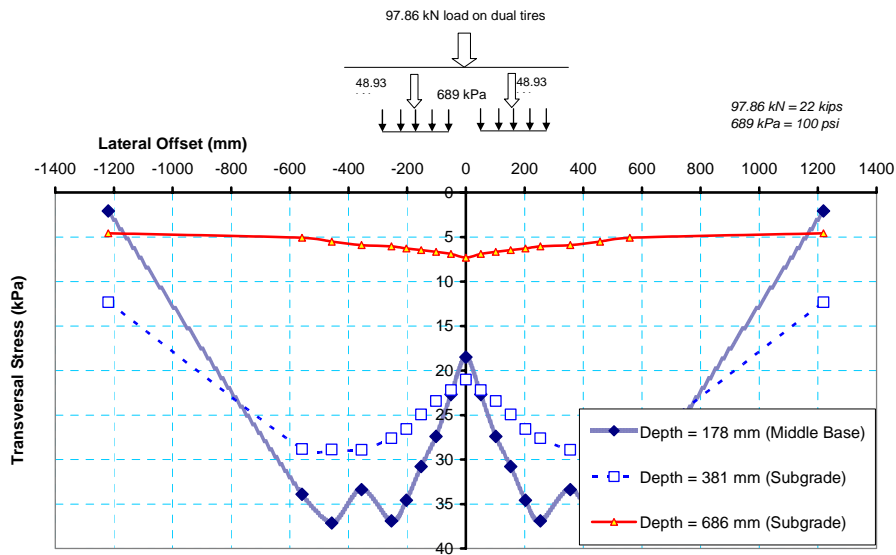

Figure 80. Transversal stress in test section with subgrade A-7-5 at 20% moisture content and HVS load of 97.9 kN (22 kips).

Figures 77 through 80 present the lateral stress measurements at this test section. The lateral stress reached a wider area in the pavement cross section

than did the vertical and the longitudinal stresses. At the standard axle load

level, the magnitude of the maximum lateral stress near the top of the subgrade

was approximately 17 percent of the vertical stress at the same depth.

The stresses measured at the depth of 686 mm (27 in.) relative to the top

of the asphalt were almost insignificant. This is consistent with the small strains

recorded at that depth.

6.5 Resilient Strain Contour Sections

Another useful way of visualizing the resilient strain data is through contour maps

of the cross sections. The following figures show the contour cross sections for strains in

the vertical, longitudinal and transversal directions for four traffic load intensities.. These

contours are equivalent to the cross sections presented in figures 57 through 68. The

strains are expressed in microstrains.

The contour vertical strain figures suggest that the resilient strains in the base

course were much higher than those in the subgrade. The data also shows that the strains

caused by the dual tire traffic were contained in a relatively narrow band. This suggests

that the pavement structure was effectively behaving as a flexible pavement.

The contours contain the same data used in the resilient strain cross sections

shown above. The Surfer® software was used to build the contours automatically. The

reader is cautioned to keep this in mind when interpreting some of the curves.
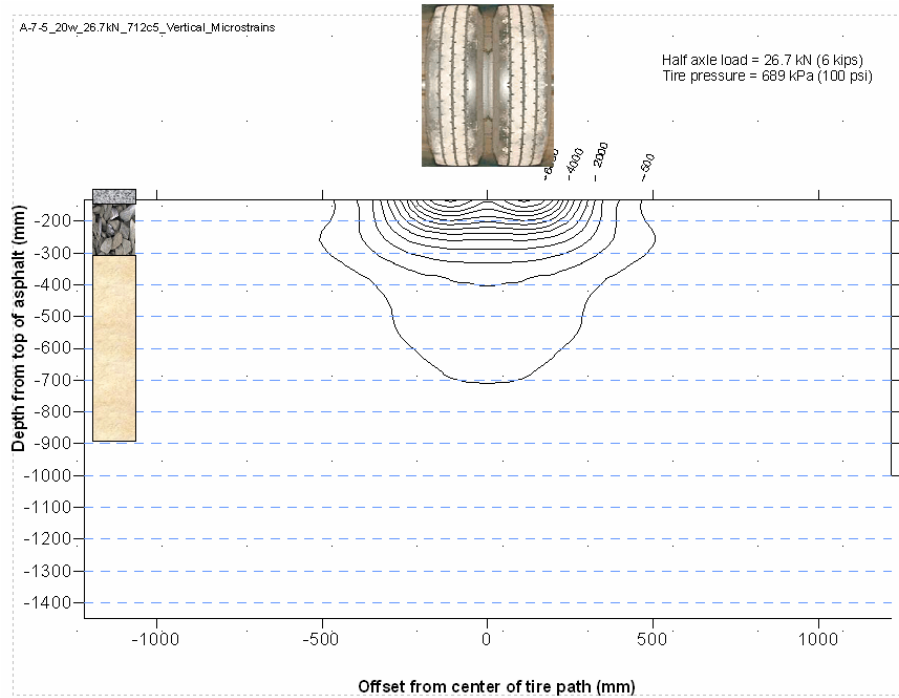
Figure 81. Vertical resilient strain contour section with subgrade soil A-7-5 at 20% and HVS load of 26.7 kN (6 kips).
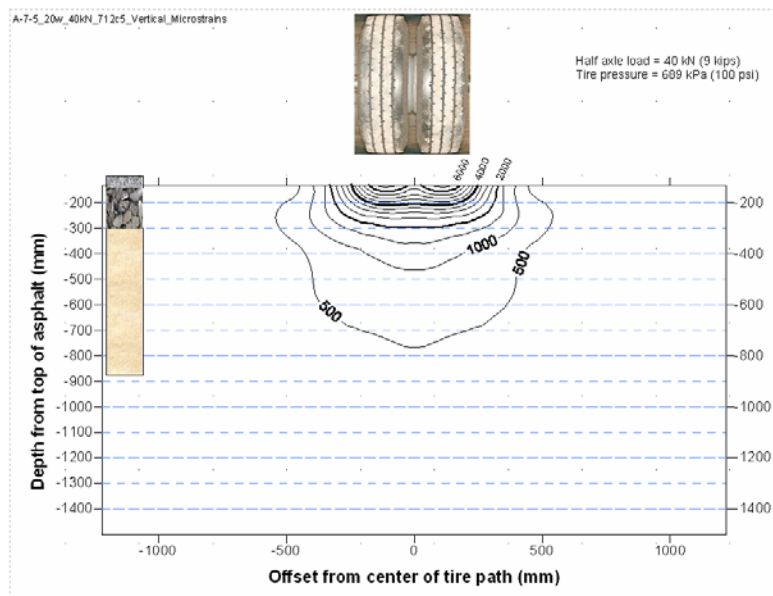
Figure 82. Vertical resilient strain contour section with subgrade soil A-7-5 at 20% and HVS load of 40 kN (9 kips).
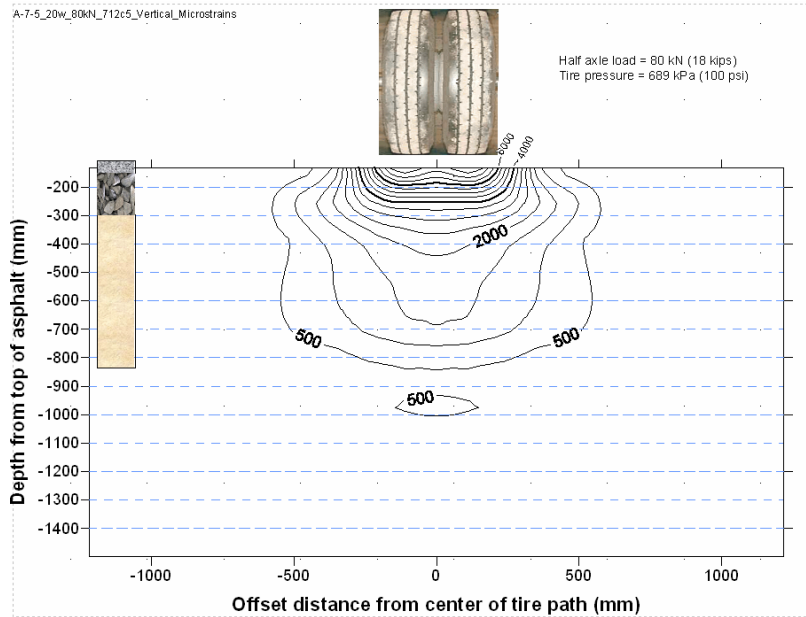
Figure 83. Vertical resilient strain contour section with subgrade soil A-7-5 at 20% and HVS load of 80 kN (18 kips).
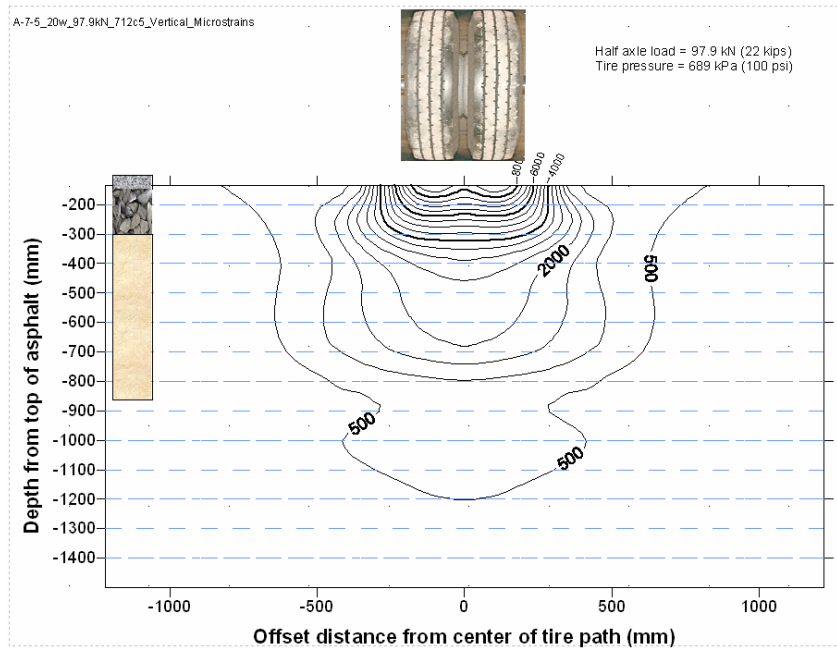
Figure 84. Vertical resilient strain contour section with subgrade soil A-7-5 at 20% and HVS load of 97.9 kN (22 kips).
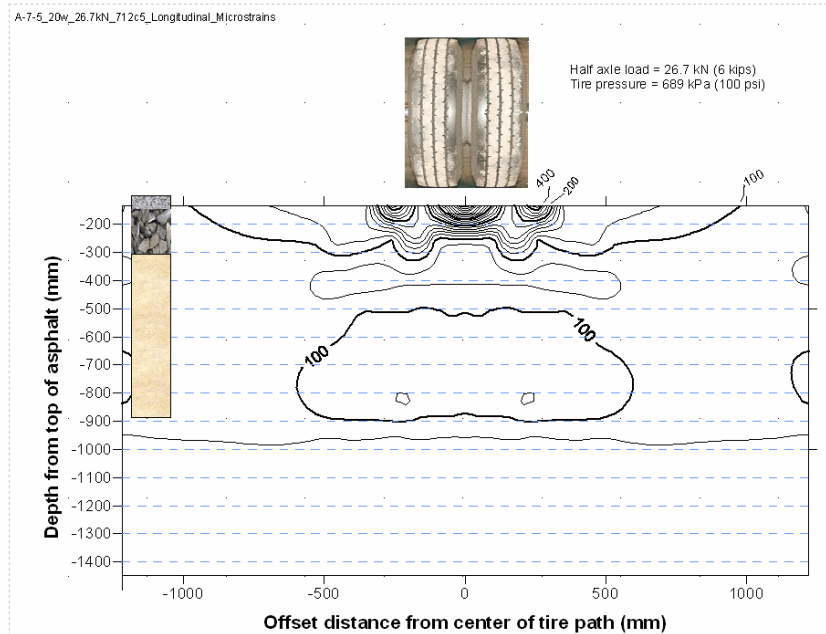
Figure 85. Longitudinal resilient strain contour section with subgrade soil A-7-5 at 20% and HVS load of 26.7 kN (6 kips).
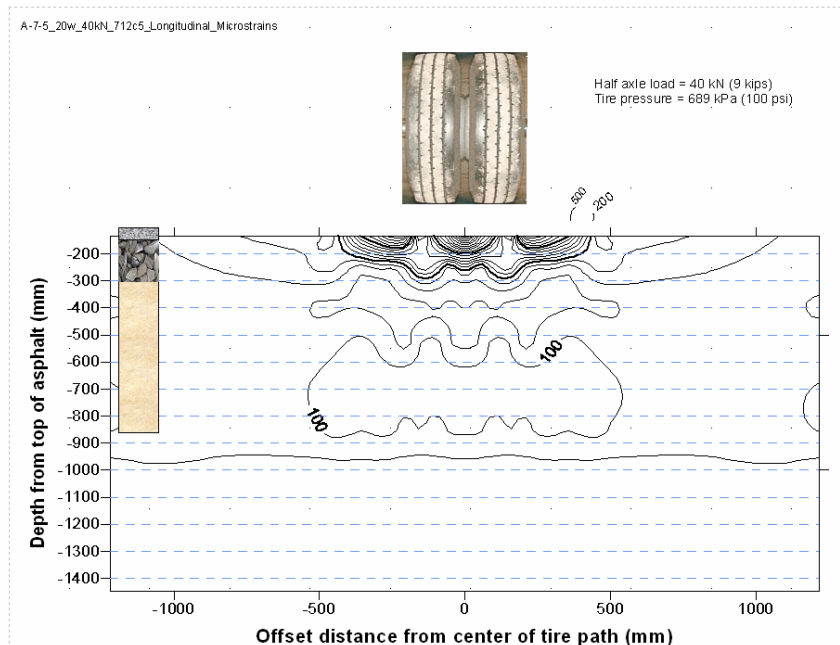
Figure 86. Longitudinal resilient strain contour section with subgrade soil A-7-5 at 20% and HVS load of 40 kN (9 kips).
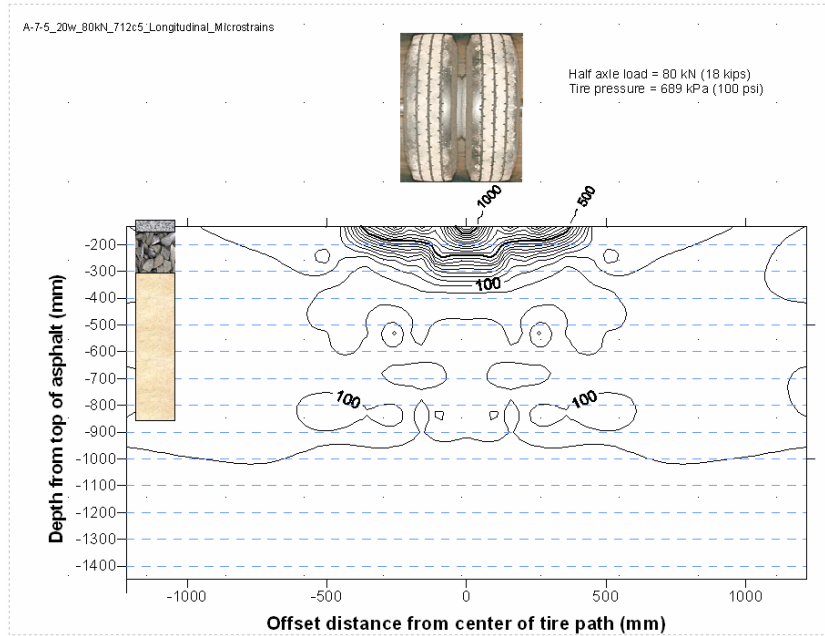
Figure 87. Longitudinal resilient strain contour section with subgrade soil A-7-5 at 20% and HVS load of 80 kN (18 kips).
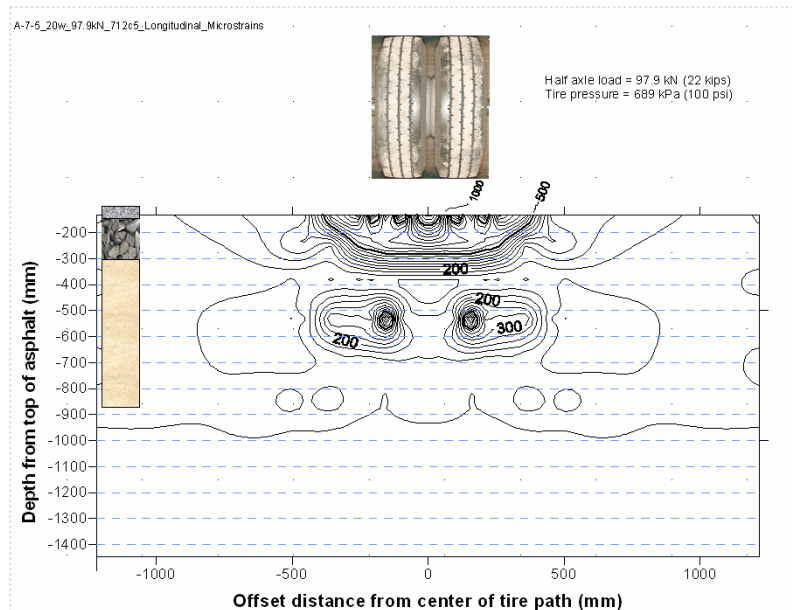
Figure 88. Longitudinal resilient strain contour section with subgrade soil A-7-5 at 20% and HVS load of 97.9 kN (22 kips).
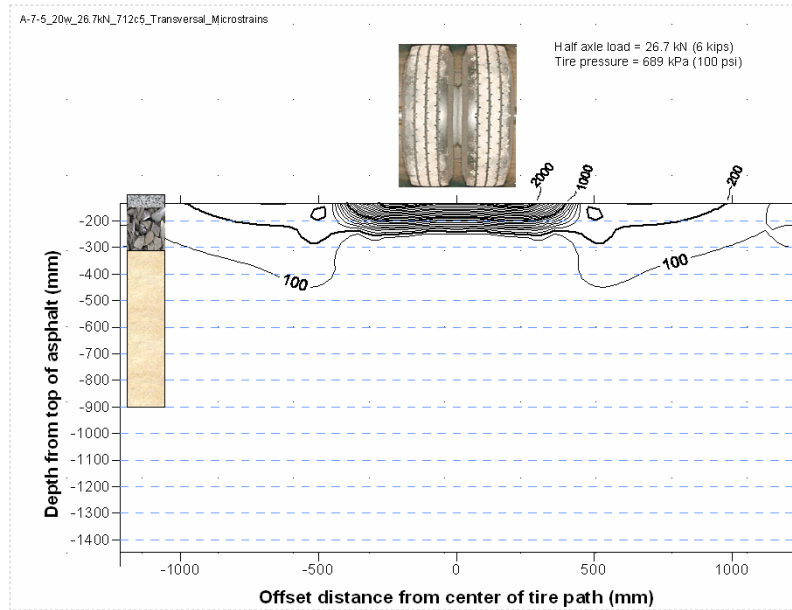
Figure 89. Transversal resilient strain contour section with subgrade soil A-7-5 at 20% and HVS load of 26.7 kN (6 kips).
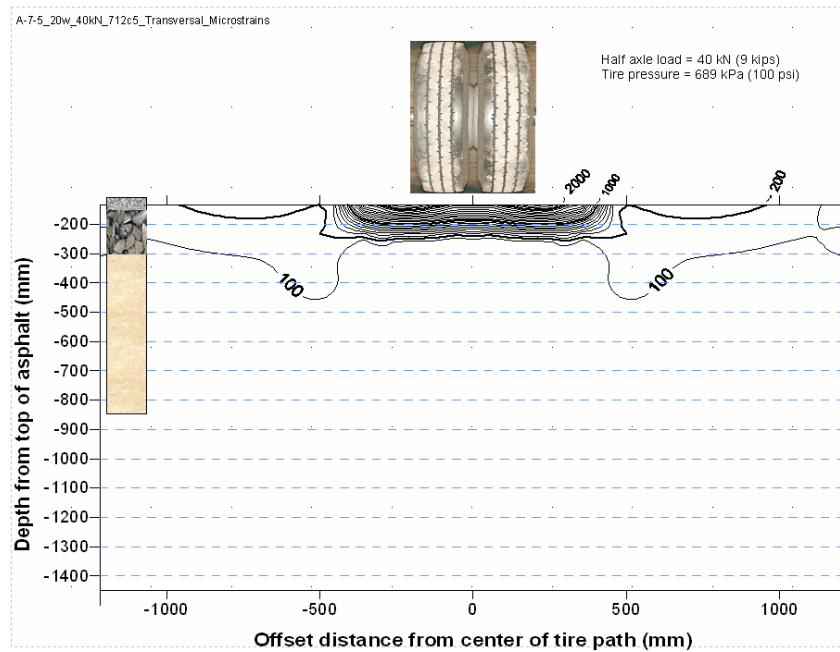
Figure 90. Transversal resilient strain contour section with subgrade soil A-7-5 at 20% and HVS load of 40 kN (9 kips).
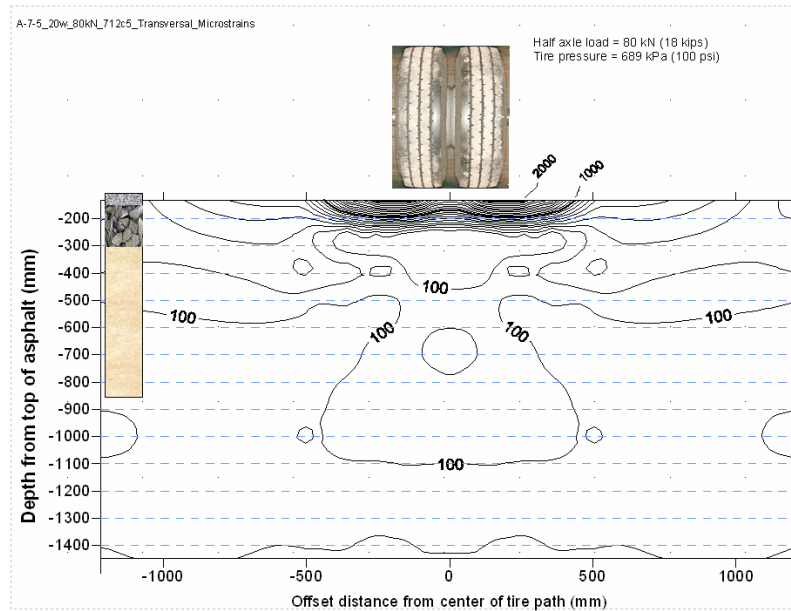
Figure 91. Transversal resilient strain contour section with subgrade soil A-7-5 at 20% and HVS load of 80 kN (18 kips).
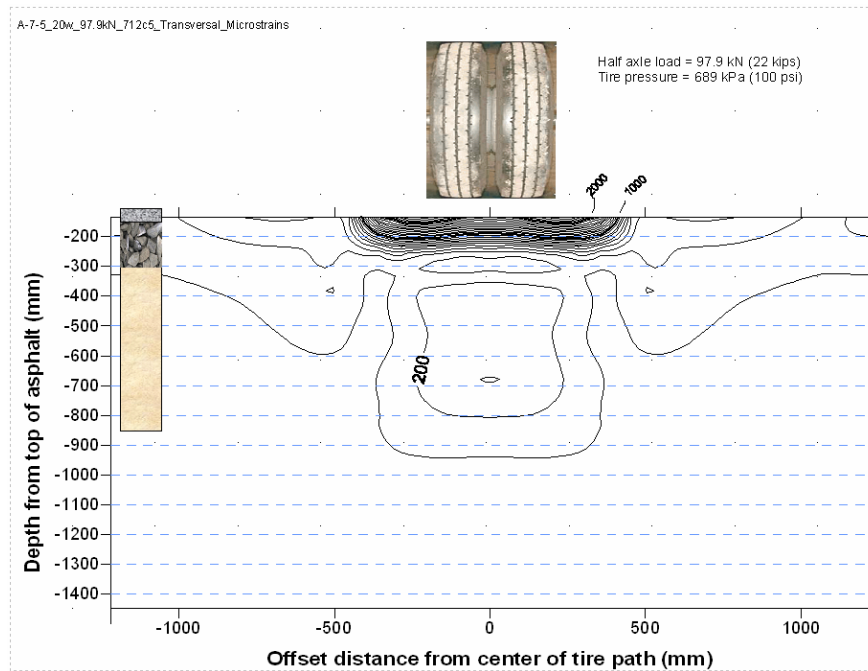
Figure 92. Transversal resilient strain contour section with subgrade soil A-7-5 at 20% and HVS load of 97.9 kN (22 kips).

6.6 Stress Contour Sections

Contour cross sections of the stress measurements were built similarly to the strain contour cross sections. The supporting data is the same as with the stress cross sections. The contour graphs only provide an alternative way to view the same data.

The contour graphs suggest that the vertical, longitudinal and transversal components of stress decreased with depth.

The stress cells closest to the top of the pavement structure were in the base course. There was no stress sensor in the asphalt. Only at the highest load level, the largest vertical stress registered by the stress cells was 450 kPa. Comparing this stress to the tire inflation pressure of 689 kPa (100 psi) assumed to be the applied pressure on top of the asphalt concrete, one can appreciate the reduction in vertical stress that occurred from the top to the bottom of the asphalt layer. This stress reduction is due to the development of shear forces within the asphalt.
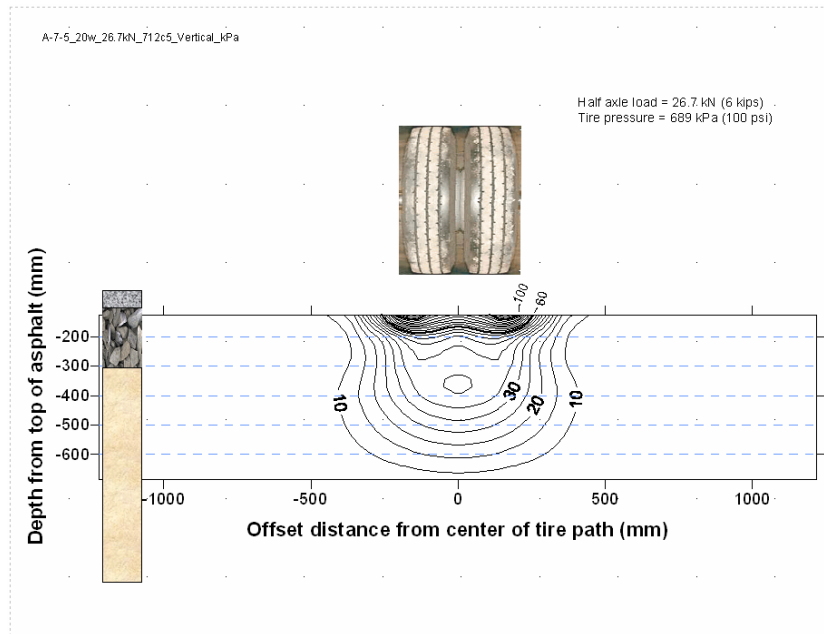
**Figure 93. Vertical stress contours in test section with subgrade A-7-5 at 20% moisture content and HVS load of 26.7 kN (6 kips).**
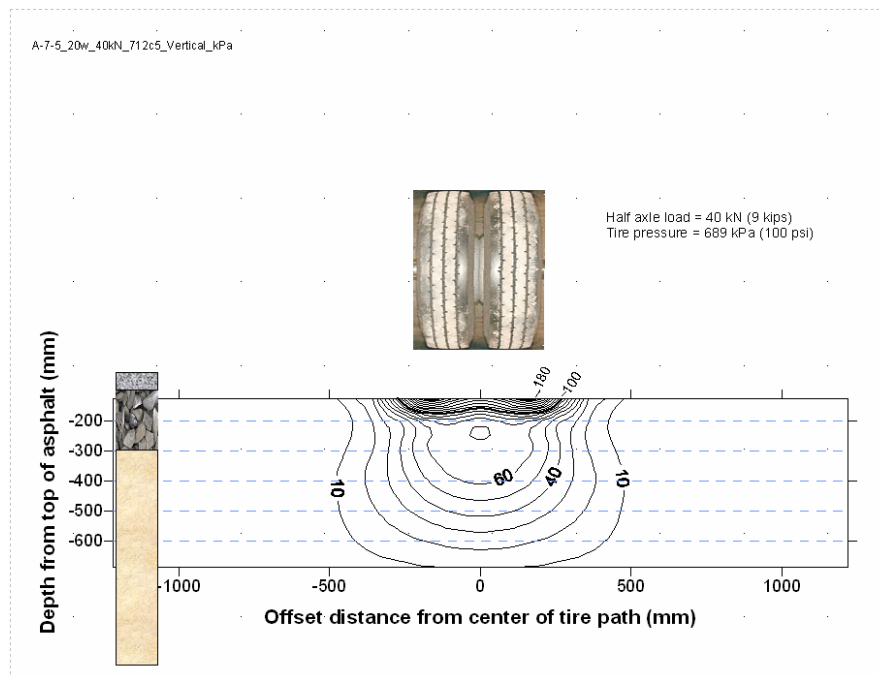

Figure 94. Vertical stress in test section with subgrade A-7-5 at 20% moisture content and HVS load of 40 kN (9kips).
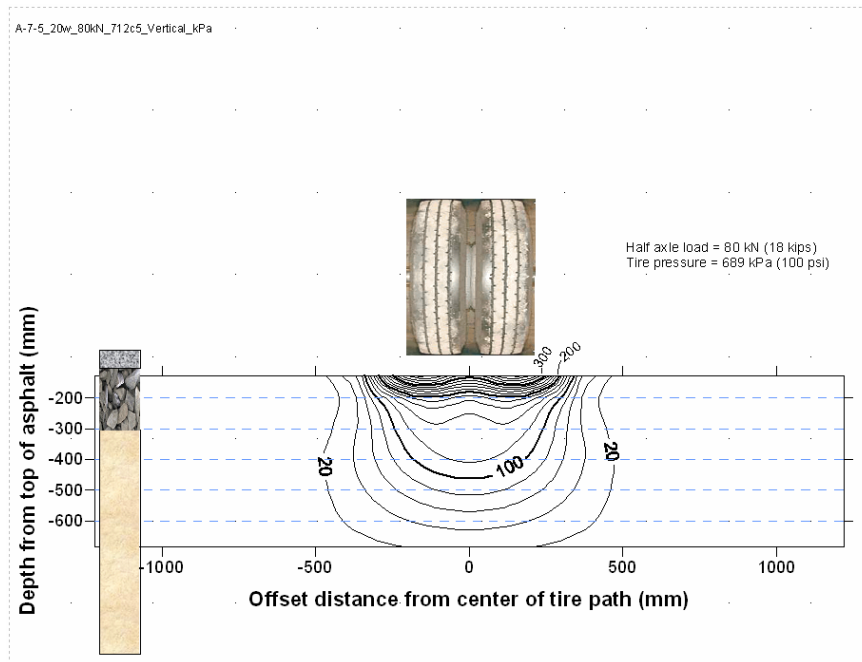
Figure 95. Vertical stress contours in test section with subgrade A-7-5 at 20% moisture content and HVS load of 80 kN (18 kips).
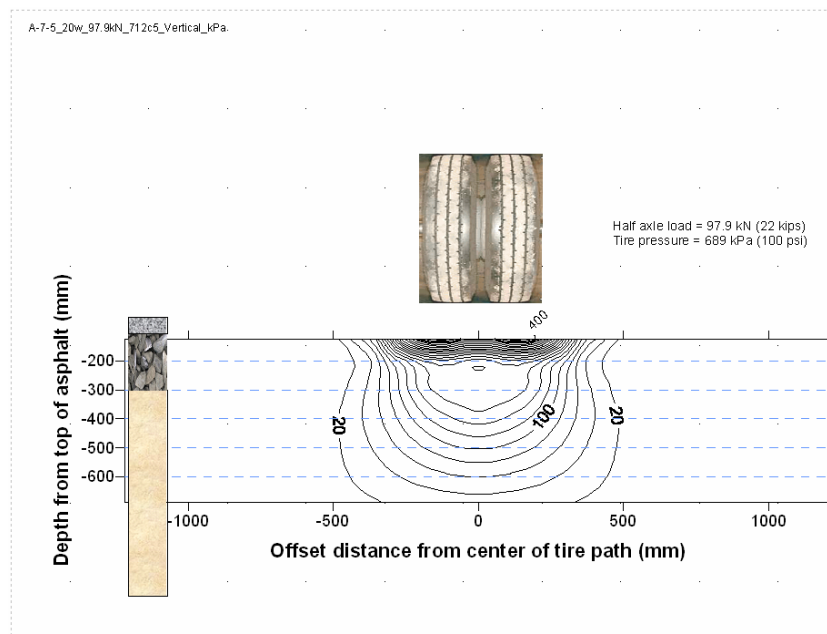
Figure 96. Vertical stress contours in test section with subgrade A-7-5 at 20% moisture content and HVS load of 97.9 kN (22 kips).

A-7-5_20w_26.7kN_712c5_Longitudinal_kPa

Half axle load = 26.7 kN (6 kips)
Tire pressure = 689 kPa (100 psi)
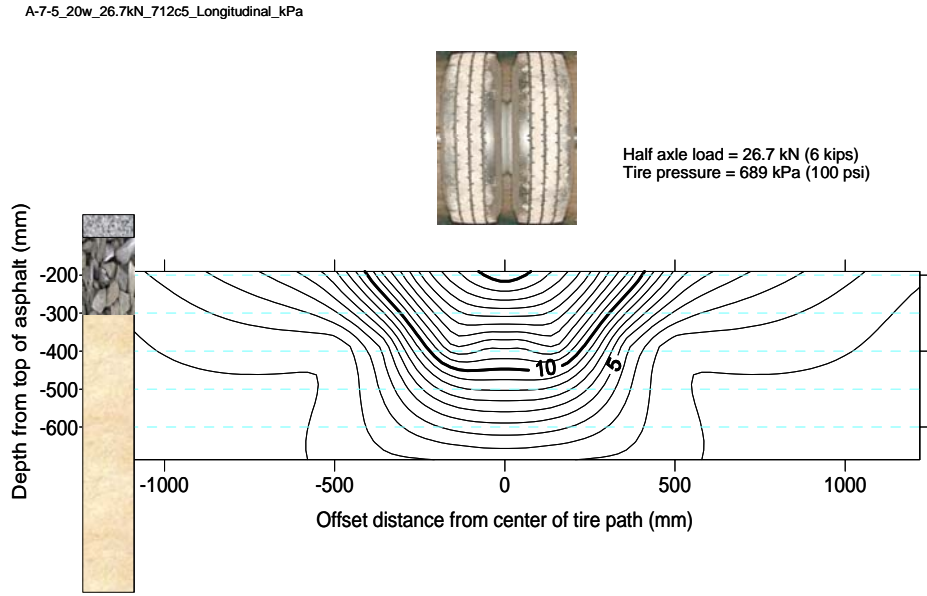
Figure 97. Longitudinal stress contours in test section with subgrade A-7-5 at 20% moisture content and HVS load of 26.7 kN (6 kips).

A-7-5_20w_40kN_712c5_Longitudinal_kPa

Half axle load = 40 kN (9 kips)
Tire pressure = 689 kPa (100 psi)
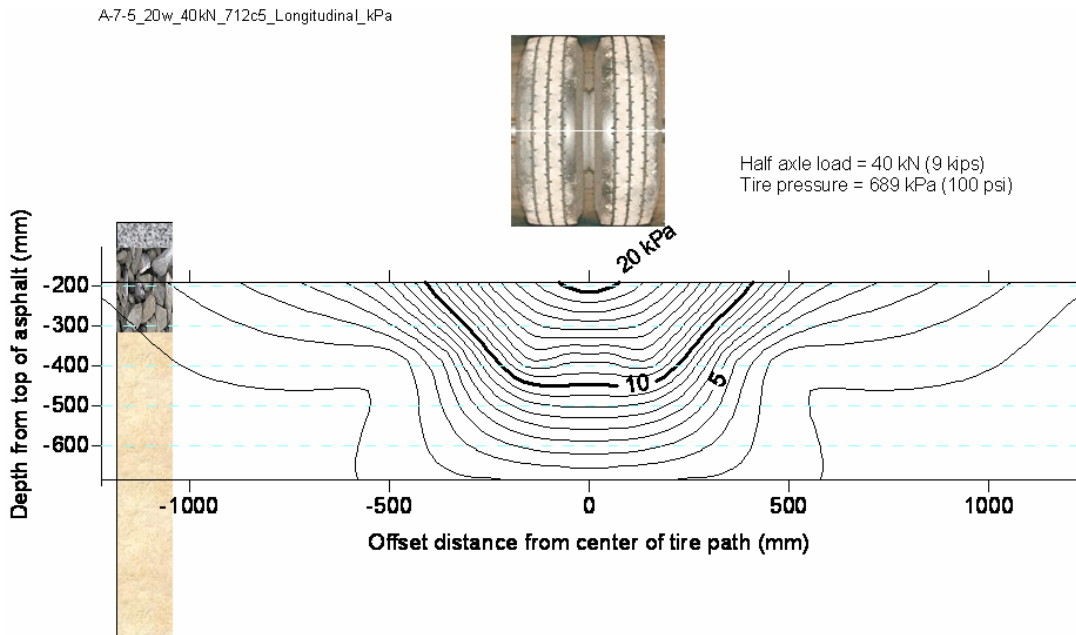
Figure 98. Longitudinal stress contours in test section with subgrade A-7-5 at 20% moisture content and HVS load of 40 kN (9 kips).
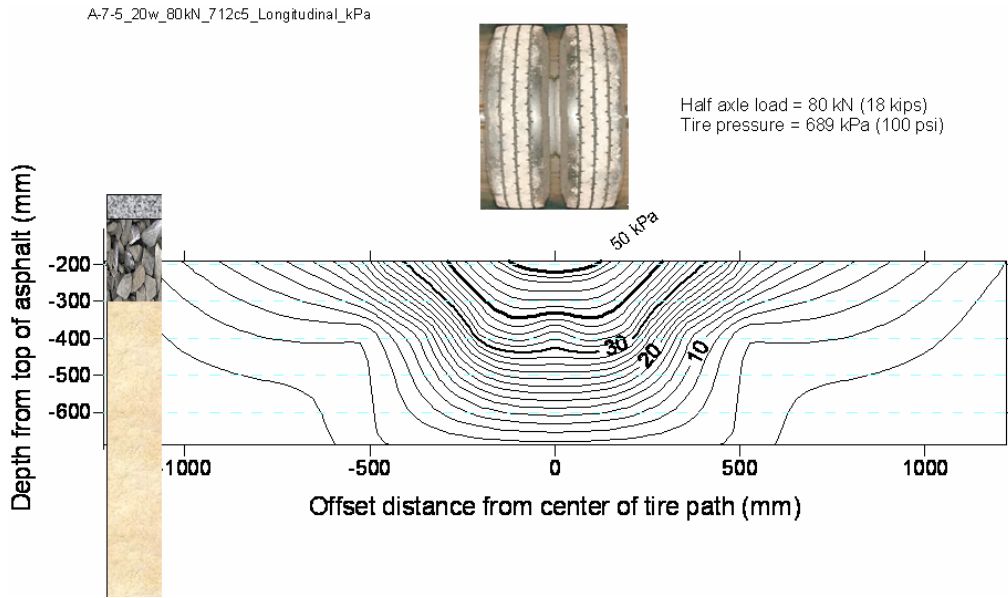
Figure 99. Longitudinal stress contours in test section with subgrade A-7-5 at 20% moisture content and HVS load of 80 kN (18 kips).
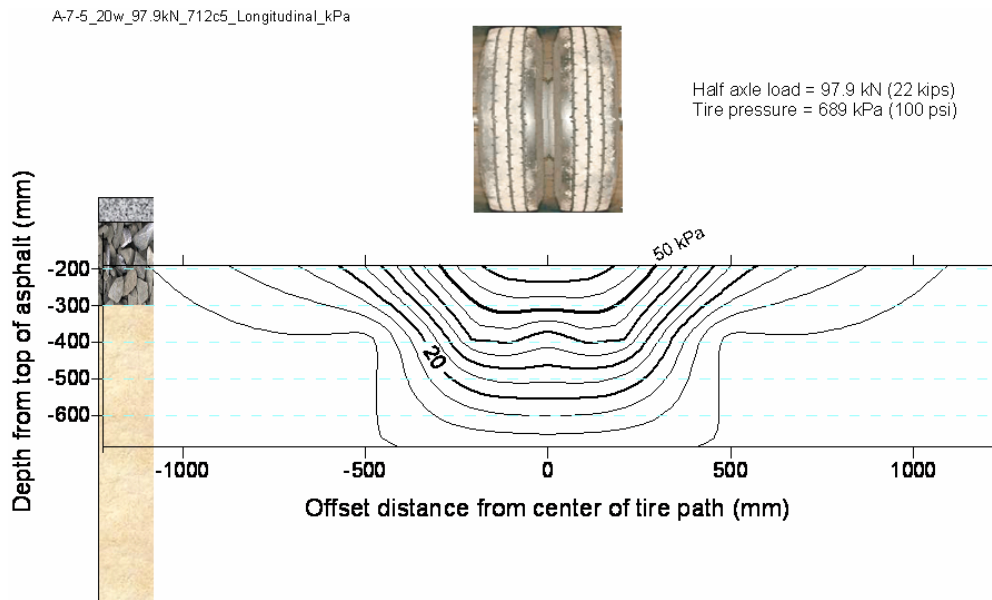
Figure 100. Longitudinal stress contours in test section with subgrade A-7-5 at 20% moisture content and HVS load of 97.9 kN (22 kips).
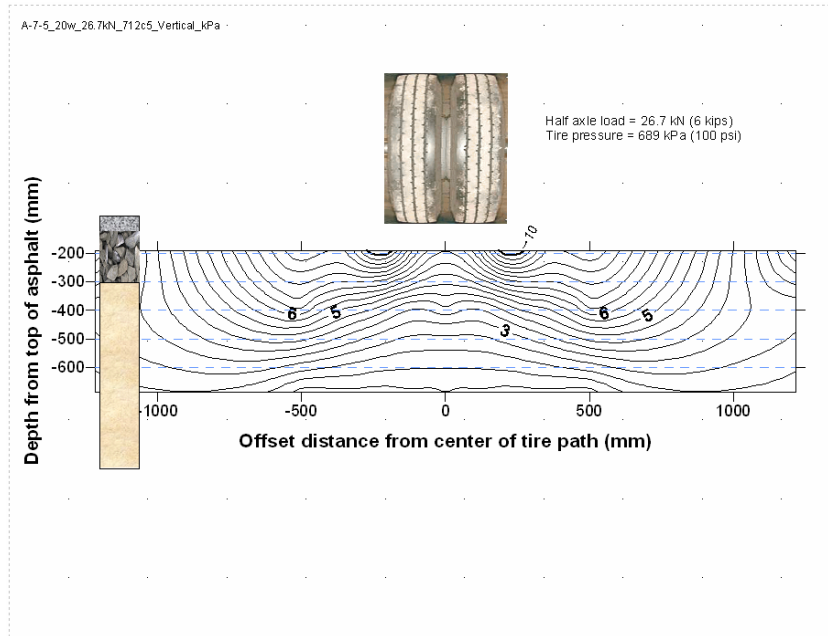
Figure 101. Transversal stress contours in test section with subgrade

A-7-5 at 20% moisture content and HVS load of 26.7 kN (6 kips).
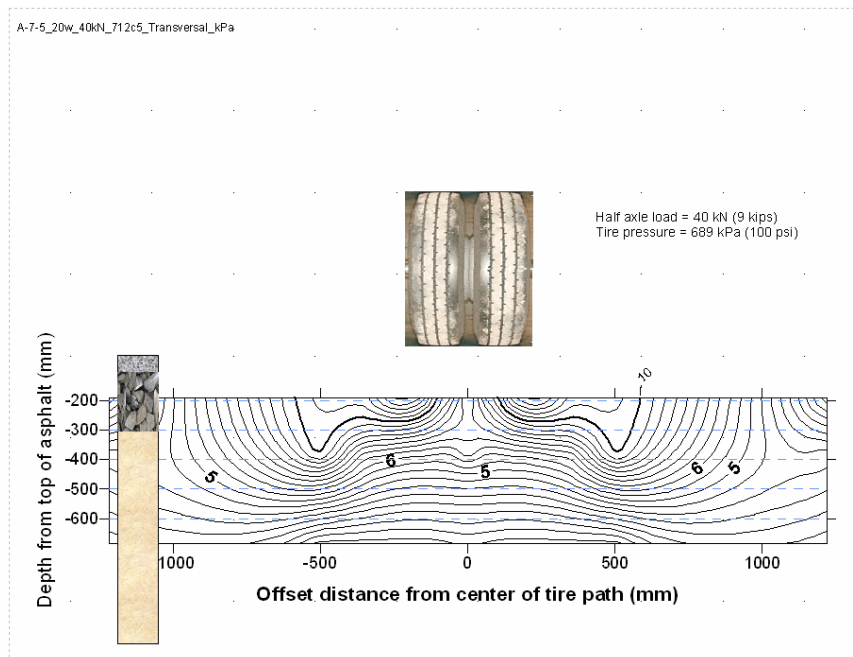
Figure 102. Transversal stress contours in test section with subgrade

A-7-5 at 20% moisture content and HVS load of 40 kN (9 kips).
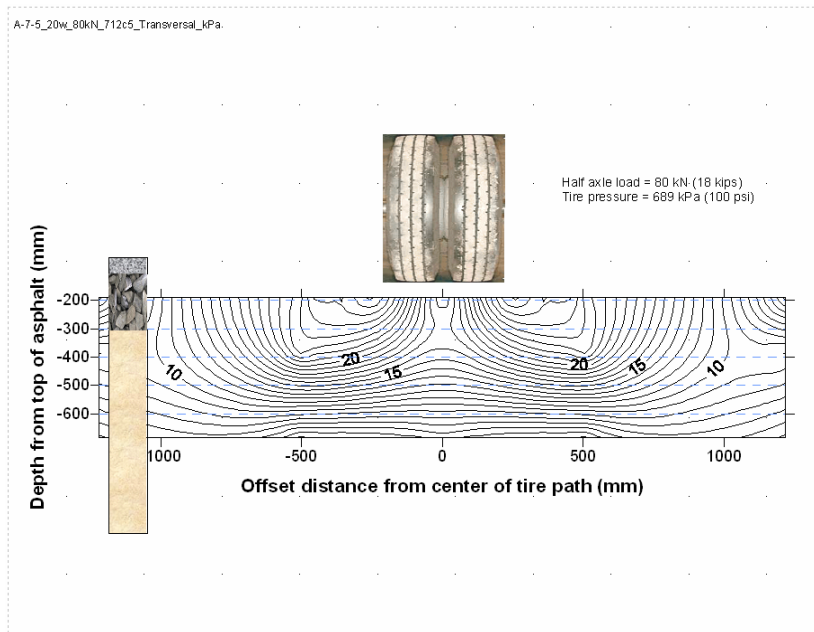
Figure 103. Transversal stress contours in test section with subgrade A-7-5 at 20% moisture content and HVS load of 80 kN (18 kips).
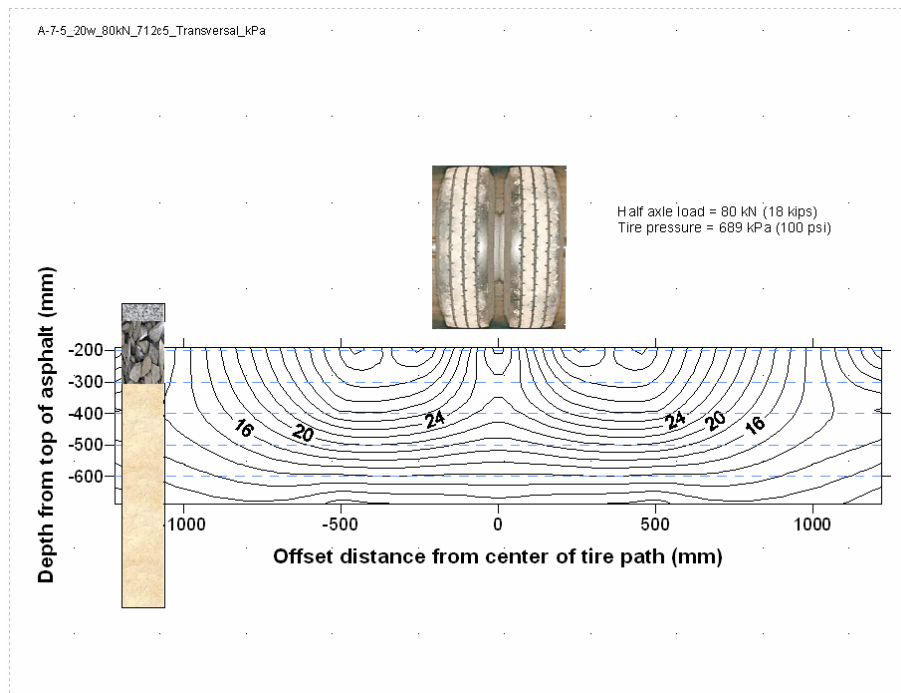
Figure 104. Transversal stress contours in test section with subgrade A-7-5 at 20% moisture content and HVS load of 97.9 kN (22 kips).

6.7 Subgrade Rut Prediction Models

6.7.1 Experimental Results and Prediction Models

The experimental results in terms of total surface rutting and the vertical permanent deformation at the top of the subgrade were used to develop models that predict permanent strain at the top of the subgrade and at 152.4 mm (6 in.) below the top of the subgrade as a function of soil type, moisture condition, number of traffic repetitions and traffic load intensity.

The variability of the experimental results is the product of the variability of a series of test parameters such as soil density, layer thickness, layer moduli, moisture content, temperature, and soil composition. For each test window at a given number of traffic repetitions, the obtained rut depth test results belong to a random distribution of values as illustrated in Figure 105. The true mean of measurement is not known, but it is estimated from the measured values that fall into a random distribution. It appears that in Figure 105 there are two distinct groups of experimental results corresponding to two distinct cases. For each soil type at each moisture condition, the experiments in this study produced rut depths that belong to a random distribution.
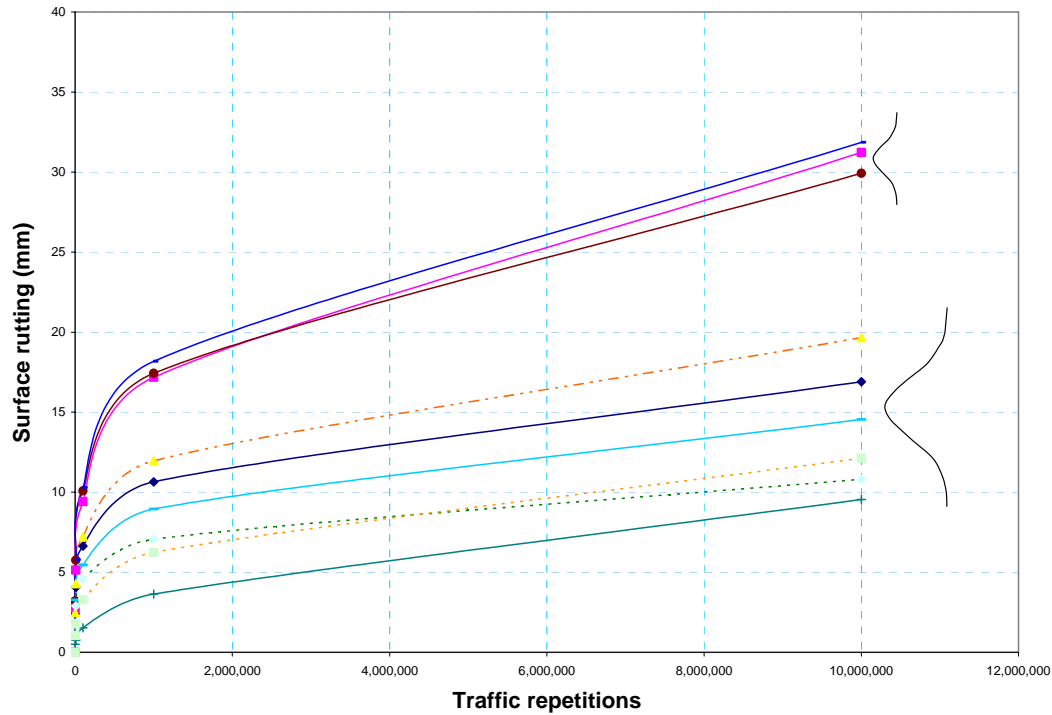
Figure 105. Variability of Test Results.

The new AASHTO mechanistic-empirical design procedure for flexible

pavements incorporates one rut prediction model for the asphalt concrete layer and one

for all unbound materials: base, sub-base and subgrade. The software that implements the

method divides the various pavement layers into sub-layers. The resilient strain is

calculated using the linear elastic analysis software JULEA or a finite element code. The

plastic strain at the mid-depth of each sub-layer is calculated through a relationship

between plastic and resilient strains and the number of traffic repetitions. The current

software calculates the permanent strains at the top of the subgrade and at a depth of 152

mm (6 in.) below the top of the subgrade. Then permanent deformation is calculated by

integrating of permanent strains in the various pavement sub-layers.

During the service life of a pavement, three stages of permanent deformation or strain are recognized: primary, secondary and tertiary. Figure 106 illustrates this concept.
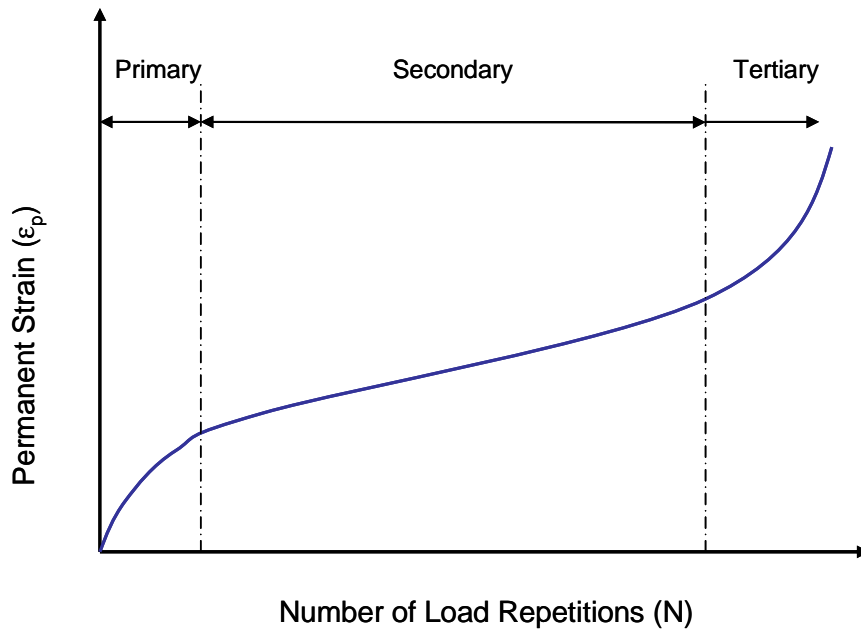
Figure 106. Typical Stages of Permanent Strain Progression in Pavements.
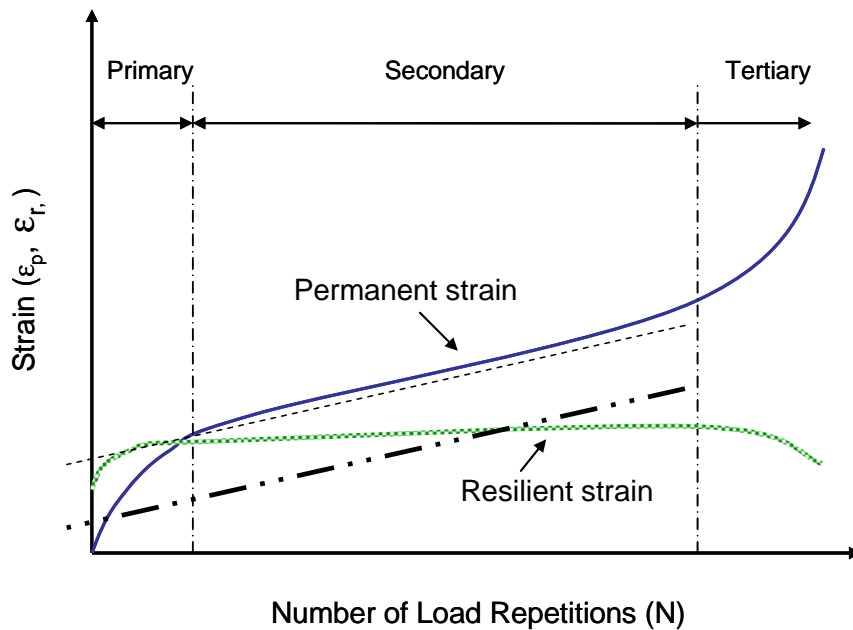
Figure 107. Typical Stages of Permanent Deformation Progression in Pavements.

During the primary stage, strain and deformation progress in non-linear modes as functions of traffic repetitions. This is due to closing of voids left from incomplete compaction and initial particle slips and rotations needed to accommodate the soil particles until point-to-point contacts are established. During the secondary stage, strain and deformation increase according to a near linear relationship with traffic repetitions. At the end of the secondary stage, shear failures occur and deformations and strains progress in accelerated non-linear mode with respect to the number of traffic repetitions. Pavement distress is normally visible at this stage. Normally, pavements are not allowed to reach this stage due to safety concerns.

Resilient strains also typically begin in a non-linear mode, followed by an approximately linear progression during the secondary stage, and non-linear decrease during the tertiary stage.

The approach adopted in the current mechanistic-empirical design methodology assumes that permanent strains are proportional to the resilient strains. This is illustrated in Figure 107 by the two parallel discontinuous lines representing the idealized permanent and resilient strains. Furthermore, the primary stage is substituted with a backward projection of the secondary stage linear function until the intersection with the ordinate axis at zero traffic repetitions. Unfortunately, in most cases, the experimental data indicate significant differences between the slopes of the permanent and the resilient strain curves during the secondary stage. Therefore, the models developed based on the experiments of this study predict the permanent strains within the primary and secondary stages as functions of the number of traffic repetitions, soil type, load intensity and subgrade moisture condition. Unfortunately the experiments in this study were restricted

to only one level of asphalt and base course thickness. For these models to be applicable

to other geometries, some adaptation is needed to consider the effect of asphalt and base

thickness values that differ from those used in these test sections.

6.7.2 Soil Type Specific Permanent Deformation Models

An attempt was made to develop a permanent strain prediction model that could

be applied to all subgrade soil types, perhaps thru correlations of common soil properties.

Unfortunately, no such generic correlation could be developed. Instead, the experimental

data indicated the need to develop prediction models that are specific for each of the four

subgrade soil types included in this study. The models were obtained by regression

analysis relating permanent deformation or strain to the number of traffic repetitions, load

intensity, and moisture condition for each subgrade soil type.

The current mechanistic-empirical design software requires the estimation of

vertical permanent strain at two depths in the subgrade: at the top of the subgrade and at a

depth of 152.4 mm (6 in.) below the top of the subgrade.

For Subgrade Soil Type A-2-4:

The following models are defined for the range of subgrade moisture conditions

from optimum to 6 percent wet of optimum by weight.

$$\varepsilon_{p, z = 0} = (0.3554*N^{0.2884}) * (0.98 + 0.00000004668*L^{3.5}) * (0.37+0.00750973*\Delta w^{1.6148})$$

$$* \ 6562 \hspace{6cm} \text{Equation 6.1}$$

$$\varepsilon_{p,\,z\,=\,6} = (0.3554*N^{0.2884}) * (0.98 + 0.00000004668*L^{3.5}) * (0.37+0.00750973*\Delta w^{1.6148})$$

$$* 4265 \qquad\qquad\qquad\qquad\qquad\qquad\qquad \text{Equation 6.2}$$

where:

$\varepsilon_{p,\,z\,=\,0}$ = Vertical permanent strain on top of the subgrade

$\varepsilon_{p,\,z\,=\,6}$ = Vertical permanent strain at depth of 152.4 mm (6 in) below the top of the

subgrade.

N = Number of traffic repetitions

L = Half axle load intensity in kN   (1 kN = 0.2248 kips)

Δw = Percent gravimetric moisture content differential from optimum

For Subgrade Soil Type A-4:

The following models are defined for the range of subgrade moisture conditions
from optimum to 4 percent wet of optimum by weight.

$$\varepsilon_{p,\,z\,=\,0} = (-1.6+0.835N^{0.2094}) * (0.11 + 0.000055L^{2.374}) * (1+ 1.2\,\Delta w) *$$

$$(0.26+0.028*\Delta w^{1.428}) * 6562 \qquad\qquad\qquad\qquad \text{Equation 6.3}$$

$$\varepsilon_{p, z=6} = (-1.6+0.835N^{0.2094}) * (0.11 + 0.000055L^{2.374}) * (1+ 1.2\ \Delta w) *$$

$$(0.26+0.028*\Delta w^{1.428}) * 4265 \hspace{3cm} \text{Equation 6.4}$$

<u>For Subgrade Soil Type A-6:</u>

The following models are defined for the range of subgrade moisture conditions from optimum to 4 percent wet of optimum by weight.

$$\varepsilon_{p, z=0} = (1.5+0.425N^{0.427}) * (-9.45+6.56L^{0.123}) * (0.304+0.004*\Delta w^{2.162}) * 6562$$

$$\text{Equation 6.5}$$

$$\varepsilon_{p, z=6} = (1.5+0.425N^{0.427}) * (-9.45+6.56L^{0.123}) * (0.304+0.004*\Delta w^{2.162}) * 4265$$

$$\text{Equation 6.6}$$

<u>For Subgrade Soil Type A-7-5:</u>

The following models are defined for the range of subgrade moisture conditions from optimum to 6 percent wet of optimum by weight.

$$\varepsilon_{p, z=0} = =(0.749N^{0.115}) * (0.936 + 0.00000001256L^{4.2165}) * (0.172+0.004*\Delta w^{1.513}) *$$

$$6562 \hspace{5cm} \text{Equation 6.7}$$

$$\varepsilon_{p, z=6} = =(0.749N^{0.115}) * (0.936 + 0.00000001256L^{4.2165}) * (0.172+0.004*\Delta w^{1.513}) *$$

4265   Equation 6.8

CHAPTER 7

SUMMARY, CONCLUSIONS AND RECOMMENDATIONS

7.1 Summary

A national pooled-fund study SPR-2(208) named Pavement Subgrade

Performance Study was established to evaluate the existing subgrade failure criteria for

the design of flexible pavements. While this study was in progress, a new proposed

mechanistic-empirical design methodology was also in progress. The new method is

known as the NCHRP 1-37A Guide or the Mechanistic-Empirical Pavement Design

Guide (MEPDG). As the framework for the MEPDG method became more defined, the

focus of this pooled-fund study adjusted to develop subgrade rut prediction models that

could improve the rut prediction capabilities of the new pavement design method.

The MEPDG uses a permanent deformation prediction model for asphalt concrete

and a separate model for all unbound pavement layers, including a coarse aggregate base,

sub-base, and subgrades that may consist of sand, fine-grained silts, clays and other soil

type mixtures. The unbound materials model in the MEPDG only indirectly considers

material type and moisture content through use of resilient modulus values for a soil. It is

based on the assumption that permanent deformation is proportional to resilient

deformation. According to experimental data presented in this report, this assumption may need revision.

The results of the experiments presented in this report show that the existing failure criteria fits well to one soil type, but not well to the other three soil types included in this study. The data suggests that failure criteria must be specific for each soil type.

Subgrade rut prediction models were developed based on the experimental data from this study. The new proposed models were design in terms of permanent strain at the top of the subgrade and at a depth of 152.4 mm (6 in.) below the top of the subgrade because these are the inputs required by the existing MEPDG software. The proposed models are functions of load intensity, subgrade moisture condition, and number of traffic repetitions.

7.2 Conclusions

Mechanistic analysis of flexible pavement structures is very complex because of interactions among:

- The diverse mechanical behaviors of the constituent materials that include linear and non-linear elastic, plastic, and viscous components

- Seasonal variations of moisture and temperature

- Aging of the materials

This is illustrated in Figure 1.

The relationships between pavement response (stresses and strains) and performance (rutting, cracking, faulting, etc.) are not simple. In flexible pavements, rutting constitutes a major distress mode, which often determines the length of service life for a pavement. Most transportation agencies have set allowable rutting limits to reduce the risk of accidents due either to hydroplaning over water-filled ruts or to sliding on bands of ice or snow in ruts on traffic lanes. Therefore, rut prediction models are at the core of the design of flexible pavement structures.

Measurements of total pavement rut at failure shown in Figure 36 indicate that, within the experimental domain, increases in moisture in the subgrade shortened the service life of the test sections. An exception was the case of subgrade soil type A-2-4 for which moisture above optimum slightly increased the number of traffic passes to failure. This counter-intuitive moisture effect may be due to the development of some cohesion caused by the added moisture, but it may be limited to the range of moisture conditions covered by these experiments. Higher moisture level effects with this soil were not investigated because the soil would drain any additional water to the bottom of the test basin. The only other stable higher moisture level with this soil would be total saturation. Figure 36 also suggests that, for each soil, there exists a critical moisture content beyond which pavement rutting is greatly accelerated. For soil types A-4 and A-6, it appears that this limit is 21 percent (gravimetric). For soil type A-7-5, it appears that the critical moisture content is 27 percent.

The measurements of subsurface permanent deformation, presented in Figures 38 through 41, indicate that the percent contribution by the base course to the total pavement rut depth increases with stronger subgrades and decreases with softer subgrades.

Sensor installation requires extreme care to preserve the density and moisture of the subgrade soil so that the soil surrounding the sensors can correctly represent the soil in the rest of the soil layer. In the design of full-scale pavement experiments, many sensors embedded in the test sections provides finer representation. However, mutual close proximity of sensors may significantly change the soil density and moisture properties of the combined sensor-soil structure, thereby distorting test results intended to measure soil properties and responses alone. Under the assumption that stress and strain would be maximized at points under the center of the tire path, sensors were installed only at these locations.

A method was devised to create a system of "virtual sensors" that generated detailed cross sections of stress and strain without the expense of more real sensors and their potential disturbance of the soil layers. Figure 55 illustrates the real and virtual system of sensors. The concept of virtual sensors obviates the need for real sensors, as follows: The response of the real sensors were recorded at a series of replicate traffic repetitions conducted with the tire assembly moved to corresponding offset positions relative to the real sensors. These tests revealed what would have occurred at locations away from the wheel path. This method proved very effective at producing detailed cross sections of strain and stress that provided insight into the mechanical behavior of pavement structures.

The virtual sensor cross sections on a pavement test section with a strong subgrade indicated that strains were largest in the upper half of the base course followed by the lower half of the base course and, much smaller in the subgrade. As expected, strains continued to decrease with depth. The depths indicated in

the figures are relative to the upper surface of the asphalt concrete. At the standard axle load level, the strain measurements at a depth of 1.0 m (39.4 in.) were so small that they could not be discerned from the normal electronic noise in the sensor output. At the heaviest load level, the strains measurements at a depth of 1.0 m (39.4 in.) could still be reliably measured, but the strain at a depth of 1.5 m (59 in.) was read with difficulty from within the normal electronic noise band. This information can also be used to specify compaction requirements for subgrade fills.

Existing mechanistic-empirical methods NCHRP, 2004) assume that permanent strain is proportional to resilient strain. The experimental data suggest significant departures from this assumption, as illustrated in Figure 105. Therefore, the proposed models are estimating permanent deformation independent from this assumption.

At the standard axle load level, at the center of the top of the subgrade, the magnitudes of the longitudinal and lateral stresses were approximately 47 and 20 percent of the vertical stress. It is important to recognize these proportions of stress in the vertical, longitudinal and transversal directions when interpreting data from triaxial tests where the confining stress is axisymmetric.

7.3 Recommendations

The current MEPDG software (NCHRP, 2004) calculates the permanent strains at the top of the subgrade and at a depth of 152 mm (6 in.) below the top of the subgrade. Then permanent deformation is calculated by integrating of permanent strains in the

various pavement sub-layers. The models proposed in this report were tailored to serve the predictions of permanent strain as required by the existing mechanistic-empirical design software. However, these proposed models are limited to a range of moisture conditions consistent with the range explored in the experimental test sections. For moisture conditions lower than the optimum moisture content, the predicted values should be those obtained at the optimum moisture content. For moisture content values higher than the recommended limit, the pavement designer should be advised to artificially alter the field conditions to avoid stability problems that could destroy the pavement with only few traffic passes, as shown in Figure 32, which corresponds to a subgrade soil type A-4 at 23 percent gravimetric moisture content. The proposed models are also limited in that they were developed with only one asphalt thickness and one base course thickness. Additional test sections including these important parameters are recommended for future research through which more general and reliable models could be developed. Much progress was accomplished in this Pavement Subgrade Performance Study, but more work is needed to arrive at permanent deformation prediction models that are sufficiently reliable and that cover a range of asphalt and base course thicknesses used in practice.

As awareness of the complexities in the mechanical behavior of pavements increases, the development of a mechanistic-empirical methodology for analysis, design, and evaluation of pavement structures should continue apace. The existing draft of the MPEDG method is a strong framework into which improved components can be added as they become available.

The experimental data supports the hypothesis that significant particle rotations and slippages occur in the base course during traffic loads. This was evidenced by significant changes in resilient strain in the base course as traffic repetitions increased. One potential approach to account for such behavior would be the use of discrete element analysis for the base course, coupled with finite element analysis for the asphalt and subgrade layers.

The development of the virtual sensor method described in section 6.2 of this report provided a novel approach to investigate the mechanical behavior of the pavement test section built with subgrade soil type A-7-5. It is recommended that this method be applied to all future test sections.

REFERENCES

AASHTO, *Guide for Design of Pavement Structures*, American Association of State Highway and Transportation Officials, Washington, D.C., 1986.

AASHTO, *Guide for Design of Pavement Structures*, American Association of State Highway and Transportation Officials, Washington, D.C., 1993.

AASHTO, *Standard Specifications for Transportation Materials and Methods of Sampling and Testing*, American Association of State Highway and Transportation Officials, Washington, D.C., 2005.

Ahlvin, R.G. and Ulery, H.H., *Tabulated Values for Determining the Complete Pattern of Stresses, Strains and Deflections beneath a Uniform Circular Load on a Homogeneous Half Space*, Highway Research Board Bulletin 343, Washington, D.C., 1962

Asphalt Institute. *Research and Development of the Asphalt Institute's Thickness Design Manual* (MS-1), 9th Ed., Research Report 82-2, 1982.

Barksdale, R. D. *Laboratory Evaluation of Rutting in Base Course Materials*. Proceedings of the Third International Conference on Structural Design of Asphalt Pavements, London, U.K., 1972.

Belcher, D.J., Gregg, L.E., Jenkins, D.S., and Woods, K.B., 1946, *The Origen Distribution and Airphoto Identification of United States Soil*s, Civil Aeronautic Administration Technical Development Report 52, Washington, D.C.

Chen, D.H., Cortez, E.R., Yang, W.S., Zhou, F., and Petros, K., *Analysis of Overload Damage In Thin Flexible Pavements*, Proceeding 85th Annual Meeting of the Transportation Research Board, Washington, D.C., 2006.

Dawson, A., *The ɛmu System Users Manual.* 2nd Edition, University of Nottingham, U.K., 1994.

Dormon, G. M., and C. T. Metcalf *Design Curves for Flexible Pavements Based on Layered System Theory*. Highway Research Record, No. 71, 1965.

El-Basyouny, M., Witczak, M. and Kaloush, K. *Development of the Permanent Deformation Models doe the 2002 Design Guide*, Proceeding 84th Transportation Research Board Annual Meeting, National Research Council, Washington, DC, January 2005.

Fernandes, J.L., Carvalho, J., and Alves, P.A., Effects of Traffic Loading on Portugues and Brazilian Pavements Performance, Proceeding 85th Annual Meeting of the Transportation Research Board, Washington, D.C. , 2006.

Highway Research Board, *The AASHO Road Test, Report 7 Summary Report*, National Research Council, Publication 1061, Washington, D.C., 1962a.

Highway Research Board, *The AASHO Road Test, The ASHO Road Test – History and Description of Project*, Special Report 61G, National Research Council, Publication 816, Washington, D.C. , 1962b.

Hogentogler, C.A., and Terzaghi, K., *Interrelationship of Load, Road and Subgrade*, Public Roads, May Issue, pp.37-64, 1929.

Hoover, J.M.   *Granular Base for Flexible Pavements*. Final Report. Engineering Research Institute, Iowa State University, Ames, Iowa, 1970.

Huang, Y.H., *Pavement Analysis and Design*, 2nd edition, Pearson Prentice Hall, Upper Saddle River, New Jersey, 2004.

Hugo, F. and Epps M., *NCHRP Synthesis of Highway Practice 325*, 2004.

Hugo, F., *Accelerated Pavement Testing Overview,* Proceedings of the 2nd International Conference on Accelerated Pavement Testing, Minneapolis, MN, 2004.

Janoo, V., Irwin, L., and Haehnel, R., *Pavement Subgrade Performance Study Project Overview*, US Army Corps of Engineers. Engineer Research and Development Center. ERDC/ITL TR-03-5, 2003.

Lane, R. and Fish, M., *New Hampshire's Concrete Aggregates and Alkali-Silica Reactivity*, Proceeding 82th Transportation Research Board Annual Meeting, National Research Council, Washington, D.C., 2003.

Lourens, J.P., *Towards Improved Understanding of Surfacing, Base, and Tyre Interaction for Low-Cost Pavement Design*, South African Department of Transport, Report RR 93/559, Pretoria, South Africa, 1995.

NCHRP, *Guide for Mechanistic-Empirical Design of New and Rehabilitated Pavement Structures*, National Cooperative Highway Research Program, NCHRP Project 1-37A Report, National Research Council. Washington, D.C., 2004.

Perkins, S. and Cortez, E.R., *Evaluation of Base-Reinforced Pavements Using a Heavy Vehicle Simulator*, Proceeding 83rd Transportation Research Board Annual Meeting, National Research Council, Washington, D.C., 2004.

Odermatt, N., Janoo, V., and Magnusson, R. , *Analysis of Permanent Deformation in Subgrade Material Using a Heavy Vehicle Simulator*, Proceedings of the First International Conference on Accelerated Pavement Testing, Reno, NV, 1999.

Saarelainen, S., Onninen, H., Kangas, H., and Pihlajamäki, J., *Full-Scale Accelerated Testing of a Pavement on Thawing, Frost-Susceptible Subgrade*, Proceedings of the First International Conference on Accelerated Pavement Testing, Reno, NV, 1999.

Yang, Jun, Wang, W., Petros, K., Sun L., Sherwood J. and Kenis, W. *Test of NCHRP 1-37A Design Guide Software for New Flexible Pavements*, Proceeding 84th Transportation Research Board Annual Meeting, National Research Council, Washington, DC, 2005.

Zhang, J., Ebersohn, and Selig E.T., *Evaluation of Earth Pressure Cells for Pavement Subgrade Performance Study*, Geotechnical Report No. CRR95-427F, University of Massachusetts, Amherst, MA, 1995.